Modeling and Analysis for Control of Reactant and Water Distributions in Fuel Cells

by

Buz A. McCain

A dissertation submitted in partial fulfillment
of the requirements for the degree of
Doctor of Philosophy
(Mechanical Engineering)
in The University of Michigan
2008

Doctoral Committee:
        Professor Anna G. Stefanopoulou, Chair
        Professor N. Harris McClamroch
        Professor Jeffrey L. Stein
        Research Scientist Hosam K. Fathy
        Kenneth R. Butts, Toyota Engineering and Manufacturing, North America

I dedicate this work to my father, Everd A. McCain, the greatest influence on the person I have become. And to my mother, Iona I. McCain, who has always been my greatest supporter.

Acknowledgments

I owe a huge debt of gratitude to my advisor, Professor Anna G. Stefanopoulou, for her guidance and patience during the last three years. I do not know how she managed to put up with me, but I know better than to ask.

Dr. Kenneth R. Butts saved me from a financial abyss with his support of my research at Toyota, and from spiritual oblivion with his friendship and living by example. There's really no way to pay him back, and he's the first person to get me to understand that it is not necessary to repay those kinds of debts.

Dr. Hosam K. Fathy was more than a committee member, his explanations of the academic world helped me make sense of an unfamiliar arena, and his explanations of modeling and model order reduction were indispensable.

I have Professor Jeffrey L. Stein to thank for getting me interested in modeling, starting me down the path to my current specialty. If I ever have a teaching opportunity, my goal will be to imitate his lecture style.

Professor Harris McClamroch is the epitome of the ideal academic. Well-respected and well-informed, high-energy and non-judgmental, helpful and friendly; meeting him through class was providence. I am thankful for his participation in my academic career.

A number of Toyota coworkers and supervisors share the credit for my meager accomplishments, including my last pre-PhD supervisor, Mr. Hiroyuki Koba, who supported my unorthodox plan respectfully. Mr. Chikuo Kubota and Mr. Akio Nishimura taught me that I respond best to trust and responsibility, and without their support, I would not have been able to study at the University of Michigan. Special thanks are owed to Ms. Melissa Spaid, Mr. John Baylis and Mr. James Griffith of Toyota Administration for their open-minded outlook on my return to school.

My labmates made the difference during my time at the Powertrain Control Lab. I am grateful to Dr. Ardalan Vahidi for his warm welcome during my first months, and to Dr. Ray Chiang for his sense of humor and kindness. Dr. Amey Karnik was invaluable to me for his knowledge of fuel cells, linear algebra, and strong logical ability. Dr. Denise McKay, thank you for sharing your towering knowledge of fuel cell operation and experimentation. Finally, I am thankful to Jason Siegel for his willingness to share his knowledge and understanding of the theoretical side of mathematics, as well as a helping hand for just about anything else.

I am very appreciative of the effort made by my study partner Gayathri Seenumani to stay friends with me, since that is not an easy task. Together we conquered

iii

Table of Contents

List of Figures

List of Tables

List of Appendices

Appendix

Chapter 1

Introduction

1.1 Motivation

Fuel cell technology has been 'on the horizon' since its successful implementation in the space programs of the 1950s, with business and technology pundits as far back as 1960 proclaiming that "...a score of non-utility companies are well advanced toward developing a powerful chemical fuel cell, which could sit in some hidden closet of every home silently ticking off electric power" ([1]). Over 47 years since that hopeful prediction, and over 160 years since the fuel cell was discovered, there are still a number of significant obstacles to widescale implementation. Commonly listed barriers include hydrogen generation and storage, component durability, cost, thermal and water management, system integration, poisoning, startup/shutdown, and public perception.

In spite of the great deal of work that remains to be done, fuel cells represent an important part of the proposed hydrogen economy, and an immense opportunity to impact the socioeconomic structure of society. The last several years have seen a significant increase in budgeting for fuel cell research and hydrogen economy development, with examples including General Motors' funding of over \$1B in fuel cell research through 2003 ([2]), President Bush's pledge of \$1.7B over 5 years in research support during the 2003 State of the Union address, and California Gov. Schwarzenegger's promise to install a hydrogen highway refueling system, estimated at \$60 million, by 2010.

1.1.1 Fuel Cell Operation

Polymer electrolyte membrane fuel cells (PEMFC) are electrochemical energy conversion devices that convert the chemical energy of supplied reactants (hydrogen and oxygen) into electricity. Of the many types of fuel cells, the PEMFC is considered a commercially implementable frontrunner for its low temperature operation and efficiency.

Shown pictorially in Fig.1.1, each fuel cell consists of an anode side and a cathode side, commonly referred to as the electrodes. The main components on each electrode are the channel through which the reactants enter/exit the fuel cell assembly and a gas diffusion layer (GDL) that receives all or a portion of the flow and physically distributes the reactants over the catalytic material. The catalyst is typically a coating on the part of the GDL that is in contact with the proton exchange membrane (PEM). The heart of the fuel cell is the PEM, which is a thin proton- and water-permeable material that requires sufficient humidification in order to function efficiently and safely (without damage).
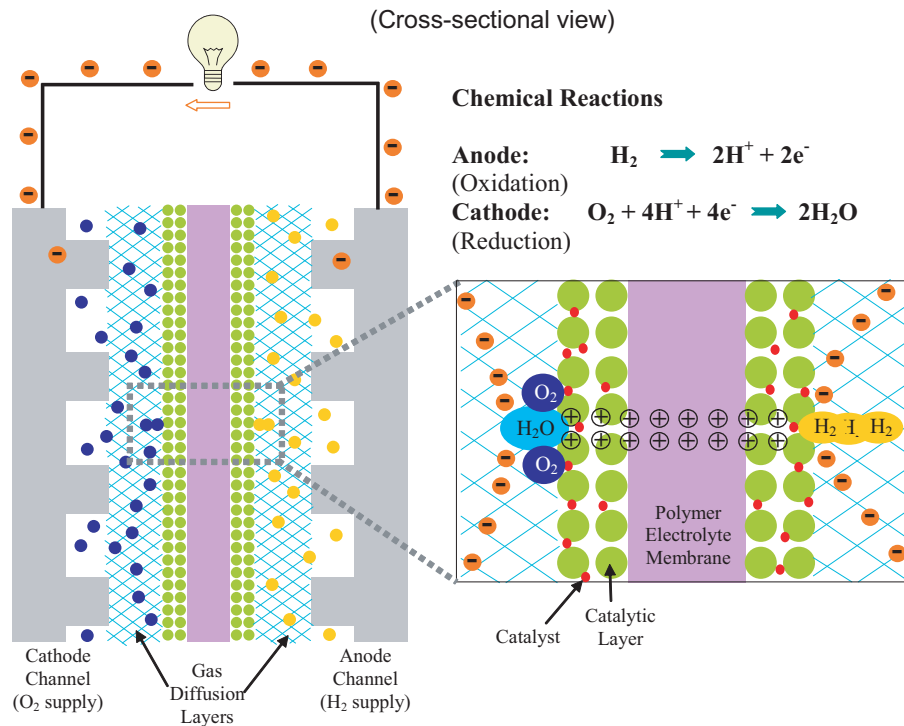
Figure 1.1: Basic concept of fuel cell electricity generation.

To summarize the operation simply, reactant gases are supplied to both electrodes of the fuel cell via the channels, the gas diffusion layer facilitates even distribution to the catalyst-coated membrane, and the catalyst accelerates the oxidation and reduction of the reactants, which are the primary reactions desired for fuel cell operation (Fig. 1.1).

The inputs to the system are the reactants and water (in the form of humidified reactant flows), while the outputs are electricity and more water. Water is mentioned as an input and an output because water is required for operation of the cell, and water is generated as a result of operation of the cell. Oxygen is available as a component of air, and the hydrogen must be processed and provided in pure form to the cell stack. The topic of hydrogen reformation is a complex research topic on its own.

The H_2 oxidation on the anode catalyst of the membrane releases two electrons, which traverse the circuit to satisfy the load required of the cell, while the remaining protons (H^+) travel through the membrane to the cathode side. The cathode side catalyst splits the oxygen molecules, which then join with the electrons completing the circuit and the protons from the membrane to form product water. On both sides of the membrane, the hydrophobic GDL porous material draws the water away from the membrane and catalyst to the respective channels for removal. The production, phase transformation, and transport of water within the fuel cell is critical for efficient performance and long life. As a prime example, the efficiency of membrane proton transport (the proton conductivity) is directly dependent upon the water content of the membrane.

1.1.2 About Water in the Fuel Cell

Water management is the fuel cell implementation barrier addressed in this thesis. At issue is the need to balance the detrimental effect of liquid water accumulation against the requirement of a sufficient level of water in the membrane. High membrane humidity is desirable for proton conductivity, yet excess liquid water has been experimentally shown to be a cause of output voltage degradation [3, 4]. Specifically, liquid water occupies pore space in the porous material of the GDL, impedes the diffusion of reactant flow towards the membrane, and ultimately reduces the active fuel cell area. The pore blocking phenomenon is shown clearly in the environmental scanning electron micrograph (ESEM) image of liquid accumulation in Fig. 1.2.

Transport, generation, and phase change of water are critical aspects of the
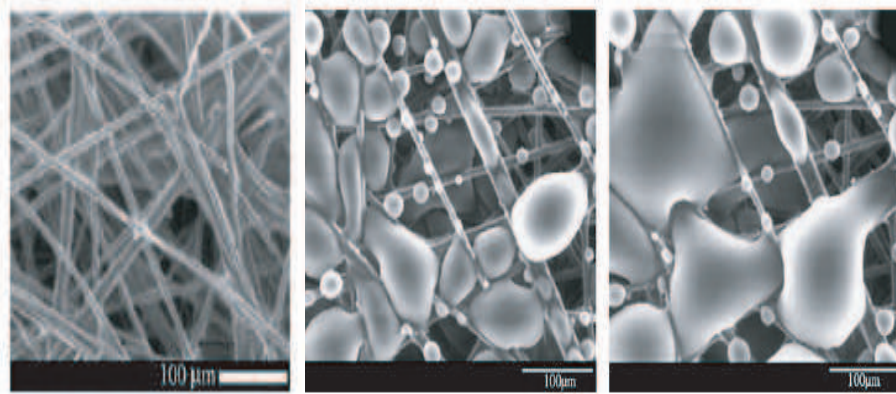
Figure 1.2: ESEM images of GDL porous media in various stages of flooding [5].

modeling of fuel cell dynamics. As shown in Fig. 1.3, evaporation/condensation occurs throughout the GDL and channels, water is generated on the cathode catalyst, and transport across the boundaries between both GDLs and the membrane as well as across the GDL-channel interfaces must be considered. Membrane water transport occurs as a result of competing phenomena, the osmotic drag and back diffusion. Osmotic drag is the process by which protons traveling across the membrane drag water molecules with them. Osmotic drag is a function of water content and current drawn, and flows from anode to cathode. The direction of back diffusion is typically opposite to that of osmotic drag because it is driven by a concentration gradient and the cathode commonly has higher water vapor concentration than the anode.

Also shown in Fig. 1.3 is the valve controlling the anode outlet flow. In dead-ended anode architecture, the valve is closed, and is opened for only a short period of time (e.g. 1 sec in 180 sec) to remove water. In a flow-through arrangement, the control valve position $\bar{u}$ is varied between zero and one based on some control logic.

To avoid damage associated with membrane and GDL drying, fuel cells may be operated under flooding conditions (i.e., a net build-up of liquid water). Removal of liquid water is necessary to regain performance lost when reaction sites become flooded. Recovery is typically accomplished by a massive and brief inlet flow increase (e.g. anode purge), which lowers efficiency due to the large reactant flow out. Additionally, durability can be compromised by the cycling of the GDL through saturated and sub-saturated conditions that arise from these substantial periodic inlet flow rate changes.

The management of water within the fuel cell stack is critical for optimal stack
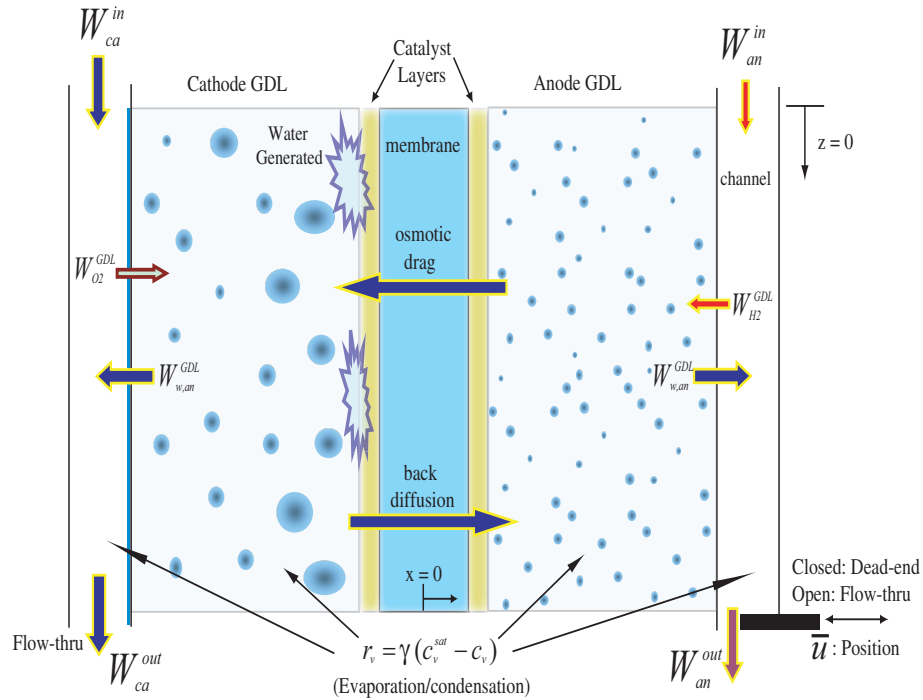
Figure 1.3: Water generation, transport, and phase change occur throughout the fuel cell. A dead-ended anode channel has the outlet closed except during intermittent high velocity flow purges.

performance. The overall goal is to use control to strike a balance between hydrogen and oxygen delivery, and water supply/removal.

In this work, anode water management is addressed (instead of cathode) for four reasons. First, anode components significantly increase the cost, weight, and size of a fuel cell system. Efficient anode water management will enable the elimination or reduction in equipment for anode inlet humidification and/or recirculation systems. Second, avoidance of excessive flooding allows higher hydrogen concentrations to be attained, preventing starvation and fuel cell damage due to carbon corrosion. Third, we desire to implement a flow-through anode channel arrangement to avoid the detrimental effect on GDL material cycling through liquid saturation and drying that occurs during purge cycles in a dead-ended system. Finally, we seek to avoid the previously mentioned cell voltage degradation associated with anode channel flooding.

1.1.3 Objective of the Research

Figure 1.4 provides an overview of the research content of this thesis. The specific objective of this work is to derive a control-oriented fuel cell model where the states used have physical meaning, the computational cost is minimized, and the performance is equivalent to an existing 24-state numeric fuel cell dynamics model [3]. The objective is approached as a combination of model reduction and model derivation. The pre-existing work includes a physics-based continuous model with six 2nd-order PDEs, ordinary differential equations for channel mass balance, and a set of algebraic equations related mostly to membrane transport and orifice flows. The pre-existing work also includes an implementation of the continuous model as a series of cascaded first-order difference equations, with validation. In this thesis, a control-oriented model that maintains the physically-intuitive characteristics is reached via a combination of nonlinear model order reduction, modal analysis, analytic solutions to the PDEs, and a control study of both the continuous PDE model and the difference equation approximation.
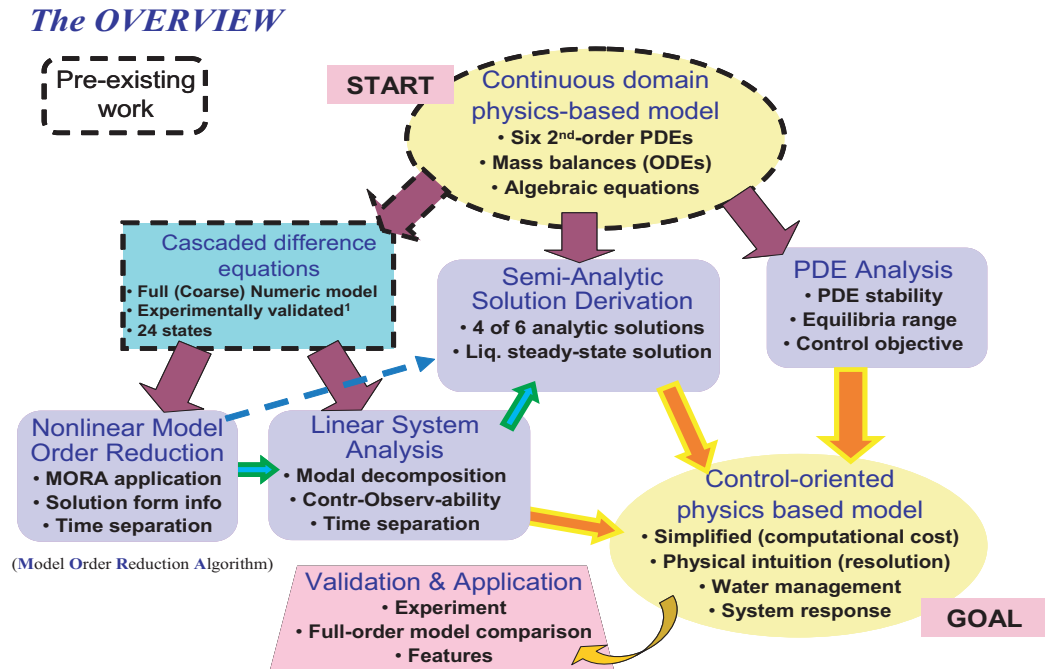
Figure 1.4: Overview of research content, leading to the control-oriented model and its control analysis.

The full-order model was shown to predict the experimentally-observed voltage degradation during prolonged operation in a dead-ended anode condition [3], and the mass of water that accumulates in the anode channels measured via neutron

imaging [4].

Though 24 states might seem sufficiently low order, a 3-section discretization is quite coarse, providing limited or vague physical insights. For analysis, finer spatial resolution is desired, but for each section added to the spatial discretization, a six-fold increase in the number of states is generated. Model order reduction is pursued for the dual purposes of simplification for control and for increased resolution at similar computational cost. The model order reduction methodology created here is a combination of an energy-based state contribution analysis, model assumption error study, empirical model reformulation, singular perturbation investigation, and application of PDE analytic solutions to reduce the computational load associated with simulation of dynamic state equations.

Model simplification is accomplished by derivation of a semi-analytic solution (SAS) model which replaces the majority of the dynamic states with their analytic solutions, thereby reducing computational effort. The SAS model is validated using experimental data under dead-ended operation conditions, and is applicable to flow-through since the on-off dead-ended arrangement is a subset of flow-through.

System behavior is studied through an analysis of the range of possible equilibria. Further, though the total system shows unbounded growth for bounded inputs, the GDL portion of the liquid water distribution is found to be stable using a Lyapunov stability analysis, implying that it is the anode channel liquid mode causing the unbounded growth. Further, this mode is shown to be controllable, a necessary condition for system stabilizability. Based on stability, maximization of hydrogen utilization, equilibrium analysis, and controllability-observability arguments, a hypothesis on an appropriate control setpoint is made. It will be the equilibrium condition such that net water flow into the anode GDL is zero and where the water mass transport across the GDL-channel interface is only in vapor phase. For conditions where a lack of liquid water disrupts evaporation, switching water vapor solutions are provided. This is necessary since the setpoint will be on the cusp of GDL drying. This condition is termed a *borderline* drying condition because it is the point where the boundary between the single-phase and two-phase water distribution lies on the GDL-channel interface *and* there is no liquid flow from GDL to channel.

1.2 Literature Survey

1.2.1 Fuel Cell Modeling

Fuel cell modeling is a widely researched field, as evidenced by the plurality of published work on review of the models themselves (e.g. [6]). For the purpose of providing perspective for the work herein, it is helpful to classify FC models by motivation (as accurate as possible by some experimental measure or control-oriented derivation with sufficient accuracy), by formulation (analytic, low-order numeric, high-order numeric), by dimension (0D, 1D, 1+1D, 2D, 3D), and by dynamic conditions (transient or steady-state).

The zero-dimensional models consider only the average values of the species pressures within the fuel cell, whereas the one-dimensional model adds spatial variation either in the through-membrane direction or along-the-channel. The union of the two types of 1D model produces the 1+1D model, so named because though the channel may be serpentine, it is assumed to be stretched out into a straight line. There is variety in the definition of a 2D model, with some mapping the variation in the plane of the membrane ([7]), some addressing the plane normal to the membrane ([8]), and still others adding a dimension along the channel *width* to the through-membrane spatial variation ([9]).

The 0D models are for control applications, usually with the fuel cell as a component in an overall system (FC plus parasitic support devices or fuel reformation [10],[11],[12]). For the most part, fuel cell modeling has become more complex since Springer et al ([13]) and Bernardi et al ([14]) published early 1D work on the topic in 1991. 1+1D work was pioneered by Fuller et al ([15]) in 1993, followed by Dannenberg's ([16]) steady-state mathematical model revealing variation in membrane water content along the channel. Recent along-the-channel work includes Kulikovsky's ([17]) investigation of semi-analytic means to determine variation in reactant concentration and current density along a straightened channel and Berg et al ([18]) applying channel spatial variation for water management. All the aforementioned 1+1D models are steady-state. Most models published implement numeric solutions, with the 2D and higher dimension models exclusively employing intense computational numeric algorithms ([19],[20]). Again, steady-state solutions comprise the majority of the higher dimension models, though [9] includes transients.

The work herein would be classified as a 1D, dynamic, control-oriented model by way of model-order reduction of a medium-order numeric model, with experimental

validation of sufficient accuracy and supplemental inclusion of analysis for control.

Similar practical application of mathematical modeling work is also being performed by Promislow [21, 22], though without the focus on simplification to prepare for a control-oriented application. For example, though Promislow includes convective transport, our assumption of a diffusion-dominated GDL gas transport model allows a simple steady-state analytic solution for the gas constituent distributions to be found, which facilitates stability analysis. Similar to [22], we apply quasi steady-state solutions for the fast gas species, and focus on the slow transients of the liquid. Another difference can be found in our assumption that water vapor concentration variation from saturation within the membrane electrode assembly has an important role to play in liquid and vapor water transport through the gas diffusion layers. Use of this vapor concentration model provides for diffusive transport under isothermal conditions.

The very recently published work in [23] has the similar goal of a two-phase PEMFC model for control by reducing the complexity. The assumptions and focus areas are significantly different, however, with the analysis of the water spatial distributions within the GDLs, inclusion of membrane water vapor transport, and emphasis on avoidance of flooding-induced degradation of voltage output as the focus of this work as opposed to their simplifying assumptions of lumped values for constituents in the GDL, liquid membrane transport, and emphasis on capturing the multiplicities predicted by their high-order model.

1.2.2 Fuel Cell Control

Fuel cell control is a growing research interest area, with work expanding in both component and system levels. Modeling and control by [24] and [25] focused on issues associated with control of fuel cells and support components such as compressors run parasitically by the fuel cell. Further, when discussing fuel cell control, the typical meaning is fuel cell power control and the goal is operating the fuel cell efficiently while striving to meet the power demands placed on it. Controlled variables for safe and efficient fuel cell operation include oxygen concentration, relative humidity, and power output. In [26], the control methodology attempted to address all of these varied control objectives by nesting multiple loops. Ideas in the literature for power control include setting a voltage output command to obtain cell current output to meet the power requirements (or vice versa due to the current-voltage dependency) [26], modulation of oxygen excess ratio via airflow [27], and application

of controlled DC/DC converters to convert the fuel cell output to a desired power level [28]. Airflow rate and stack current are the typical control inputs for oxygen starvation prevention [29], while temperature was used as the manipulated variable for humidity control in [26].

1.2.3 Model Order Reduction

Model order reduction has a long and well-documented history. While the list of articles relevant to model order reduction is dauntingly long, a very brief summary of some of the major points is included here to aid in the understanding of the proposed direction.

Linear MOR: The vast majority of model order reduction is done on linear or linearized systems, in the state space, and has as a fundamental aspect a change of coordinates. A basic example of this is the eigenvector-based method of using a similarity transformation matrix with columns formed by the unit eigenvectors of the system. Each eigenvalue of the system provides information regarding the speed of its respective mode. In **modal truncation**, the fastest modes are removed from the system. At issue, however, is whether the modes should be removed in order from fastest to slowest, or if there might be slower modes that contribute less than one of the faster modes.

In Moore's classic work [30](1981), he introduced the usage of Hankel singular values (which he termed 'second-order modes') and the balanced realization, which is, again, a similarity transformation of the original system. This balanced version of the system is obtained by determining the transformation that renders the observability and controllability grammians diagonal and equal. The diagonal elements of these grammians are the Hankel singular values of the system. The magnitude of the Hankel SVs indicates the significance of that mode to the input-output dynamics. The modes judged to be non-contributing can be reduced through either truncation or residualization. This method represents a variation on eigen-based concepts, because the Hankel SVs are the square root of the eigenvalues of the product of the controllability and observability grammians. The idea of an internally balanced system is that if a realization can be found where the input-output relationships are equivalent within each mode, then it will be possible to determine which modes contribute the least to both input and output simultaneously. The advantage over the modal truncation is that the balanced realization considers the inputs and outputs selected, and uses that information to rank the mode contribution.

Other important work in the field includes Wilson's historic work [31](1970) focusing on minimizing a quadratically-weighted output error (optimality), as well as Skelton's [32] use of a quadratic optimality criterion to decompose the error contribution of each state, then truncating those that contribute least to the error [33]. Loeve [34] is credited with creation of the data-based Karhunen-Loeve method (aka POD - Proper Orthogonal Decomposition). Glover [35] has become synonymous with analysis of the Optimal Hankel Norm approximation, and its infinity-norm bound. An attractive aspect of the Optimal Hankel Norm approximation method is that its error bound is half that of the balanced realization methods.

It would not be unusual to specify a classification of model order reduction by its usage of projections onto a subspace spanned by a basis of modes as the foundation of the method. This classification would cover the majority of methods used in practice. Within this lower-order-subspace *projection* classification, modal truncation, balanced truncation, the POD, and the moment-matching Krylov subspace methods are the most commonly applied.

The remaining group of model order reduction techniques is much harder to classify than the subspace-projection methods described above. For lack of a better term, these methods might be called the non-subspace-projection methods. They include singular perturbation (within which balanced residualization would be included), the Optimal Hankel norm model reduction [35], and the equally applicable to linear and nonlinear systems model order reduction algorithm (MORA) [36].

In balanced residualization, the first step is, like balanced truncation, to find a balanced realization of the system and determine which states of the new system contribute least to the input-output relationships by analysis of the Hankel singular values (typically, these states are the 'fast' states of the new system). These fast states are not truncated, however. They are re-introduced into the reduced system, maintaining the DC gain, by setting their derivatives to zero.

A somewhat unique method of model order *deduction* (MODA), created by Stein and Wilson [37], takes a notably different tack to determine a sufficient model order for the application. In MODA, instead of reducing a model, given the desired range of frequency of operation, the model is built-up, mode by mode, until *sufficient* accuracy of the highest frequency mode within the range of interest is obtained. Accuracy is judged by how much the eigenvalues of the modes change each time the order of the model is increased through addition of the model accuracy-improving modes. The error bound for MODA, set in terms of allowable eigenvalue variation, must be set as a design specification prior to model creation.

11

Work in linear system order reduction is still an active topic of research, as evidenced by recent papers from Lall [38] and Rowley [39]. With Lall working on applications of POD to mechanical systems and Rowley presenting a combined "Balanced POD" method of determining approximate balanced truncations to gain computational efficiency.

Nonlinear MOR: The application of model order reduction to nonlinear systems is still in the steep learning curve phase, and much of the work seeks to draw upon the large number of linear systems tools available. Lall [40],[41] and Wilson [42] quasilinearize (through describing functions or Taylor series expansion), and then apply POD or balanced realization techniques. The Trajectory Piecewise Linear (TPWL) approach is also seeing significant research activity ([43],[44]) in conjunction with truncated balanced realization. It should be noted that the MORA of Stein and Louca is applicable to nonlinear systems, adds minimal additional computation effort, but does not have clearly defined error bounds.

For the purposes of foreshadowing the direction of this research, it is important to note that most MOR methods do not preserve the meaning of the states of models created from first principles. The reduced system states exist as combinations of the original states. After transformations and truncations/projections, it is, in general, not possible to assign physical meanings to the reduced model states (though in chance applications, it is sometimes the case that a state chosen from first principles happens to be close to a remaining mode of the reduced system).

1.2.4   Contributions and Outline

The contributions to the areas of fuel cell modeling, model simplification, and control are as follows:

- A bond graph representation of a channel-membrane-channel model is created to develop system operation physical intuition and to implement the Model Order Reduction Algorithm.
- The energy-based MORA is used in a novel way to predict the form of the analytic solutions of a set of interdependent 2nd-order PDEs. In a sense, predicting the degree of linearity of the solutions.
- MORA results on the nonlinear system are shown to collaborate well with a modal analysis performed on the linearized system to show the time separation between the liquid and gas species modes.
- Error, sensitivity, and singular perturbation analyses are performed to evaluate the coupling effect on gas diffusivity as a function of liquid water present.

- Justified approximations for effective diffusivity and capillary pressure are made to create a semi-analytic solution model that is shown to predict voltage degradation due to anode flooding and reactant response to input changes.
- Control analyses for stability and controllability-observability are performed on the SAS model showing that the system is stabilizable.
- A control objective placing the active two-phase water front at $x = L$, with proof of concept simulation, is proposed that reduces hydrogen waste and eliminates liquid accumulation in the anode channel.
- Given the control objective proposed, the SAS is expanded to include a spatially and temporally varying two-phase water front within the GDL (water vapor switching solution).
- The SAS model is structured such that it can be modified easily to include along-the-channel spatial variation and temperature variation.
- Computational cost has been decreased by over 44%, allowing increased spatial resolution of the numeric portion of the solution.

The remainder of this dissertation is organized as follows. Chapter 2 contains the background information for the continuous model formulation, including the first-principles based PDEs and the boundary conditions. Chapter 3 explains the model order reduction methodology used, including derivation of the the the channel-membrane-channel bond graph and interpretation of the applied MORA and modal decomposition parallel results. Chapter 4 covers the derivation of the semi-analytic solution model (including the switching solution), model validation, and a brief review of potential applications. Chapter 5 has the control analyses showing the stability of liquid water in the GDL, the stabilizability of the overall anode system, and the range of possible equilibria for liquid and water vapor. This chapter concludes with the control objective concept. Finally, conclusions and suggested next steps are listed in Chapter 6, followed by the Appendix.

Chapter 2

Full-Order Model Formulation

The fuel cell model described in this chapter is a slightly modified version from McKay, et al ([3]). It combines GDL, channel, and membrane transport models using boundary conditions to relate each domain. The channel constituent dynamics are included because it is through the channels (lumped with the inlet and outlet manifolds) that a controller will influence the GDL states (liquid water volume, reactant and water vapor concentrations). The water (liquid and vapor) dynamics within the gas diffusion layers (GDL) are tightly coupled through the evaporation/condensation rate. Additionally, the liquid water becomes a nonlinearly distributed parameter that inhibits reactant gas and water vapor diffusion. The channel conditions are the boundary conditions for the PDEs that describe the behavior of the GDL constituents. GDL dynamics are important since the GDL represents the path by which the channel conditions influence the membrane states, and thus the cell performance. The first principles based constituent dynamics within the GDL used herein, including the capillary flow and porous media gas transport mechanisms, as well as the boundary conditions, follow closely to that of [5].

2.1   Model of the Gas Diffusion Layer

Because creation of a physically intuitive model facilitates controller design and tuning, and since it is currently infeasible to obtain direct, realtime measurements of the critical variables at the membrane and in the GDL, a low-order and compact model of the multi-component (reactants, water), two-phase (vapor and liquid water), spatially-distributed and dynamic behavior across the gas diffusion layer (Fig. 2.1) has been investigated. The time-varying constituent distributions in the GDL of each

14

electrode are described by three second-order parabolic PDEs for reactant (oxygen in the cathode and hydrogen in the anode) concentration, water vapor concentration, and liquid water. Instantaneous electrochemical reactions on, and the mass transport through, the catalyst-covered membrane couple the anode and cathode behaviors and, together with the channel conditions, provide the time-varying boundary values for these PDEs.

2.1.1 Model Assumptions

The Semi-Analytic Solution (SAS) model developed herein has the same capability of a completely numeric model to capture the effects of changes to inputs/outputs on voltage estimation. The model combines analytic solutions for the spatial distributions of gases with a numeric solution for the liquid water and was obtained using the following assumptions:

- The model is spatially isothermal, but temperature is allowed to vary in time as this affects inlet and outlet water flow rates as well as the voltage model output. Although the effect of spatial temperature gradients are shown to be important [45], the simple tunable isothermal model considered was shown capable of predicting behavior for a reasonable range of conditions.
- Convective (bulk) flow of the gases in the GDL is neglected due to the assumption of very low velocities normal to the membrane.
- Mass transport is in 1D, normal to the membrane, and we neglect the GDL-channel interface variations due to backing plate land and channel interaction. Variation along the channel is also neglected (except as an example of a potential model application in Sec. 4.3.1)
- Due to the generation of product water in the cathode GDL, and the fully humidified inlet flow, it is assumed that two-phase water conditions and liquid capillary flow are always present in the cathode. Therefore, the single-phase water regime is not considered on the cathode side.
- Water transport out of the anode channel is assumed to be in vapor form due to the low flow rates that will be employed to ultimately achieve high efficiency through high hydrogen utilization during small flow-through conditions. For a high-velocity channel flow system, this assumption may not be valid [46].
- Though the evaporation model of [47] includes evaporation even under fully saturated vapor conditions due to the inclusion of compressibility, we employ the simplifying evaporation/condensation model from [5], where mass transfer between the liquid and vapor phases is proportional to the difference between the water vapor concentration and the concentration at the saturation pressure, i.e. incompressibility is assumed.

- It is assumed that the front between one and two-phase water will always be two-phase on the membrane side of the front, and if the front is within the GDL, the entire range on the channel side of the front will be single-phase (i.e. there are no islands of two-phase water).
- There is assumed to be a small, constant, and negligible resistance to liquid flow across the GDL-channel border, represented by a constant S_δ in subsequent equations. Though a modification of this boundary condition would shift the liquid water distribution, it is not expected to significantly alter the qualitative findings of this research.

Assuming a one-dimensional treatment of the GDL processes, let x denote the spatial variable, with $x = 0$ corresponding to the membrane location and $x = \pm L$ corresponding to the channel locations ($+L$ at anode channel, -L at cathode channel) per Fig. 2.1, and let t denote the time variable. The model includes channel and GDL for both anode and cathode, with differences between the electrodes appearing only in sign, rate of reactant consumption, and the generation of water vapor on the cathode side. This water generation is lumped into the membrane transport to form the $x = 0$ cathode boundary condition, and thus does not change the form of the equations, only the specific boundary value.

The state variables are as follows:

- $c_{v,an}(x,t)$ and $c_{v,ca}(x,t)$ are the concentrations of water vapor at time t at a cross-section of GDL located at x, $0 \le x \le L$ (anode) or $-L \le x \le 0$ (cathode);
- $c_{H_2}(x,t)$ and $c_{O_2}(x,t)$ are the reactant concentrations at time t at a cross-section of GDL located at x, $0 \le x \le L$ (anode-H_2) or $-L \le x \le 0$ (cathode-O_2);
- $s(x,t)$ is the anode GDL fraction of liquid water volume V_L to the total pore volume V_p, $s = \frac{V_L}{V_p}$, commonly referred to as the water saturation. The variable s is thus a concentration-like variable for the liquid water at time t, at a cross-section of GDL located at x, $0 \le x \le L$.

The following intermediate variables are useful:

- $N_v(x,t)$ is the water vapor molar flux (mol/m^2/s) at time t at a cross-section of the GDL located at x, $0 \le x \le L$ (anode) or $-L \le x \le 0$ (cathode);
- $W_l(x,t)$ is the liquid water mass flow (kg/s) at time t at a cross-section of the GDL located at x, $0 \le x \le L$.
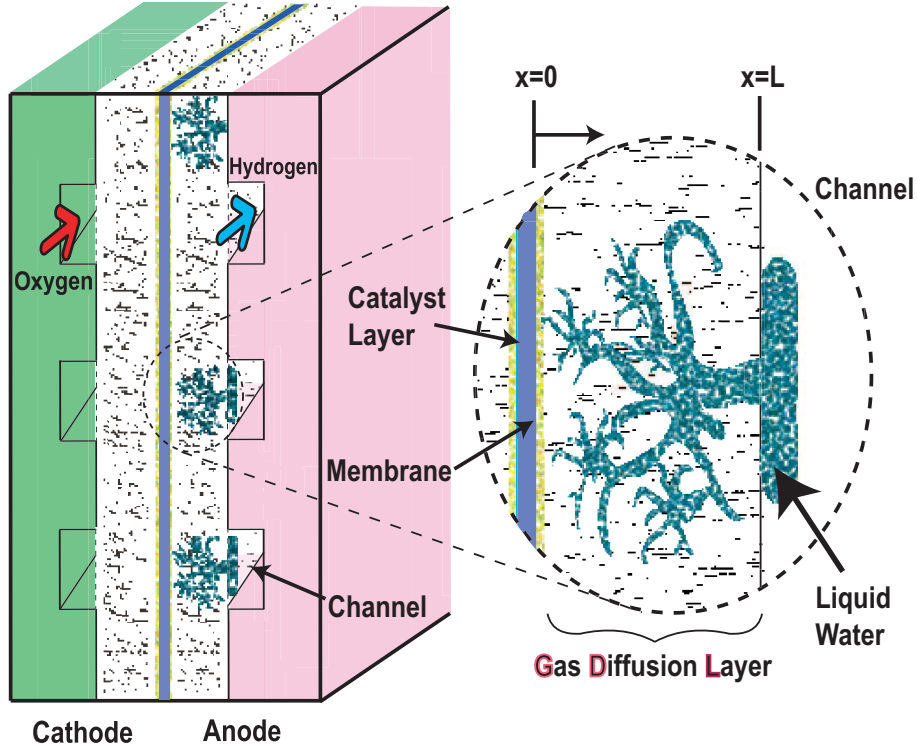
Figure 2.1: Basic concept of water transport in a fuel cell.

2.1.2 Continuous 1D Model Formulation

The molar fluxes are driven entirely by the presence of a concentration gradient (i.e. diffusion), since bulk flow (convection) is neglected:

$$N_{j,e} = -D_{j,e}(s)\frac{\partial c_{j,e}}{\partial x}, \tag{2.1}$$

where the j subscript refers to any of the gas constituents within the fuel cell, and the subscript e indicates that the equation is applicable for both anode (an) and cathode (ca) electrodes. The $D_{j,e}(s)$ are the effective diffusivities for the gases which depend on the liquid fraction, s, since liquid water reduces diffusivity in the GDL by occupying pore space, and are defined by $D_{j,e}(s) = D_{j,\varepsilon}(1-s)^m$. $D_{j,\varepsilon}$ captures the influence of porosity on diffusivity,

$$D_{j,\varepsilon} = D_j \varepsilon \left(\frac{\varepsilon - 0.11}{1 - 0.11}\right)^{0.785}, \tag{2.2}$$

where D_j is the gas diffusion coefficient and $m = 2$ based on [5].

17

The reactant gas conservation equations are of the form,

$$\frac{\partial c_j}{\partial t} = -\frac{\partial N_j}{\partial x}, \tag{2.3}$$

where j in (2.3) is limited to O_2 or H_2. The water vapor conservation equations are of the form,

$$\frac{\partial c_{v,e}}{\partial t} = -\frac{\partial N_v}{\partial x} + r_v(c_{v,e}), \tag{2.4}$$

where r_v is the evaporation rate defined as,

$$r_v(c_{v,e}) = \begin{cases} \gamma(c_v^{sat} - c_{v,e}) & \text{for } s > 0 \\ \min\{0, \gamma(c_v^{sat} - c_{v,e})\} & \text{for } s = 0 \end{cases}$$

where γ is the volumetric evaporation coefficient and c_v^{sat} is the vapor concentration associated with the water vapor saturation pressure. Note that evaporation can only occur if there is liquid water ($s > 0$) in the GDL, yet condensation can occur even if $s = 0$ (under supersaturated conditions).

Under the isothermal conditions assumed in this model, once the production or transport of vapor exceeds the ability of the vapor to diffuse through the GDL to the channel, the vapor condenses at the rate determined by γ, hence supersaturated conditions ($c_v(x) > c_v^{sat}$) are allowed. The mass flow of liquid water is driven by the gradient in capillary pressure (p_c) due to build-up of liquid water in the porous medium,

$$W_l = -\varepsilon A_{fc}\rho_l \frac{KK_{rl}}{\mu_l}\frac{\partial p_c}{\partial x}, \tag{2.5}$$

where μ_l is the liquid viscosity, ρ_l is the liquid water density, A_{fc} is the fuel cell active area, and K is the material-dependent absolute permeability. The relative liquid permeability is a cubic function of the reduced water saturation ($K_{rl} = S^3$) [5], and p_c is a function of a third-order polynomial in $S(x,t)$ (Leverett J-function $J(S) = 1.417S - 2.12S^2 + 1.263S^3$) [5]), where

$$S(x,t) \triangleq \begin{cases} \frac{s(x,t)-s_{im}}{1-s_{im}} & \text{for } s \geq s_{im}, \\ 0 & \text{for } s < s_{im}. \end{cases} \tag{2.6}$$

The immobile saturation, s_{im}, works as stiction, i.e. there is no liquid flow unless the water saturation exceeds s_{im}. It should be noted that the electrode subscript e on S and s is hereafter dropped for convenience, since the development is the same for both anode and cathode.
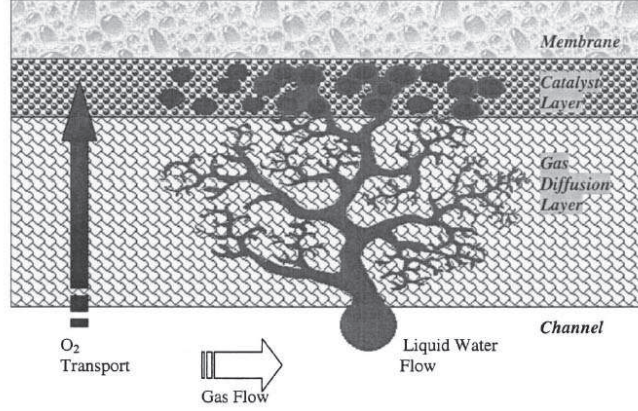
Figure 2.2: Capillary flow of liquid water through the gas diffusion layer [5]

Combining (2.1) with (2.4) provides the two second-order parabolic PDEs that govern the water vapor concentrations in the cathode and anode,

$$\frac{\partial c_{v,e}}{\partial t} = \frac{\partial}{\partial x}\left(D_{v,e}(s)\frac{\partial c_{v,e}}{\partial x}\right) + r_v(c_{v,e}). \tag{2.7}$$

It is shown in Sec. 4.1.1 that an approximation of the time varying $D_{v,e}(s)$ with $D_{v,e}(s_{im})$ yielded negligible error, and since this makes the diffusivity independent of x, it can be represented by $D_v^{s_{im}} \triangleq D_{v,e}(s_{im})$ for both cathode and anode, and the water vapor PDEs become:

$$\frac{\partial c_{v,e}}{\partial t} = D_v^{s_{im}}\frac{\partial^2 c_{v,e}}{\partial x^2} + r_v(c_{v,e}). \tag{2.8}$$

Under appropriate conditions, liquid accumulates in the GDL until it has surpassed the immobile saturation threshold (s_{im}), at which point capillary flow will carry it to an area of lower capillary pressure (toward the GDL-channel interface as shown in Fig. 2.2). To facilitate the analytic solution, (2.5) is rewritten as,

$$W_l = -\varepsilon A_{fc}\rho_l\frac{K}{\mu_l}S^3\frac{\partial p_c}{\partial S}\frac{\partial S}{\partial x}. \tag{2.9}$$

Using a least squares fit approximation,

$$\frac{K}{\mu_l}S^3\frac{\partial p_c}{\partial S} = \frac{K}{\mu_l}S^3(1.417 - 4.24S + 3.789S^2) \approx b_1 S^{b_2}, \tag{2.10}$$

19

where $b_1 = 2.42 \times 10^{-5}$ and $b_2 = 2.88$, results in

$$W_l = -\varepsilon A_{fc}\rho_l b_1 S^{b_2}\frac{\partial S}{\partial x}. \tag{2.11}$$

Conservation of liquid mass is employed to determine the rate of liquid accumulation,

$$\frac{\partial s}{\partial t} = -\frac{1}{\varepsilon A_{fc}\rho_l}\frac{\partial W_l}{\partial x} - \frac{M_v}{\rho_l}r_v(c_{v,e}), \tag{2.12}$$

where M_v is the molar mass of water.

Substitution of (2.11) into (2.12) yields the water saturation PDE,

$$\frac{\partial s}{\partial t} = \frac{\partial}{\partial x}\left(b_1 S^{b_2}\frac{\partial S}{\partial x}\right) - \frac{M_v}{\rho_l}r_v(c_{v,e}). \tag{2.13}$$

2.1.3 Boundary Conditions

The choice of boundary conditions (BC) is important for the solution of the PDE system described in the previous section. For $c_{v,e}(x,t)$, mixed Neumann-Dirichlet type BC are imposed. The channel (ch) boundary condition is,

$$c_{v,e}|_{x=\pm L} = c_{v,e}^{ch} = p_{v,e}^{ch}/\left(\mathcal{R}T_{st}\right), \tag{2.14}$$

where $\mathcal{R}$ is the universal gas constant, T_{st} is the stack temperature, and the total pressure in the anode channel, p_{an}^{ch}, is a key state of the model as it is influenced by fuel cell flow in, flow out, and GDL-channel transport. The anode membrane water vapor BC is:

$$\left.\frac{\partial c_{v,an}}{\partial x}\right|_{x=0} = -\frac{N^{mb}}{D_v^{s_{im}}}, \tag{2.15}$$

which represents the assumption that water enters the GDLs in vapor form only due to the presence of microporous layers between the membrane and GDLs [5, 48]. The membrane water molar flux N^{mb} is governed by electrosmotic drag and back diffusion, which are driven by current density $i(t)$ (A/m^2) and water vapor concentration variation across the membrane, respectively, and depend on stack temperature. The model for N^{mb} used here is taken from [3], and takes the general form:

$$N^{mb} = \overbrace{\beta_w(\lambda_{ca} - \lambda_{an})}^{\text{back diffusion}} - \overbrace{2.5\frac{\lambda^{mb}}{22}\frac{i(t)}{F}}^{\text{osmotic drag}}, \tag{2.16}$$

with

$$\beta_w = 3.5 \times 10^{-6}\alpha_w\frac{\rho^{mb}}{M^{mb}t^{mb}}\frac{\lambda^{mb}}{14}e^{\frac{-2436}{T_{st}}}, \tag{2.17}$$

20

where α_w is a tuned parameter, λ^{mb} is the membrane water content ([13],[49]), λ_e are the water contents on either side of the membrane, and F represents Faradays constant. The λ_e are polynomial functions of the $c_{v,e}^{mb}$, which are the water vapor concentrations on either side of the membrane ($x = 0$). The material and physical parameters of the membrane enter through its density (ρ^{mb}), molecular weight (M^{mb}), and thickness (t^{mb}).

At the catalyst layer of the cathode side, product water is generated as a function of $i(t)$, and thus the Neumann BC contains the net of N_v^{rct} and N^{mb},

$$\left. \frac{\partial c_{v,ca}}{\partial x} \right|_{x=0} = \frac{N_v^{rct} - N^{mb}}{D_v^{sim}}, \tag{2.18}$$

where N_v^{rct} represents the generation of product water at the cathode catalyst layer given by,

$$N_v^{rct} = \frac{i(t)}{2F}. \tag{2.19}$$

From the assumption that water transport into the GDL at $x = 0$ has no liquid component, Neumann boundary conditions are imposed for $s(x,t)$:

$$\left. \frac{\partial s}{\partial x} \right|_{x=0} = 0. \tag{2.20}$$

The setting of a physically meaningful liquid water boundary condition at the GDL-channel interface has been a challenging issue [50, 51] with the choice of either zero water saturation or zero liquid flow being typically assumed [5, 52, 53], though channel water saturation BCs of 0.01, 0.4, and 0.6 were considered in [54]. A lack of liquid flow into the channel seems physically unlikely due to the hydrophobic nature of the GDL material, and the assumption of zero water saturation ($S|_{x=0} = S_{ch} = 0$) is convenient for analysis, but does not have a solid physical interpretation. Here we consider the simplifying and convenient form of:

$$S(L,t) \triangleq \begin{cases} S_\delta & \text{for } m_{l,an}^{ch} > 0, \\ 0 & \text{for } m_{l,an}^{ch} = 0, \end{cases} \tag{2.21}$$

where S_δ represents the effect of the liquid water that accumulates on the GDL-channel interface, and the inclusion of S_δ essentially adds a means to provide resistance to flow due to accumulation of liquid in the channel. The value $S_\delta = 0.0003$ was assumed for simulation. Based on the voltage output experimental verification,

21

this assumption does not impair the model's estimation ability. However, as more information becomes available from measurement methods such as neutron imaging, this assumption may be reevaluated.
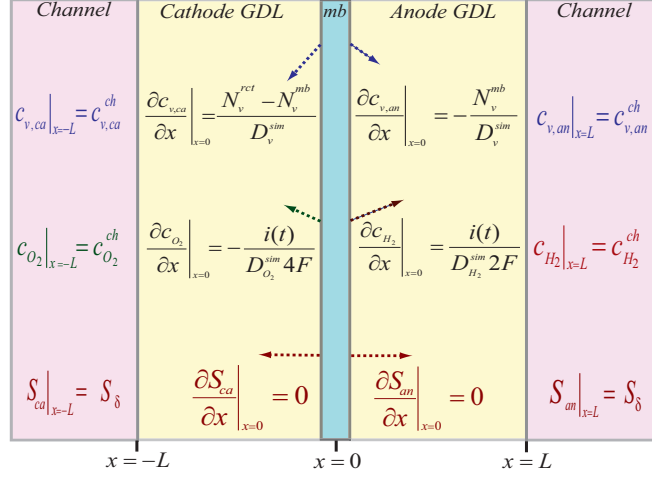
Figure 2.3: Boundary conditions for anode and cathode GDL. Time-varying Neumann BC are placed at the membrane, with time-varying Dirchlet BC at the channels (not to scale).

A graphical representation of the boundary conditions described, including appropriately similar boundary conditions imposed on the reactants H_2 and O_2, is shown in Fig. 2.3.

2.2   Channel Equations

To determine the water vapor channel dynamics, the total channel pressure must be found. The pressures, which represent the channel boundary conditions, are calculated from:

$$p_e^{ch} = \sum_j p_j^{ch}, \tag{2.22a}$$

$$p_j^{ch} = \frac{m_j^{ch} \mathcal{R} T_{st}}{M_j V^{ch}} \qquad (j \neq v), \tag{2.22b}$$

$$p_{j,e}^{ch} = \min \left\{ \frac{m_{w,e}^{ch} \mathcal{R} T_{st}}{M_j V^{ch}}, p_v^{sat} \right\} \quad (j = v), \tag{2.22c}$$

where the subscript j represents each of the gaseous elements present (H_2 and water vapor for the anode, and O_2, N_2, and water vapor for the cathode).

22

The governing equations for the reactants and water in the channel are:

$$\frac{dm_j^{ch}}{dt} = W_j^{in} + W_j^{GDL} - W_j^{out}, \tag{2.23a}$$

$$\frac{dm_{w,e}^{ch}}{dt} = W_{v,e}^{in} + W_{w,e}^{GDL} - W_{v,e}^{out}, \tag{2.23b}$$

where

$$W_j^{in} = \lambda_j \frac{i(t)}{2\eta F} A_{fc} M_j, \tag{2.24}$$

with the *in* and *out* subscripts referring to channel inlets and outlets, and η is a factor that depends on the electrochemical reaction so that $\eta = 1$ for H_2 and $\eta = 2$ for O_2, and λ_j is the excess ratio of the reactant j.

In the general case, both anode and cathode will have humidified inlet streams, with the relative humidity (RH_e^{in}) and the inlet flow rates $(W_{air}^{in}$ and $W_{H_2}^{in})$ prescribed, thus,

$$W_{v,ca}^{in} = \frac{P_{v,ca}^{in}}{P_{air}^{in}} \frac{M_v}{M_{air}} W_{air}^{in} \quad \text{and} \quad W_{v,an}^{in} = \frac{P_{v,an}^{in}}{P_{H_2}^{in}} \frac{M_v}{M_{H_2}} W_{H_2}^{in} \tag{2.25}$$

where $P_{v,e}^{in} = RH_e^{in} P^{sat}$, and $P_{H_2}^{in}$, P_{air}^{in} are the pressures of the dry inlet gases. The cathode exit flow rate to the ambient (amb) is modeled as a linearly proportional nozzle equation,

$$W_{ca}^{out} = k_{ca}^{out}(p_{ca}^{ch} - p^{amb}), \tag{2.26}$$

whereas the anode exit flow rate,

$$W_{an}^{out} = \bar{u} \cdot k_{an}^{out}(p_{an}^{ch} - p^{amb}), \tag{2.27}$$

has a controllable valve flow $0 \le \bar{u}(t) \le 1$ to remove water and, unfortunately, hydrogen. $\bar{u} = 0$ represents a *dead-ended* anode arrangement, which is commonly paired with a periodic purge cycle $(\bar{u} = 1)$ for water removal. For $0 < \bar{u} < 1$, this becomes a *flow through* anode water management system. The model verification of [55] was from experimentation that employed the dead-end/purge system, the analysis in this work is applicable for both dead-end and flow through conditions.

The constituent exit mass flow rates are found from,

$$W_j^{out} = \frac{m_j^{ch}}{m_{gas,e}^{ch}} W_e^{out}, \tag{2.28a}$$

$$W_{v,e}^{out} = W_e^{out} - \sum_j W_j^{out}, \tag{2.28b}$$

where $m_{gas,e}^{ch} = m_j^{ch} + p_{v,e}^{ch} V_{an}^{ch} M_v / (\mathcal{R}T_{st})$, and j is H_2 for the anode, but addresses both O_2 and N_2 for the cathode.

The reactant and water mass flow rate from the GDL to the channel are:

$$W_j^{GDL} = -\varepsilon A_{fc} M_j \left(D_j(s) \frac{\partial c_j}{\partial x} \right) \Bigg|_{x=\pm L}, \tag{2.29a}$$

$$W_{w,e}^{GDL} = -\varepsilon A_{fc} \left(\rho_l b_1 S^{b_2} \frac{\partial S}{\partial x} + M_v D_v(s) \frac{\partial c_{v,e}}{\partial x} \right) \Bigg|_{x=\pm L}. \tag{2.29b}$$

Using the dynamic water mass balance in the channel (2.23b), the liquid water in the channel is found by assuming that any water in the channel in excess of the maximum that can be held in vapor is liquid,

$$m_{l,e}^{ch} = max \left[0, m_{w,e}^{ch} - c_v^{sat} M_v V_e^{ch} \right]. \tag{2.30}$$

This is equivalent to assuming an instantaneous evaporation rate for the channel, and a maximum channel relative humidity of 100%. The channel model structure differs from that of the porous medium GDL, which has an evaporation/condensation rate, and water vapor concentration in excess of saturation is allowed. This differing treatment of the evaporation is simplifying since the channel then does not require separate water vapor and liquid states. For the voltage model of [3], liquid water mass is of interest, and the approximation of instantaneous evaporation has a very negligible effect on the voltage estimation.

2.3   Discretization and Numerical Solution

The one-dimensional system of interconnected parabolic PDEs and support equations of (2.3)-(2.13), combined with three similar PDEs describing the spatial and temporal evolution of the reactants (H_2, O_2), water vapor, and water saturation was modeled and discretized into 3 sections for each electrode and parameterized using data from an experimental fuel cell [3]. The discretization procedure is described here because analysis of the linearized numeric model is key background work and allows direct comparison with the developed semi-analytic model.

The 24 states of the 3-section discretized fuel cell model (includes anode and cathode) can be grouped as follows:

- Concentrations of Gas constituents in the GDLs: 13

    - 3 each sections of O_2, H_2, anode water vapor, and cathode water vapor, plus 1 lumped section for N_2.

- Liquid constituents in GDL: 6

    - 3 sections of liquid water fraction for each GDL.

- Dynamics states in channels: 5

    - Concentrations of O_2, N_2, and water vapor in the cathode channel and concentrations of H_2, and water vapor in the anode channel.

2.3.1 Difference Equations

It is because the boundary conditions for each of the constituents are Neumann type that the discretization is performed on three pairs of first-order DEs (2.1)-(2.9) instead of three second-order PDEs. The forward-difference method is used for the discretizations of the flux and flow equations,

$$N_{H_2}[k] \simeq -D_{H_2}(s)\frac{c_{H_2}[k+1] - c_{H_2}[k]}{\delta x}, \tag{2.31}$$

$$N_v[k] \simeq -D_v(s)\frac{c_{v,an}[k+1] - c_{v,an}[k]}{\delta x}, \tag{2.32}$$

$$W_l[k] \simeq -b_1 S[k]^{b_2}\frac{s[k+1] - s[k]}{\delta x}, \tag{2.33}$$

where $\delta x = x[k+1] - x[k]$, and the k represents a counter for the discretized sections.

Next, since the fluxes across the membrane are included in the model, and form the BC, the difference equations relating the states to the fluxes are formed using the backward-difference method:

$$\frac{dc_{H_2}[k]}{dt} \simeq -\frac{N_{H_2}[k] - N_{H_2}[k-1]}{\delta x}, \tag{2.34}$$

$$\frac{dc_{v,an}[k]}{dt} \simeq -\frac{N_v[k] - N_v[k-1]}{\delta x} + r_v(c_{v,an}[k]), \tag{2.35}$$

$$\frac{ds[k]}{dt} \simeq -\frac{W_l[k] - W_l[k-1]}{\delta x} - \frac{M_v}{\rho_l} r_v(c_{v,an}[k]). \tag{2.36}$$

Dymola^{TM} software is used to implement the resulting lumped-parameter, ordinary differential equations of the discretized system, which will be referred to as the Coarse Numeric Solution (CNS), and will be compared with respect to accuracy and computational load to the semi-analytic solution presented in Chap. 4.

Chapter 3

Model Order Reduction

The model order reduction methodology implemented was chosen based on the criteria of applicability to nonlinear systems and the capability to maintain the physical meanings of the states. The former requirement is simply because our system is nonlinear, and the latter because it is desirable to obtain physical insights into the operation of the fuel cell to be able to justify assumptions and explain results. For baseline comparison purposes, balanced truncation model order reduction was performed on the linearized system with results showing that a 56% order reduction to 11 states with negligible loss in estimation accuracy. It is therefore expected that this research can create a control-oriented model with less than 12 states for equivalent spatial discretization.

3.1 Derivation of the Bond Graph Equations

The above requirements suggest application of the Model Order Reduction Algorithm (MORA) from [36], which requires both an understanding of the model on an element-by-element basis and knowledge of the *effort* and *flow* of each element over time. The bond graph is a modeling tool that lends itself conveniently to the MORA's energy-based analysis because effort and flow are easily obtained. However, for bond graph implementation, each equation in the mathematical model must first be cast in a form that is applicable to the building blocks of the bond graph.

The derivation and background for the following physical model equations can be found in Chap. 2. The discrete model therein consists of equations for gas diffusion, gas concentration time rate of change, capillary pressure-driven liquid water flow, evaporation, chemical reactions, and a number of conditional and empirical

equations governing membrane mass transport. In this section, the equations modeling the physical system are used as the starting point for the bond graph model creation. Each subsection in this section will explain how the bond graph for each model phenomenon is derived.

3.1.1 Gas Species Concentration (Capacitance Model)

The rate of change of molar concentration ($c_j = \frac{p_j}{\mathcal{R}T}$) of gas species j is:

$$\frac{dc_j}{dt} = \frac{\partial N_j}{\partial x} + r_j \tag{3.1}$$

where the general electrode subscript e has been dropped for convenience and the species denoted by j correspond to the oxygen O_2 and vapor v from the cathode, and to the hydrogen H_2 and vapor v from the anode. The reaction term r_j is zero for the oxygen and hydrogen cases, whereas for the vapor case it captures the evaporation rate $r_j = \gamma \left(p_v^{sat}/(\mathcal{R}T) - c_v \right)$, where p_v^{sat} is the saturation vapor pressure.

In discrete form (3.1) is written:

$$\frac{dc_j[k]}{dt} = \frac{1}{\delta x}(N_j[k] - N_j[k-1]) + r_j, \tag{3.2}$$

where [k] and [k-1] represent any two sequential sections of the discrete model.

As can be seen from (3.2), the rate of change of concentration (mol/m³/s) becomes a function of the difference in molar fluxes across the section boundaries for the particular gas species. Additionally, the local reaction (evaporation) rate r_j is included for the water vapor model. The O_2 and H_2 reactions are calculated as molar fluxes (mol/m²s), and thus enter the equation through the across-boundary flow.

The bond graph constitutive law for a *capacitance* is:

$$\frac{d\mathbf{e}[k]}{dt} = \frac{1}{C}(\mathbf{f}[k] - \mathbf{f}[k-1] + \mathrm{MSf_{rct}}), \tag{3.3}$$

where for our case $C = \delta x = (t^{GDL}/3)$ (the length one section), $\mathrm{MSf_{rct}}$ is a modulated flow source that can represent a variety of flow inputs, but is non-zero for this application only when j is water vapor, v. From these observations, a choice of molar flux as the *flow* variable, concentration as the *effort* variable, and section length for the *capacitance* for the gas mass transport is logical, and preserves physical meaning.

Finally, while a choice of pressure for the effort variable would also be acceptable, concentration was chosen simply because this is an existing state variable.

3.1.2 Gas Species Diffusion (Resistance Model)

Diffusion of gases takes place in the anode and cathode gas diffusion layers. On the anode side, relative diffusion of hydrogen and vapor must be considered, while the cathode side model must take into account the relative diffusion of oxygen, nitrogen, and vapor. This model is simplified by assuming that the presence of N_2 in the mixture does not significantly affect the diffusivity of O_2 and vapor.

The diffusion of gas species in the diffusion layer is a function of the concentration gradient, transferring gas from regions of higher concentration to regions of lower concentration:

$$N_j = -D_j(s)\frac{\partial c_j}{\partial x}. \tag{3.4}$$

As shown in (3.4), the molar flux, N_j (mol/m^2/s), depends on the diffusion coefficient, $D_j(s)$.

The discrete version of (3.4) is realized with N_j being a function of the difference in the concentration between neighboring sections:

$$N_j[k] = \frac{-D_j(s[k])}{\delta x}(c_j[k+1] - c_j[k]). \tag{3.5}$$

The general *resistance* constitutive law utilized in bond graphs is:

$$\mathbf{f}[k] = \frac{1}{R[k]}(\mathbf{e}[k] - \mathbf{e}[k+1]) \tag{3.6}$$

where for this application the flow resistance is represented by a modulated resistance:

$$R[k] = MR[k] = \frac{\delta x}{D_j(s[k])}. \tag{3.7}$$

A *modulated resistance* is necessary because the diffusivity of gas constituents in the GDL is affected by the volume of liquid water present, represented by $s[k]$, giving rise to the discrete *effective* diffusivity [5]:

$$D_j(s[k]) = D_j\varepsilon\left(\frac{\varepsilon - 0.11}{1 - 0.11}\right)^{0.785}(1 - s[k])^2, \tag{3.8}$$

where $s[k] = \frac{V_l[k]}{V_p}$, D_j is the diffusivity constant for the species j (which is dependent

upon the molecular size of j).

3.1.3   Liquid Water Storage (Capacitance Model)

The volume of liquid water (V_l) in each GDL section is determined by the capillary liquid water volumetric flow rate, Q_l, and the evaporation rate, r_v:

$$\frac{dV_l}{dt} = Q_l^{in} - Q_l^{out} - \frac{r_v V_p M_v}{\rho_l},$$
(3.9)

where the evaporation (condensation) rate governs the creation of liquid water micro-droplets (considered to be evenly distributed at any x), and where conditions necessary for water droplet formation are assumed to have been met [5]. For simplification of the model, dynamics associated with the formation of the liquid water droplets have been neglected.

In order to cast our model into a form that is conducive to calculation of "power equals the product of *effort* and *flow*", the time rate of change of liquid water volume should be translated into a dynamic capillary pressure relationship with volumetric flow.

As a pore fills with liquid water, the capillary pressure increases, causing the water to flow to an adjacent pore with less water. This process creates a flow of liquid water through the GDL, finally resulting in the incursion of liquid into the channel. Capillary pressure results from surface tension of the water droplets, and is calculated as follows:

$$p_c = \beta_{pc} g_{NL}(S) \,,$$
(3.10)

where β_{pc} is a constant that captures the geometry of the surface tension between the water and air, the porosity, and the permeability of the GDL (details can be found in [5]). The nonlinear function $g_{NL}(S)$ is an empirically-fit third-order polynomial in S commonly used to describe the relationship between capillary pressure and the amount of liquid water present,

$$g_{NL}(S) = 1.417S - 2.12S^2 + 1.239S^3.$$
(3.11)

In this model, gravitational effects on the liquid water are considered negligible due to the liquid water surface tension interaction within the fibers of the GDL.

Taking the time derivative of (3.10), it can be shown that the time rate of change of the capillary pressure is related to the volumetric flow by a discrete equation of

the form:

$$\frac{dp_c[k]}{dt} = \beta_Q g'_{NL}(S,k)(Q_l[k] - Q_l[k-1] - r_l[k]),\qquad(3.12)$$

where β_Q represents a constant that depends upon surface tension, permeability, and GDL porosity. The nonlinear function $g'_{NL}(S,k)$ is the derivative of $g_{NL}(S,k)$ from (3.10) with respect to S. Further, the condensation rate r_l is a conversion from r_v to relate molar to mass condensation rates $(\text{m}^3/\text{s})(3.15)$.

Following the pattern of the previous subsections, the next step is to translate (3.12) into a bond graph compatible form. While (3.12) could be implemented using a modulated capacitance, simulations have shown that a simplification can be obtained by using the mean value for the applicable range of $g'_{NL}(S)$. This direction is justified by noting first that per [5], our model assumes no liquid water flow until 10% of the pore volume is filled with liquid water. At that point capillary action causes the liquid to flow into the next section, significantly reducing the liquid water fill rate for the original section, while notably increasing the fill rate for the next. The practical range of S is small enough after liquid flow begins to justify use of the mean value, therefore $g'_{NL}(S,k)$ becomes $\bar{g}$.

Then, with the evaporation modeled as a modulated flow source, the capillary pressure equation can now be modeled as a *capacitance* in a bond graph model:

$$\frac{d\mathbf{e}[k]}{dt} = \frac{1}{C}(\mathbf{f}[k-1] - \mathbf{f}[k] - \text{MSf}_r).\qquad(3.13)$$

Where the *capacitance* becomes:

$$\frac{1}{C} = \beta_Q \bar{g},\qquad(3.14)$$

and the molar liquid evaporation rate is represented by a modulated flow source:

$$MSf_r = r_l = \frac{M_v V_p}{\rho_l} r_v.\qquad(3.15)$$

3.1.4 Liquid Water Transport (Resistance Model)

The remaining equation to be modeled in bond graph form is the liquid water flow. Parameters that affect the mass flow rate of liquid water are flow area, permeability, viscosity and density of liquid water, and the section thickness. These factors will naturally influence the resistance to flow for this element. It is, however, the presence

of a liquid water volume gradient that drives the liquid water flow. Capillary pressure and liquid water volume are related through (3.10).

The physics of the liquid flow phenomenon are described by:

$$Q_l = \beta_{wl} S^3 \left(\frac{\partial p_c}{\partial x} \right), \tag{3.16}$$

where p_c is capillary pressure, $S = \left(\frac{s - s_{im}}{1 - s_{im}} \right)$ is the reduced water saturation, β_{wl} is a constant that embodies flow area, permeability, density, and viscosity, and $\partial p_c / \partial x$ describes the influence spatial variation of capillary pressure has on volumetric flow rate.

Similar to the gas species diffusion bond graph equation, an application of a *modulated resistance*, in discrete form, is appropriate:

$$\mathbf{f[k]} = \frac{1}{MR[k]} (\mathbf{e}[k] - \mathbf{e}[k+1]). \tag{3.17}$$

In the bond graph model, the MR will be a function of several system parameters (listed below in the explanation of β_R), and the continuously varying liquid water volume:

$$\frac{1}{MR[k]} = \beta_R S^3, \tag{3.18}$$

where β_R is a constant that depends upon flow area, permeability, water viscosity, section thickness and porosity, and surface tension([5]). The volumetric flow rate is calculated from:

$$Q_l[k] = \frac{1}{MR[k]} (p_c[k] - p_c[k+1]). \tag{3.19}$$

Capillary pressure as the *effort* variable and volumetric flow rate as the *flow* variable were natural choices, as was the liquid water volume as the modulus.

Finally, a conditional statement must be included to prevent capillary action from starting unless the liquid water volume reaches 10% of the pore volume (the minimum condition for flow suggested in [5]).

3.2 The Bond Graph Model

The goal of this model order reduction is to determine the minimum number of sections required to accurately model flooding. Therefore, a repeatable bond graph model for one section would be useful.
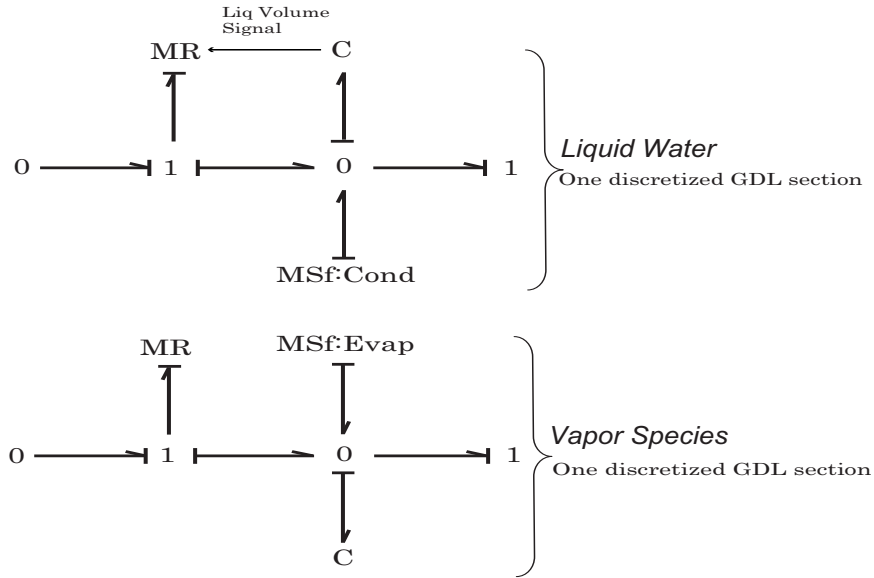
Figure 3.1: Bond Graph Building Block for one Discrete GDL Section

Using the relationships from Section 3.1, a single section bond graph submodel was created (Fig. 3.1). With this submodel, a GDL discretization for a variety of resolutions can be easily accomplished.

Flow through the GDL is bounded on one side by the channel, and on the other by the catalyst-coated membrane. These boundary conditions are clarified in this section.

The conditional and empirical equations for the membrane water transport do not fit into standard bond graph form, so function blocks were built to accommodate them. The air, hydrogen and water vapor supplied to the gas distribution channels are easily modeled as flow sources, where the amount supplied can be controlled to supply the desired O_2 and H_2 excess ratios. Similarly, evaporation is modeled as a modulated flow source, with presence of liquid water as the fundamental prerequisite and the modulus being the product of the evaporation coefficient and water vapor pressure relative to the saturation pressure.

The boundary conditions for the molar fluxes at the GDL-catalyst interface are equal to the chemical reaction rates and the membrane water transport, which depends on the GDL water concentrations at the catalyst c_v^{mb} and the current drawn from the stack I_{st} (2.16,2.19). The membrane water transport and reaction rates are thus modeled as modulated flow sources. The active signals are stack current for reaction rates, including generation of water at the cathode catalyst, and stack current and c_v^{mb} for the membrane water transport flow source.

Stacking three of the discretized sections from Fig. 3.1 for each constituent of interest, including function submodels for the membrane physics, adding evaporation flow sources, and putting in flow sources for the supply of air and hydrogen gives the model shown in Fig. 3.2. In this full-order bond graph model, the channels are modeled as dynamic boundary conditions and shown on the far left and right sides of the bond graph. The flow into and out of the fuel cell occurs in the channels. The cathode side of the model is the left half of the model, the anode side the right half. The membrane is located in the middle of the model. Positive flow in the model is defined to be from cathode channel to anode channel. Finally, for the purpose of
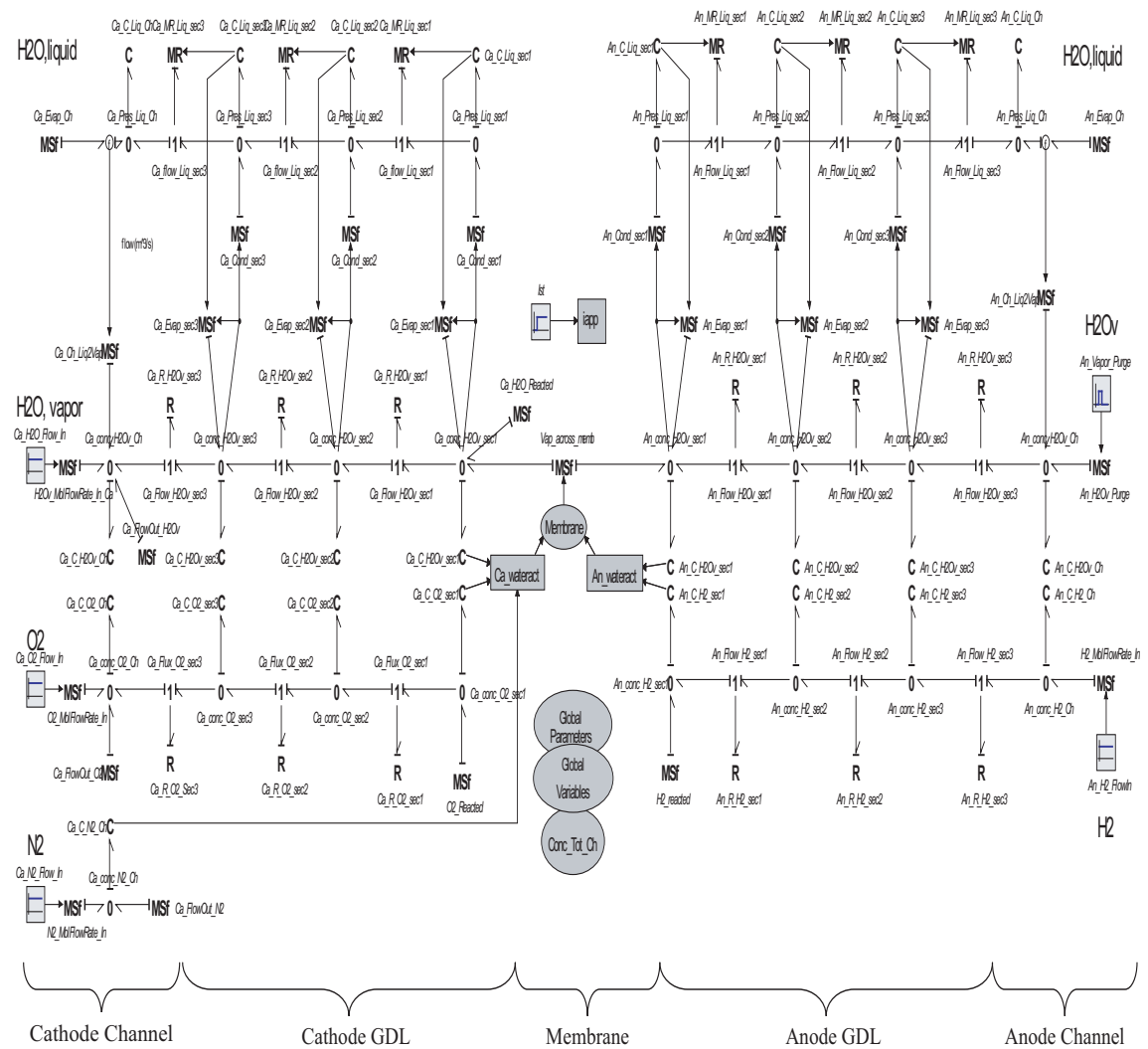
Figure 3.2: Complete Bond Graph Representation of a 3-Section Discrete Water Dynamics Model.

model simplification, the concentration of nitrogen throughout the cathode diffusion

layer is assumed to be identical to the concentration in the channel.

3.3 The Model Order Reduction Algorithm

Analysis via MORA proceeds with the above-derived bond graph version of the full-order numeric model.

3.3.1 Background of the MORA

The Model Order Reduction Algorithm (MORA) derived by Louca et al. [36] is applied and analyzed in this chapter. The MORA is a method that seeks to simplify complex models by creating a metric named *activity* to determine the energetic contribution of every element of a model. Based on the fact that $Power = \mathcal{P} = $ **effort** $\cdot$ **flow**, the *activity* is defined:

$$activity_j = \int_0^T |\mathcal{P}_j(t)|dt = \int_0^T |\mathbf{e}_j \cdot \mathbf{f}_j| \, dt, \quad (3.20)$$

where the **effort** and **flow** variables for this application, (derived in 3.1), are concentration (mol/m³) and molar flux rate (mol/m²/sec) for the gas constituents, and capillary pressure, p_{cap} (Pa) and volumetric flow rate (m³/sec) for the liquid states, respectively. Use of pressure and volumetric flow for the liquid constituents is typical, resulting in units of Watts for the power and Joules for the *activity*. However, for comparison between gas and liquid elements, it is necessary to scale the results of the power calculations for the gaseous elements since the molar flux needs to be converted to volumetric flow rate (m³/s) and the concentration to pressure (N/m²).

Once the *activity* of an element is determined, it is normalized by an *Activity Index(AI)* to determine whether the element has significant contribution to the overall energy of the system. The definition of the *Activity Index(AI)* is:

$$AI_j = \frac{Activity_j}{\sum_1^m (Activity_j)} \times 100\%, \quad (3.21)$$

where m is the total number of energetic (energy-utilizing) elements in the model.

As a function of the sum total of all the individual element *activites*, the *AI*

provides a means to compare elements from any part of the model.

An important aspect of the MORA is that it reduces model complexity while maintaining the physical meaning of the variables and parameters. It is also applicable to nonlinear systems, which, due to the nonlinear nature of this model, makes it attractive for use here.

3.3.2   Application of the MORA

Activity results are strongly dependent upon the duration of the simulation and the inputs to the system. For this analysis, an attempt was made to systematically determine the influence on the *activity* for appropriate durations and inputs. Inputs considered were a step changes in I_{st}, purge events, and a sum of sinusoids stack temperature. *Activity* calculations were performed for all the possible combinations of input mentioned above, and a range of durations that were tied to mode speeds of the system. Review of the results showed that using the longer time-constants of the system gave a disadvantage to the concentration states, that reach equilibrium quickly, as their net **flow** goes to zero early in the time window. At the opposite extreme, using the time constant of the fastest mode as the duration undervalues the slow modes.

As can be seen from (3.20), it is necessary to assign a time duration for the *activity* calculation. This is a critical aspect of the method, with influence on the results as great as variations in the system inputs. Excitation of all elements can be obtained by varying the main disturbance inputs of I_{st} and T_{st} at frequencies significantly higher than normally experienced during fuel cell operation. It was determined that the equitable input/duration combination would be to implement high-frequency stack current and temperature changes while taking energy measurements over an extended period of time. This allows the fast gas and vapor capacitance elements to be frequently excited, while giving the slow diffusion *activities* time to grow.

To address the full potential of each group of states, an *activity* calculation was made for flooded and non-flooded conditions, with results listed in Table 3.1. An example of an *activity* simulation using the resistive elements of the H_2 and the anode water vapor v_{an} is shown in Fig. 3.3. In this plot, the H_2 *activities* show only slight variation from section to section, while the water vapor *activities* show significant section to section variation.

In a typical *activity* analysis, it is common to compare *activity* magnitudes,

Table 3.1: Activity Summary for Borderline and Flooding Cases : Threshold = 0.01

pink	Small sec-to-sec variation		orange	Large sec-to-sec variation		blue	Negligible *activity*	

Borderline					**Flooding**				
sec	Element	AI%	Element	AI%	Sec	Element	AI%	Element	AI%
1	H_2 storage	0.002	H_2 flow	2.380	1	H_2 storage	0.002	H_2 flow	2.410
2	Capacitance	0.002	Resistance	2.320	2	Capacitance	0.002	H_2 Resistance	2.350
3		0.002		2.230	3		0.002		2.270
1	v_{an} storage	0.001	v_{an} flow	0.100	1	v_{an} storage	0.001	v_{an} flow	0.087
2	Capacitance	0.001	Resistance	0.030	2	Capacitance	0.001	Resistance	0.003
3		0.001		0.570	3		0.001		0.000
1	O_2 storage	0.001	O_2 flow	35.30	1	O_2 storage	0.001	O_2 flow	35.40
2	Capacitance	0.001	Resistance	25.80	2	Capacitance	0.001	Resistance	25.90
3		0.001		20.10	3		0.001		20.10
1	v_{ca} storage	0.001	v_{ca} flow	0.728	1	v_{ca} storage	0.001	v_{ca} flow	0.734
2	Capacitance	0.001	Resistance	0.023	2	Capacitance	0.001	Resistance	0.023
3		0.001		0.001	3		0.001		0.001
GDL	N_2 storage	0.000	N_2 flow	0.077	GDL	N_2 storage	0.000	N_2 flow	0.077
	Capacitance		Resistance			Capacitance		Resistance	
1	s_{an} storage	0.015	s_{an} flow	0.126	1	s_{an} storage	0.087	s_{an} flow	0.110
2	Capacitance	0.014	Resistance	0.259	2	Capacitance	0.003	Resistance	0.236
3		0.013		0.347	3		0.000		0.673
1	s_{ca} storage	0.013	s_{ca} flow	0.418	1	s_{ca} storage	0.013	s_{ca} flow	0.420
2	Capacitance	0.010	Resistance	0.898	2	Capacitance	0.010	Resistance	0.904
3		0.005		2.600	3		0.005		2.620
1	$S_{f,an}^{evap}$	0.479	$S_{f,an}^{cond}$	0.137	1	$S_{f,an}^{evap}$	0.488	$S_{f,an}^{cond}$	0.145
2	Flow Source	0.007	Flow Source	0.013	2	Flow Source	0.016	Flow Source	0.023
3		0.093		0.024	3		0.000		0.003
1	$S_{f,ca}^{evap}$	4.180	$S_{f,ca}^{cond}$	0.544	1	$S_{f,ca}^{evap}$	4.210	$S_{f,ca}^{cond}$	0.547
2	Flow Source	0.129	Flow Source	0.085	2	Flow Source	0.130	Flow Source	0.085
3		0.004		0.011	3		0.004		0.011
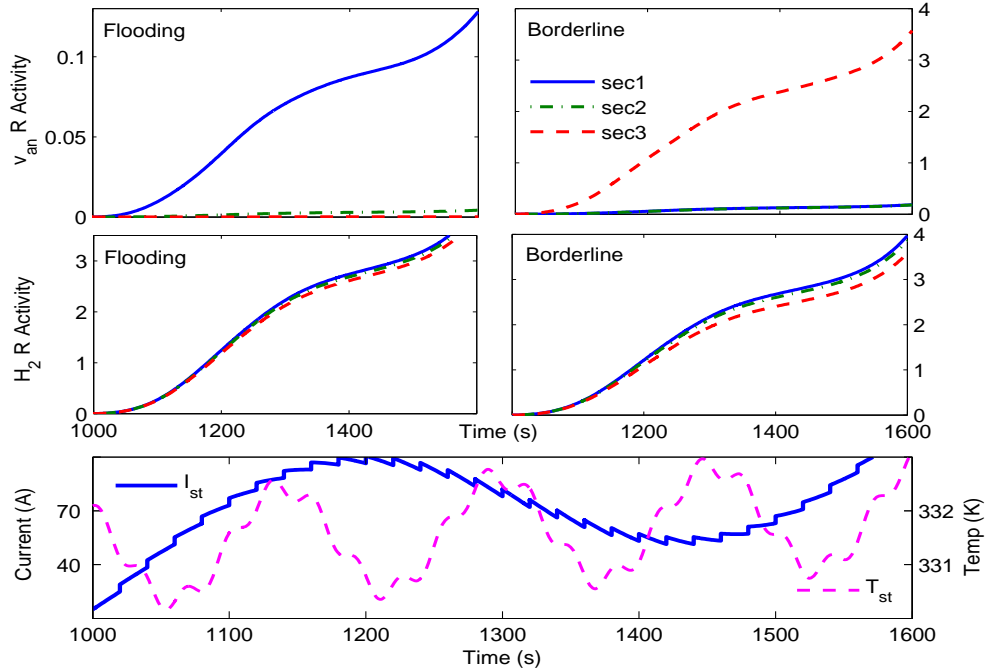
Figure 3.3: Activity of resistive elements have information regarding degree of linearity of distribution from state in discretized PDEs.

and conclude that either an element is negligible and can be eliminated, or that it's dynamics are fast enough to justify assignment of instantaneous equilibrium. The threshold for such considerations is a judgment call, with $< 0.1\%$ being common. However, the *AI* for this application will be dominated by the O_2 resistive elements, suggesting a more conservative threshold of 0.01% because a reduction in one order of magnitude will bring those O_2 resistive elements in line with other contributors to the *AI*.

As can be seen from the data in Table 3.1, the small *activities* of the capacitance elements for vapors and reactants imply that their dynamics are relatively inconsequential to the system. This suggests that it is appropriate to take the steady-state solutions for the gas and vapor states. From the bond graph point of view, removal of a capacitance element will leave a zero junction without it's capacitive element as shown in Fig. 3.4. The figure also includes the removal of the active modification signal for the gas flow resistance, which will be justified in Sec. 4.1.1.

A zero junction, representing a sum of flows, is the equation of mass balance
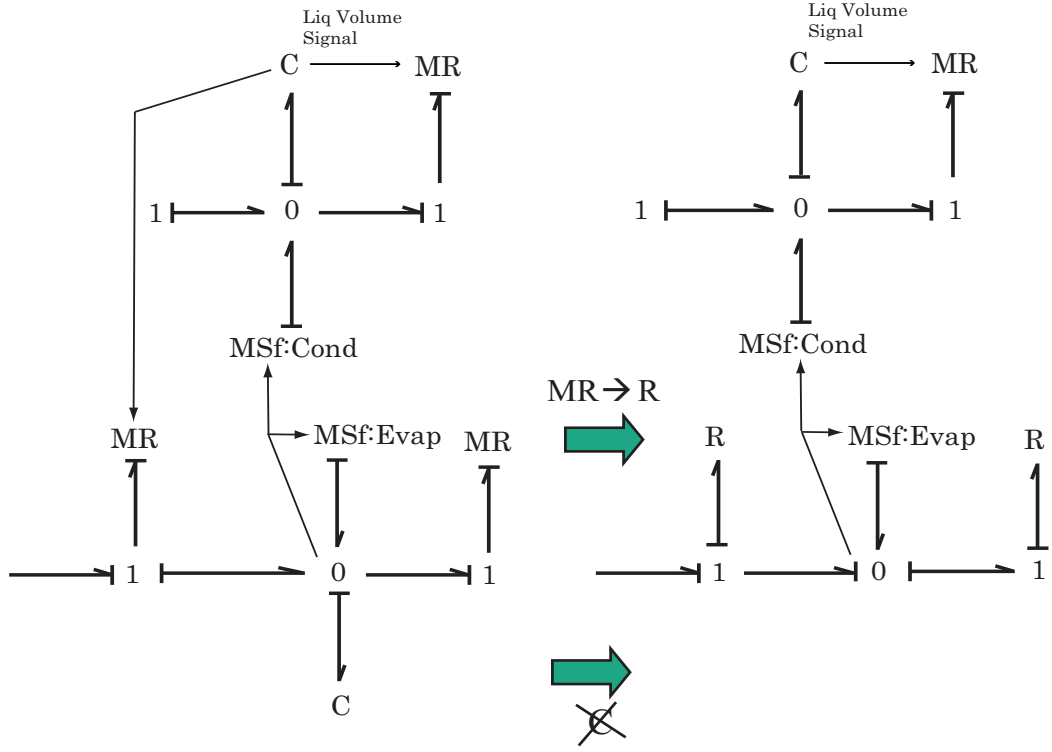
Figure 3.4: Small *activity* leads to residualization of the state associated with the capacitive element.

in the discretized k^{th} section for the jth element,

$$\frac{dc_j[k]}{dt} = \frac{1}{C}\left(\text{flow}^{in} - \text{flow}^{out}\right).\tag{3.22}$$

Thus, elimination of the capacitive element is identical to setting flow-in equal to flow-out, resulting in an equation that provides the steady-state solution.

Beyond the traditional element elimination, the *activity* analysis holds important information regarding degree of nonlinearity in a discretized PDE application, and thus aids in a judgment regarding sufficient spatial resolution. From this view, comparing the *activity* levels, it can be seen that the elements of some species have small variation in *activity* from section to section. It is hypothesized that small variation in *diffusion activity* implies *over-discretization*.

To evaluate the hypothesis, study of the definition of *activity* for a diffusion element shows that similar diffusion *activity* implies associated state reduction potential. As described in Sec. 3.1.2, the diffusion of a gas species through the liquid water-filled GDL pores can be modeled as *resistance* elements, and therefore have the power ($\mathcal{P}$) through them determined by the concentration *across* multiplied by

the **flow** *through*, or $\mathcal{P} = (c_j[k] - c_j[k+1])N_j[k]$.

For the non-vapor gases O_2 and H_2, once equilibrium in the section is reached, the flow into a section equals the flow out. Since the concentrations reach equilibrium very fast, the flow through each section is nearly equivalent. It is only variations in concentration that separate the diffusion *activties*. Therefore, similar *activity* results in diffusion elements imply a *linear distribution of concentration* in the GDL, which indicates a single section is sufficient to describe the distribution (i.e. lumped volume approximation).

The conclusion of the *activity* analysis is a reduction proposal with two options. The first is state residualization due to the sufficiency of steady-state solutions implied by low *activity*. These states are listed in the left side of Table 3.2. The second option is to keep the dynamics of the states, yet reduce the discretization because the small variation in section to section *activity* is small. The states with potential for reduced spatial discretization are shown on the right column of Table 3.2.

Table 3.2: Options for element reduction based upon *activity* analysis

Use Steady-State Solution	Lumped Volume
c_{O_2}	c_{O_2}
c_{H_2}	c_{H_2}
c_{N_2}	s_{ca}
$c_{v,an}$	s_{an}
$c_{v,ca}$	

Due to a lack of defensible metric, it is unclear if the degree of section to section variation for the liquid water flows can be judged similar or not. However, the results can be interpreted to indicate that the distribution of the liquid water in the GDL is more nonlinear than the distributions of the H_2 and O_2, and less nonlinear than than the water vapor distributions (using the slope of a least squares best fit to the data as the metric). Results from Chap. 4 will confirm this interpretation.

3.4   Time-Scale Decomposition

The *activity* study of Sec. 3.3.2 suggests that the water vapor and reactant states have very fast dynamics. In this section, a modal analysis is applied to verify the MORA result and attempt to quantify the time scale separation between liquid and gas states.

Insight into the relative response speeds of the system states is gained by linear time-scale decomposition techniques. Linearization of the numeric 24-state system of Sec. 2.3 was performed for operating points differentiated by λ_{H_2} to cause the system to experience both flooding and drying conditions. The other parameters of the system were kept at values typical of mid-level operation for the fuel cell stack; T_{st}=60°C, i=45 A/cm^2, RH$_{an}^{in}$ and RH$_{ca}^{in}$ equal to nearly dry H_2 (0.1%) and fully humidified air, respectively, and O_2 excess ratio at 300%.

This operating point represents the midrange of the normal operation of the experimental fuel cell on which the model was tuned and consequently validated ($0 \leq i \leq 0.45$ A/cm^2, $150\% \leq \lambda_{O_2} \leq 300\%$, $40^oC \leq T_{st} \leq 70^oC$) [3].

The linearization was performed numerically using the linearization function within Dymola^{TM} on the full-order model. The linear system was then exported to Matlab^{TM,1} for analysis using the Controls System Toolbox^{TM,1}.

The analysis begins by letting $\mathbf{v}$ be the eigenevectors of the discretized and linearized system matrix A (24×24). It is assumed that there is a similarity transformation $A_T = TAT^{-1}$ that will partition the system by modes into subsystems that can be analyzed separately. This transformation was accomplished by applying the balancing algorithm of [56], where each row-column pair of a matrix is scaled via similarity transformation T to have equal norms. The standard form of a similarity-transformed ($x_T = Tx$) system is:

$$\begin{aligned}
\dot{\mathbf{x}}_T &= TAT^{-1}\mathbf{x}_T + TB\mathbf{u} \\
\mathbf{y} &= CT^{-1}\mathbf{x}_T + D\mathbf{u}
\end{aligned}$$

(3.23)

The new system matrices can be fit into an overall matrix for purposes of performing scaling on one entity (D is omitted because the transformation does not affect it):

$$M = \begin{bmatrix} TAT^{-1} & TB \\ CT^{-1} & 0 \end{bmatrix}$$

(3.24)

The net result of the balancing transformation is that the off-diagonal elements are scaled-to-minimize according to their row and column position, moving the representation close to block diagonal. Thus, the resulting eigenvectors are grouped by blocks, which in the physical system tend to be elements with strong mutual interaction (such as a discretized PDE or states sharing a volume). For this two-phase application, this results in a pair of subsystems with one consisting only of gas states,

---

[1]Trademark of the MathWorks

and the other only of liquid states. Because T is diagonal, the diagonal elements of the A matrix are unchanged, and the physical meanings of the states are preserved.

After applying the transformation, the new system of eigenvectors are practically decoupled with $\mathbf{v}_T = T\mathbf{v}$, and $V_T = [\mathbf{v}_{T,1}|\mathbf{v}_{T,2}|...|\mathbf{v}_{T,n}]$ defining the eigenspace of the transformed system. Normalizing those eigenvectors, and eliminating components below a negligible threshold, it is found that the eigenspace has the form:

$$V_T \approx \begin{bmatrix} 0 & V_{T,l,6\times6} \\ V_{T,g,18\times18} & 0 \end{bmatrix}, \tag{3.25}$$

where the subscripts g and l indicate gas or liquid states. This shows that, though not a perfect mathematical decoupling, with reasonable thresholds a transformation can be found that results in a practical decoupling of the liquid and gas states. Note that the resulting eigenvectors cannot be associated with individual states of the original system, only that each eigenvector can be assigned to a linear combination of either only gas states or only liquid states.

We measure the gas/liquid coupling by the infinity norm of the components that correspond to liquid states in the unit normalized, predominantly gas state eigenvectors, and likewise of the gas states in the predominantly liquid state eigenvectors. Repetition of the process for low and high end operating points of the typical range, as well as for flooding and drying conditions, showed that the strength of the gas/liquid coupling grows with the current density (i) and is greater during drying conditions. At a typical current density, the coupling is $\sim4\%$, and is still only a minor influence at maximum load. (Table 3.3).

Table 3.3: Gas and liquid state coupling versus current density i.

i (A/cm)^2	0.10	0.25	0.45	1.0
Coupling	0.05%	0.3%	3.9%	11.3%

As the anode inlet flow increases due to the high current density, the channel states emerge as components of the anode liquid modes, indicating a channel gas-GDL liquid coupling on the anode side. Further, the coupling is entirely one-way, i.e. certain gas constituents show up in the predominantly liquid modes, but liquid states are nearly absent from the predominantly gas modes.

Modal analysis provides an understanding of the time constants associated with the system. For this model, the time constants all relate to combinations of filling dynamics for gases and/or liquid water. Using a flooding condition as an example,

the time constants for the GDL states within the full-order system are listed in Table 3.4.

Table 3.4: GDL State Response Speeds (Time Constants (τ_c))

Reactants		Water Vapor		Liquid Water	
Mode	τ_c [s]	Mode	τ_c [s]	Mode	τ_c [s]
c_{H_2}	$3.0\text{x}10^{-4}$	$c_{v,an}$	$7.5\text{x}10^{-4}$	s_{an}	2.91
c_{H_2}	$5.3\text{x}10^{-4}$	$c_{v,an}$	$8.5\text{x}10^{-4}$	s_{an}	5.61
c_{H_2}	$4.0\text{x}10^{-3}$	$c_{v,an}$	$1.0\text{x}10^{-3}$	s_{an}	25.6
c_{O_2}	$1.2\text{x}10^{-3}$	$c_{v,ca}$	$4.8\text{x}10^{-4}$	s_{ca}	1.30
c_{O_2}	$2.2\text{x}10^{-3}$	$c_{v,ca}$	$5.5\text{x}10^{-4}$	s_{ca}	2.48
c_{O_2}	$1.2\text{x}10^{-2}$	$c_{v,ca}$	$0.9\text{x}10^{-3}$	s_{ca}	12.5

The most significant information to be gathered from this table of 18 discretized PDE states within the GDL is the separating line that can be drawn between fast and slow modes of this system. An analysis of the eigenvectors for the 24 modes reveals that the slowest six modes are related to the filling dynamics of the six states associated with liquid water in the GDL.

The slow mode time constants (liquid) range from 1.3 to 26 seconds, while the fast modes (gas) have time constants ranging from 0.3 ms to 12 ms. These results for the liquid are on the same order as the qualitative conclusions reached by Natarajan et al [9].

This large time-scale separation indicates that application of a singular perturbation analysis is appropriate, i.e. (i) treat the liquid states as time-invariant (slowly-varying) parameters when we seek the analytic solutions for the gaseous states, and (ii) treat the gaseous states as having reached their steady-state values during the calculation of the liquid states.

The main conclusion taken to the analytic solution stage is that the MORA analysis (Sec. 3.3) indicates that the gas/water vapor-related capacitance elements of the model (which represent the dynamic characteristics of the gas/vapor states) can be neglected due to their low *activity*. This implies that steady-state solutions can be used for the GDL hydrogen, oxygen, and water vapor concentration states when solving for the slow GDL liquid states. This result is confirmed with a modal analysis on the linearized system, which shows additionally that there is a significant separation between the GDL liquid and gaseous state time constants.

Chapter 4

The Semi-Analytic Solution

In this chapter, significant model simplification is obtained by derivation and implementation of analytic solutions for those states associated with the low-energy modes found through the *Activity* analysis of Sec. 3.3. A time scale decomposition verified the selection of the GDL gas constituent states for residualization to algebraic equations due to large time scale separation. This fact justifies use of the quasi steady-state solutions for H_2, O_2, and water vapor when solving for the slowly varying liquid water distributions. The SAS model must accommodate a mobile boundary front between single and two-phase water conditions in the GDL, and x_{fr} is defined as the location nearest the membrane such that $s(x_{e,fr}, t) = 0$. Inclusion of the moving front necessitates the addition of a set of equations to establish the analytic solution for the range where only water vapor is present (i.e. $x_{fr} < x \leq L$). The behavior throughout the GDL will then be described with a combined analytic solution that allows switching between the range $\{s(x, t) > 0$ for $x \in [0, x_{e,fr}]\}$ and $\{s(x, t) = 0$ for $x \in [x_{e,fr}, \pm L]\}$.

4.1   Development of the Semi-Analytic Model

In this section the derivation of a semi-analytic model capable of predicting fuel cell voltage output response to changes in input is presented. The voltage estimation capability of this model is equivalent to that of the discretized numeric model presented in [3], with the notable improvements being:

- Reduced computational effort due to implementation of steady-state analytic solutions for gaseous constituents,

- Improved understanding of constituent distributions due to finer model resolution,
- Improved understanding of the physics of liquid flow conditions at the capillary flow boundary and two-phase water interaction.

4.1.1 Sensitivity of Diffusivity to Liquid States

There are two phenomena responsible for the coupling between the liquid and the gas states. The first is the direct coupling between water vapor concentration and water fraction due to evaporation/condensation, which is clear from (2.12), and is addressed in Sec. 4.1.3. Second, the amount of liquid water present has an influence on the gas fluxes via the diffusivity's dependence on $s(x, t)$ (2.1), the liquid water states.

The diffusivity coupling must be addressed in order to reach an analytic solution for the gas constituents. An assumption of negligible liquid water influence on diffusivity (i.e. $s = 0$) can alter estimation significantly as shown in Fig. 4.1. Further, an inappropriate choice of constant liquid water fraction s can have a significantly detrimental affect on the model predictions of $(c_{v,an} - c_v^{sat})|_{x=0}$, which is an important value for calculation of membrane water transport. The plot shows that if the average liquid water fraction (s_{avg}) was known and used to calculate diffusivity, $D_v^{s_{avg}} = D_v \left(\frac{1}{L} \int_0^L s dx \right)$, the error would be at a minimum. Unfortunately, s_{avg} is not known a priori, so a logical choice that can be made a priori is $s = s_{im}$, thus $D_v^{s_{im}} \cong D_v(s)$ is used as an approximation for the effective diffusivity. The error caused by this approximation is considered negligible since $s(x, t)$ is generally in the vicinity of s_{im}. A relevant exception to this is during GDL drying $(s = 0)$, which will be addressed by switching the water vapor concentration model to one without evaporation, and using the effective diffusivity for zero water saturation $(D_{v,\varepsilon}(0))$.

The case where a section of the GDL is drying requires a more comprehensive analysis of the system equations since it involves a dynamically varying boundary, where the two-phase water flow transitions to only water vapor flow. The experimental data used here to validate the soon-to-be-presented semi-analytic model and the coarse numeric models do not correspond to conditions that cause the GDL section nearest the channel to reach $s = 0$. Were the discretization to have greater resolution (perhaps $n > 10$), then GDL section drying may have occurred during purges of the dead-ended system used in the experiments. However, the effect of this very short term drying on the voltage prediction is expected to be negligible.
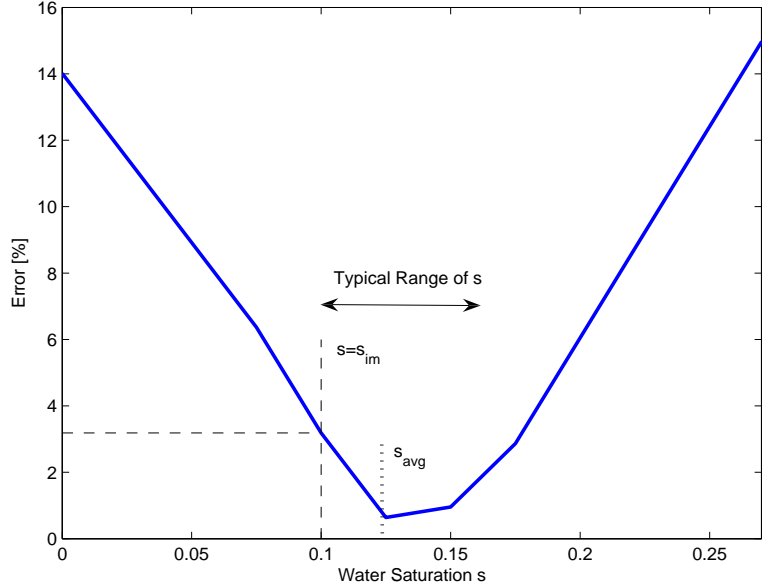
Figure 4.1: Steady-state error in $(c_{v,an} - c_v^{sat})|_{x=0}$ for varying choices of constant liquid water fraction.

Approximation of the temporally and spatially-varying $s(x,t)$ with $s(x,t) \approx s_{im}$ decouples the liquid and vapor PDEs. This enables an analytic solution for the gas species. To evaluate the effect of this assumption on the $c_{v,an}(x)$ distribution, the results of Sec. 3.4 suggest that the diffusivities can be treated as slowly varying parameters for the purpose of solving the gas PDEs because they are functions of only the slowly varying s. For error comparison purposes, the numerically determined $s(x[k],t)$ is used at each time step and in each discretized section to calculate the effective diffusivity. Assuming the liquid saturation as constant while the water vapor concentration PDE is solved leads to Fig. 4.2. It shows that the assumption of $s = s_{im}$ does not result in a significant change in the water vapor concentration distribution.

With the assumption of constant diffusivities, denoted $D_v^{s_{im}}$ and $D_j^{s_{im}}$ for the water vapor and reactant cases respectively, it is possible to solve the $c_j(x,t)$ and $c_{v,e}(x,t)$ second-order PDEs analytically using separation of variables.

4.1.2   Gas Constituent Solutions

It is assumed that the water phase mix will always be two-phase on the membrane side of the mobile front, and if the front is within the GDL, the entire range on the channel

46
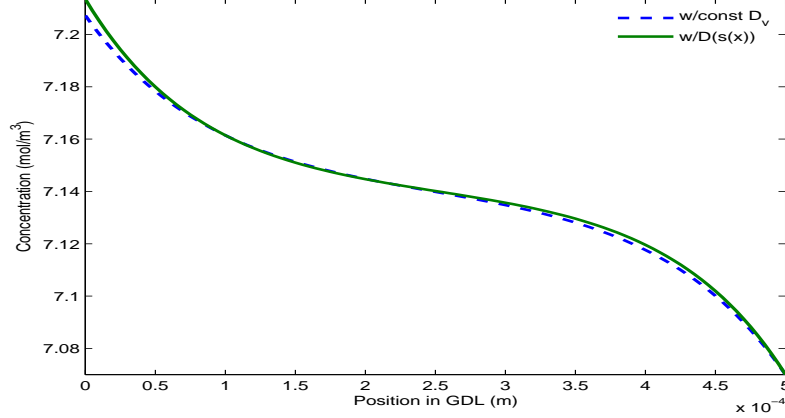
Figure 4.2: Use of $s = s_{im}$ has negligible effect on solution.

side of the front will be single-phase. An undesirable example where this would not be true is if the cathode side experienced sudden and significant drying such that the back diffusion not only ceased, but changed direction. That case will not be considered here. It should be noted that the assumption of consistent cathode liquid water presence implies that the cathode channel water vapor concentration is $c_v^{sat}(T_{st})$ for all t. Further, the transient solution of the gas constituent solutions is presented in order to identify any/which of the modes from the linearization correspond to the analytic solutions.

The separation of variables methodology is used to find the solution to the gas/vapor PDEs (shown in Appendix B). The explicit solution for the anode (similar for the cathode) gas constituents when liquid water is present throughout the GDL (i.e. under the assumption that $s(x,t) > 0$ for $x \in [0, L]$) is found to be:

$$c_{H_2}(x,t) = \sum_{n=0}^{\infty} e^{-D_{H_2}^{s_{im}} \eta_n t} A_n \cos(\sqrt{\eta_n} x) +$$
$$\frac{N_{H_2}^{rct}}{D_{H_2}^{s_{im}}}(L - x) + c_{H_2}^{ch}, \tag{4.1}$$

and,

$$c_{v,an}(x,t) = \sum_{n=0}^{\infty} e^{-\zeta_n t} B_n \cos(\sqrt{\eta_n} x) +$$
$$\left(\alpha_1 e^{\beta x} + \alpha_2 e^{-\beta x}\right) + c_v^{sat}, \tag{4.2}$$

47

where

$$\eta_n = (n + 1/2)^2 (\pi/L)^2,$$

and

$$\beta = \sqrt{\gamma/D_v^{sim}} \qquad \zeta_n = (D_v^{sim}\eta_n + \gamma). \tag{4.3}$$

A_n and B_n are coefficients of the infinite series approximations in (4.1) and (4.2) for the shape of the distribution of the respective concentrations at time $t = 0$. Upon a change in the system conditions (e.g. a step in I_{st}), the solution will begin a transition from the steady-state distribution at $t = 0$ (let this state be ss^-) to the steady-state solution dictated by the new inputs (identified as ss^+).

For the H_2 solution, the coefficients A_n are

$$A_n = \frac{2}{L}\left[\frac{N_{H_2}^{rct}|_{t=ss^-} - N_{H_2}^{rct}|_{t=ss^+}}{D_{H_2}^{sim}\eta_n} + \frac{(-1)^n(c_{H_2}^{ch}|_{t=ss^-} - c_{H_2}^{ch}|_{t=ss^+})}{\sqrt{\eta_n}}\right]. \tag{4.4}$$

Note: Substitution of $N_{O_2}^{rct}$ and $D_{O_2}^{sim}$ for similar terms in the H_2 solution represented by (4.1) and (4.4) will result in the analytic solution for O_2.

From (4.2) it can be seen that the water vapor transient response solution is a transition from one exponential form steady-state solution to the next, described by the product of a decaying exponential in time and an infinite Fourier series. The coefficients for the water vapor transient solution are,

$$B_n = \frac{2}{L(\beta^2 + \eta_n)}[\beta(\varphi_2 - \varphi_1) + \tag{4.5}$$
$$\sqrt{\eta_n}(-1)^n(\varphi_1 e^{\beta L} + \varphi_2 e^{-\beta L})],$$

where

$$\varphi_i = \alpha_i|_{t=ss^-} - \alpha_i|_{t=ss^+}. \tag{4.6}$$

Figure 4.3 shows the transitions from an initial distribution to the next steady-state distribution required due to a change in BC. The changes in slopes at the membrane are caused by a step current density input. The fast time constants derived in Sec. 3.4 are apparent. Note here that the solution for the vapor concentration is contingent upon the assumption that liquid water extends throughout the GDL length, so (4.2) holds for $0 \leq x \leq L$. Considering the time scale separation, only the steady-state solutions of the gas constituent PDEs are of interest hereafter. For H_2 and O_2, the only difference in the analytic solutions between single and two-phase
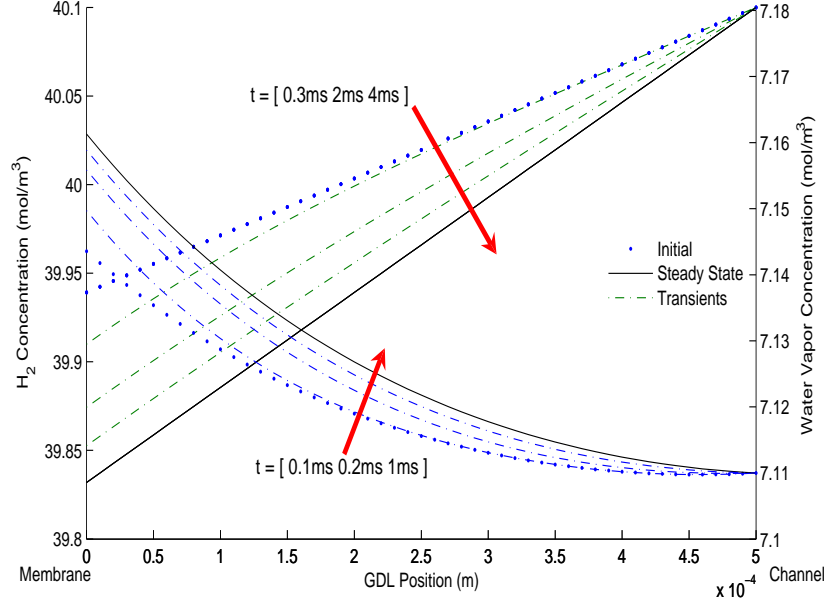
Figure 4.3: Transient solutions of c_{H_2} and $c_{v,an}$ for a step in current density ($0.15 \rightarrow 0.30$ A/cm^2).

regions is in the diffusivity coefficient.

The steady-state solutions for the reactants can be expanded to include the moving boundary at x_{fr}:

$$c_{H_2}(x) = \frac{D_{H_2}^{s_{im}} i(t)}{D_{H_2,\varepsilon} 2F}(x - L) + c_{H_2}^{ch} \qquad [x_{fr} \leq x \leq L], \qquad (4.7a)$$

$$c_{H_2}(x) = \frac{i(t)}{D_{H_2}^{s_{im}} 2F}(x - x_{fr}) + c_{H_2}(x_{fr}) \qquad [0 \leq x < x_{fr}], \qquad (4.7b)$$

$$c_{O_2}(x) = -\frac{i(t)}{D_{O_2}^{s_{im}} 4F}(x - L) + c_{O_2}^{ch} \qquad [-L \leq x \leq 0], \qquad (4.7c)$$

where $c_{H_2}(x_{fr})$ is determined from (4.7a), then applied in (4.7b).

Determination of the Vapor Solution Coefficients

The steady-state water vapor distributions when $s(x,t) > 0$ are given by:

$$c_{v,an}(x) = \alpha_1 e^{\beta x} + \alpha_2 e^{-\beta x} + c_v^{sat} \qquad [0 \leq x < x_{fr}], \qquad (4.8a)$$

49

$$c_{v,ca}(x) = \nu_1 e^{\beta x} + \nu_2 e^{-\beta x} + c_v^{sat} \qquad [-L \leq x \leq 0], \qquad (4.8b)$$

where,

$$\beta = \sqrt{\gamma/D_v^{sim}}. \qquad (4.9)$$

The α_i are functions of N^{mb} and the anode channel condition (i.e., the anode GDL BC),

$$
\begin{aligned}
\alpha_1 e^{\beta x_{fr}} + \alpha_2 e^{-\beta x_{fr}} &= c_v(x_{fr}) - c_v^{sat}, \\
\alpha_1 - \alpha_2 &= -N^{mb}/\beta D_v^{sim}.
\end{aligned}
\qquad (4.10)
$$

The ν_i, similar to the α_i, are dependent upon N^{mb} and the cathode channel condition, but are additionally influenced by the water vapor reaction term N_v^{rct} from the formation of H_2O at the cathode catalyst,

$$
\begin{aligned}
\nu_1 e^{-\beta L} + \nu_2 e^{\beta L} &= c_{v,ca}^{ch} - c_v^{sat} \\
\nu_1 - \nu_2 &= (N_v^{rct} - N^{mb})/\beta D_v^{sim}.
\end{aligned}
\qquad (4.11)
$$

The membrane water transport, N^{mb}, can be found from (2.16), and requires knowledge of the water vapor concentrations on both sides of the membrane, obtained from (4.8a) at $x = 0$,

$$
\begin{aligned}
c_{v,an}^{mb} &= (\alpha_1 + \alpha_2) + c_v^{sat}, \\
c_{v,ca}^{mb} &= (\nu_1 + \nu_2) + c_v^{sat}.
\end{aligned}
\qquad (4.12)
$$

The cathode side water vapor concentration is modeled to determine the $c_{v,ca}^{mb}$, which is necessary to find N^{mb}. However, the focus of our model is anode side water management (though the process developed is equally applicable to the cathode), thus for notation simplification the subscript an will be understood and omitted in subsequent formulation and discussion.

Since water vapor concentration on one side of the membrane influences the water vapor concentration on the opposite, a complex cathode channel inlet/outlet-membrane-anode channel inlet/outlet system of equations was derived and solved to determine the values of the four boundary conditions needed to simultaneously solve both the anode and cathode water vapor concentration second-order PDEs. These boundary conditions are influenced by inlet flow reactant excess ratios, temperatures, and relative humidities, as well as by the stack current, which is an exogenous signal defined by the power required. The details of this simultaneous channel-to-channel solution method are given in Appendix D.

The evaporation/condensation present in the two-phase regions acts as a dis-

tributed source. This source disappears in the single-phase water region. Implementation of the solution for values of x such that $s = 0$ for $x > x_{fr}$ (single-phase GDL conditions) requires determination of the front location (which is found numerically from the solution of $s(x,t)$ as expressed in Sec. 4.1.3) and a method of mating the solutions on either side of the front (discussed in Sec. 4.1.4). Within the single-phase water flow condition, the effective diffusivity is constant, so considering (2.8) when the evaporation reaction term has gone to zero,

$$\frac{\partial c_v}{\partial t} = \frac{\partial}{\partial x}\left(D_{v,\varepsilon}\frac{\partial c_v}{\partial x}\right) = D_{v,\varepsilon}\frac{\partial^2 c_v}{\partial x^2}, \tag{4.13}$$

where $D_{v,\varepsilon} = D_v(0)$ is the vapor effective diffusivity when $s = 0$.

The steady-state solution of

$$0 = D_{v,\varepsilon}\frac{\partial^2 c_v}{\partial x^2}, \tag{4.14}$$

is

$$c_v^{1p}(x) = m^{1p}(x - L) + c_v^{ch} \ (x \geq x_{fr}) , \tag{4.15}$$

where the slope mating the single-phase (1p) solution, m^{1p}, with the two-phase (2p) water region will be derived in Sec. 4.1.4.

4.1.3   Liquid Water Solution

Since it has been shown that the time constant of the water vapor is multiple orders of magnitude faster than that of the liquid water, it is acceptable to replace the c_v coupling term in (2.13) by its steady-state solution (4.8a). The PDE for liquid water distribution in the porous medium is then,

$$\frac{\partial s}{\partial t} = \frac{\partial}{\partial x}\left(b_1 S^{b_2}\frac{\partial s}{\partial x}\right) + \frac{M_v\gamma}{\rho_l}(\alpha_1 e^{\beta x} + \alpha_2 e^{-\beta x}), \tag{4.16}$$

for (x,t) such that $s(x,t) \geq s_{im}$, and

$$\frac{\partial s}{\partial t} = \frac{M_v\gamma}{\rho_l}(\alpha_1 e^{\beta x} + \alpha_2 e^{-\beta x}), \tag{4.17}$$

for (x,t) such that $0 < s(x,t) < s_{im}$ where $S = 0$ per (2.6), and β and α_i are as defined in the $c_{v,e}(x)$ solution previously (4.8a).

For the $s(x,t) \geq s_{im}$ case, (4.16) can be integrated twice (details in Appendix C)

to obtain the steady-state liquid water saturation,

$$s_{ss}(x) = \beta_z \left[\beta(\alpha_1 - \alpha_2)(x - L) + c_v^{ch} - c_v^{sat} \right.$$

$$\left. -(\alpha_1 e^{\beta x} + \alpha_2 e^{-\beta x}) + \left(\frac{S_\delta}{\beta_z} \right)^{b_2+1} \right]^{\frac{1}{b_2+1}} + s_{im}, \tag{4.18}$$

with

$$\beta_z = (1 - s_{im}) \left(\frac{M_v \gamma (b_2 + 1)}{\rho_l \beta^2 b_1} \right)^{\frac{1}{b_2+1}}. \tag{4.19}$$

For the $0 < s(x, t) < s_{im}$ case, because it is required for equilibria analysis, the unsteady solution of (4.17) can be found easily by integrating with respect to time,

$$s(x, t) = \frac{M_v}{\rho_l} \gamma (\alpha_1 e^{\beta x} + \alpha_2 e^{-\beta x}) t + s_0(x), \tag{4.20}$$

where $s_0(x)$ is the water saturation distribution at $t = t_0$. The $s_0(x)$ term represents the influence of the initial conditions on the water saturation.

Since the complete analytic solution of (4.16) has not been found, a Semi-Analytic Solution (SAS) is defined that combines the quasi steady-state analytic solutions for the gas constituents $(c_{H_2}(x), c_{O_2}(x), c_{v,an}(x), c_{v,ca}(x))$ with the anode liquid water ratio $(s(x, t))$ numeric differential algebraic equation (DAE).

4.1.4 Vapor Solution Transition

In this section the transition between the two-phase exponential solution (4.8a) and the linear single-phase solution (4.15) is analyzed. It is assumed that the water mass flow is preserved at the transition from two-phase to single-phase and use mass continuity across the transition point to establish the necessary flow rate on the single-phase side of the mobile front.

To satisfy mass flow continuity,

$$W_w^{1p} = M_v \varepsilon A_{fc} N_v^{1p} = M_v \varepsilon A_{fc} N_v^{2p} + W_l(x_{fr}^-, t) = W_w^{2p}, \tag{4.21}$$

where

$$N_v^{1p} = -D_{v,\varepsilon} \frac{dc_v^{1p}}{dx} = -D_{v,\varepsilon} m^{1p} \quad \text{for } x < x_{fr}, \tag{4.22}$$

and

$$N_v^{2p} = -D_v^{s_{im}} \frac{dc_v^{2p}}{dx} = -D_v^{s_{im}} \beta (\alpha_1 e^{\beta x} - \alpha_2 e^{-\beta x}) \quad \text{for } x \geq x_{fr}. \quad (4.23)$$

Rearranging to find the slope for the single-phase water concentration of (4.15),

$$m^{1p} = \frac{D_v^{s_{im}}}{D_{v,\varepsilon}} \beta \left(\alpha_1 e^{\beta x_{fr}} - \alpha_2 e^{-\beta x_{fr}} \right) - \frac{W_l(x_{fr}^-, t)}{M_v \varepsilon A_{fc} D_{v,\varepsilon}}. \quad (4.24)$$

Here x_{fr}^- indicates the spatial coordinate of the mobile front that is part of the two-phase water solution, where x_{fr} is defined as the smallest value of x such that $s(x_{fr}, t) = 0$ from the numeric solution of (4.16). The vapor-only water mass flow rate on the single-phase side of x_{fr} must match the sum of the liquid and vapor water mass flow rates on the two-phase side, hence the $W_l(x_{fr}^-, t)$ term in (4.24), which is found by solving (2.11) with $S(x_{fr}^-, t)$. Finally, the α_i are found from (4.10) and (4.12).

4.1.5   Simulation of Vapor Solution Transition

A simulation result of the reaction-diffusion to diffusion-only switching solution for a 10-section GDL discretization is shown in Fig. 4.4. The solution switches as the $s(x,t)=0$ boundary travels, section-to-section, from channel toward the membrane. The transition points are aligned to section boundaries due to application of the numeric solution. The graph shows the time progression of the water vapor concentration distribution as the liquid water mobile front recedes into the GDL, where sec. 1 is the lumped parameter volume closest to the membrane, and sec. 10 is closest to the channel. The system is modeled as an averaged single cell of the 24-cell, 300 cm^2 active area, 1.2kW experimental fuel cell stack set-up used in the model verification. The current density is 0.15A/cm^2, the cathode inlet stream is fully-humidified air, the anode inlet stream is pure, nearly dry hydrogen supplied at 2.63 times stoichiometry, and the stack temperature is set at 333K.

For this result, an initially flooded anode at t=0s experiences a change to a drying condition due to a 9% increase in H_2 excess ratio. By t =500s, the channel liquid water has been removed as evidenced by the drop in vapor concentration at $x = L$, but since there is still liquid water in sec. 10, the exponential solution is temporarily valid throughout the GDL ($0 \leq x \leq$ L). However, $s(10) < s_{im}$ indicates that liquid flow into the channel has ceased, implying that GDL-channel water transport
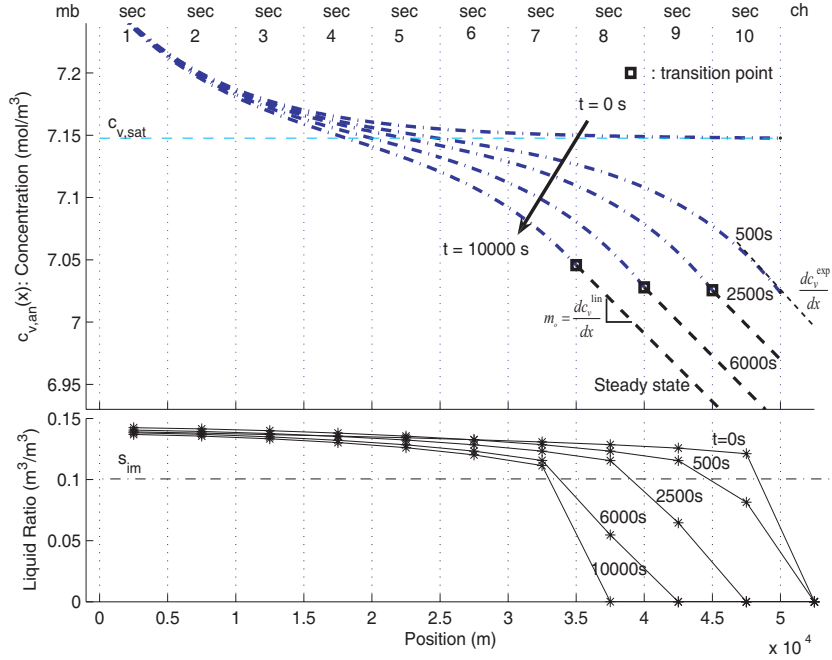
Figure 4.4: Water vapor distribution for the switching analytic solution with the mobile front in the transition from two-phase to single-phase during a step change in λ_{H_2}.

is in vapor phase only, with the mass flow rate given by,

$$W_w^{2p}(x_{fr}^-, t) = -M_v \varepsilon A_{fc} D_v^{s_{im}} \frac{\partial c_v^{2p}(x)}{\partial x}\bigg|_{x=x_{fr}^-} + W_l(x_{fr}^-, t), \qquad (4.25)$$

and $W_l(L, t) = 0$. This GDL to channel water flow rate is smaller than the vapor flow rate out of the channel because the two-phase front recedes toward the membrane during the time period $500s < t < 10000s$, finding equilibrium when the front reaches sec. 7. Thus, Fig. 4.4 depicts the modeled water vapor distribution of the combined diffusion-reaction/diffusion-only SAS, with the $c_v(x)$ in $x < x_{fr}$ taking the two-phase exponential solution, and the $c_v(x)$ in $x \geq x_{fr}$ taking the single-phase linear solution.

4.2 Verification of the Semi-Analytic Model

The model predicts voltage degradation by establishing a causal relationship between anode channel flooding and the fuel cell voltage deterioration.

The experiments were performed using a 1.2KW, 24-cell stack with an active area of 300 cm^2. The experiment operated with a dead-ended anode, and the nec-
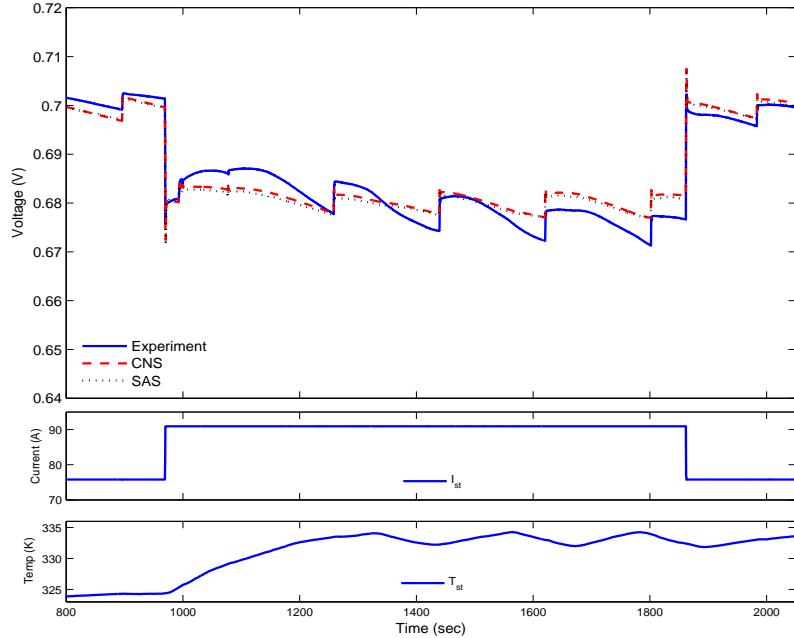
Figure 4.5: The semi-analytic model is able to capture static and transient trends in a direct comparison to experimental voltage output, and generates a voltage estimate very similar to the numeric solution

essary purges executed at 180 second intervals for a duration of 1 second. The SAS model used the same parameter values identified for the CNS model. For further experiment and parameter identification details, readers are requested to see [3].

In the first experiment, the stack current was varied from 75A → 90A → 75A while temperature was thermostatically controlled from 50C → 60C. Comparing the coarse numeric model to the semi-analytic model in Fig. 4.5 illustrates that little, if any, predictive accuracy has been lost by implementing the semi-analytic solution to the GDL dynamics, and the important trends related to transient manifold pressure dynamics and stack current changes are captured.

A desirable aspect of the model's control-oriented goal is estimation of the behavior of a 24-cell stack using a single cell model. In the set of validation experimental results shown in Fig. 4.6 a (200% → 300%) stoichiometry change is added to a series of stack current steps (40A → 60A → 15A). This data illustrates the range of voltage outputs from the individual cells in the stack. Though the model voltage prediction departs from the stack average value for some conditions, trends are still captured and the results are still within the range of individual cell values. The semi-analytic model output again tracks the coarse numeric model closely.
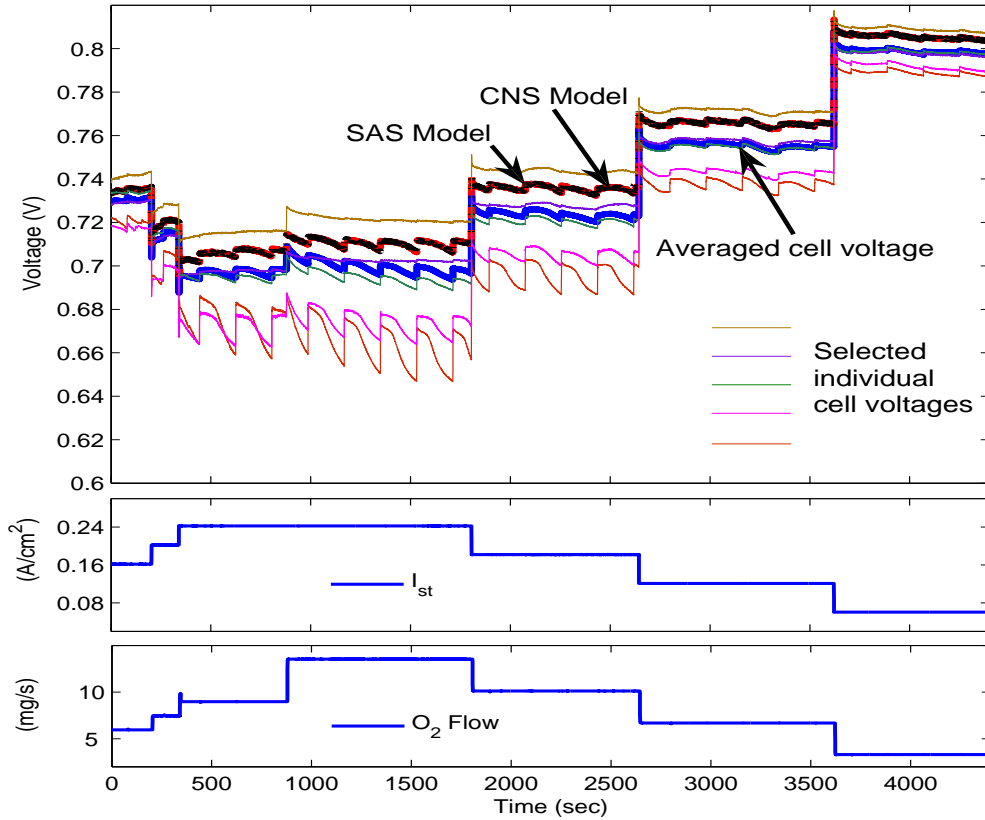
Figure 4.6: The voltage prediction captures fluctuations due to changing conditions, and bias is within the cell-to-cell variation.

4.3 Applications of the SAS Model

Three examples of applications of the SAS model to extend understanding of PEM fuel cell operation are briefly discussed in this section. The potential for future work related to addition of an along-the-channel dimension, inclusion of a temperature gradient in the channel, and studies of hydrogen utilization is shown by simulation of modified versions of the SAS model.

4.3.1 About the Along-the-Channel Dimension

It is commonly understood that the portion of the channel nearest the inlet will be significantly drier than the channel portion nearest the outlet. Anode channel flow determination is a balance between prevention of membrane drying at the inlet, while avoiding the flooding generated at the exit due to the accumulation of water from the

length of the channel. Numerous articles on the topic have been published, but the neutron imaging work is most dramatic. Fig. 4.7, borrowed from [4] indicates clearly the dry-inlet, wet-outlet phenomenon. If it were desirable for the outlet humidity to be less than c_v^{sat}, in the interest of membrane protection, it is necessary to consider the resulting membrane humidity near the channel inlet.
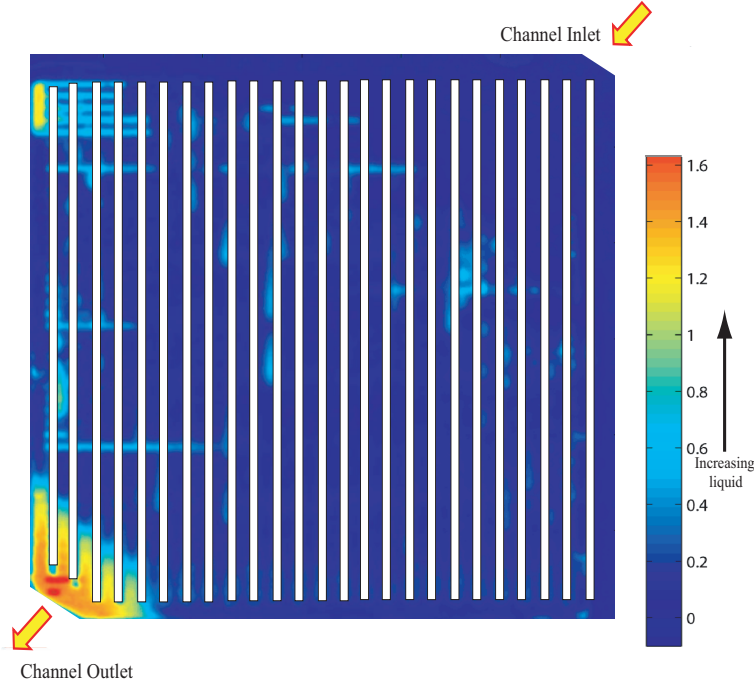
Figure 4.7: Neutron imaging shows liquid water accumulating near the anode channel exit (horizontal liquid images are from cathode side).

Modeling of along-the-channel concentration variation is implemented by considering the SAS model as a unit, and stacking it to stretch from inlet to outlet at the desired discretization degree. Fig. 4.8 demonstrates the concept. Using this methodology it is discovered that H_2 excess ratio must be increased significantly to make the water vapor concentration nearest the channel exit fall below c_v^{sat}. For a single lumped volume model under flow-control, flow-through conditions, a hydrogen excess ration of about 200% is required to keep the anode exhaust sub-saturated. As shown in Fig. 4.10, for a 9-section channel discretization, that excess ratio doubles to 400%, raising a concern for membrane drying near the inlet.

Such a large excess ratio appears to indicate that the SAS model will have a lower efficiency than the numeric model because of the high hydrogen pass-through. The issue of hydrogen utilization is addressed in Sec. 4.3.3, where it will be shown that a controlled flow-through model uses significantly less hydrogen than the purge-

cycle control method.

4.3.2 Model Extension to 1+1D

The benefit of reduced model complexity becomes apparent as the computationally inexpensive analytic solutions allow the modeler to increase GDL x-coordinate direction resolution and/or add discretization along the channel.

A graphical representation of the along the channel dimension is shown in Fig. 4.8. The spatial coordinate z is used to indicate position in the channel, with $z=0$ at the inlet, and $z = L_c$ as the outlet location.
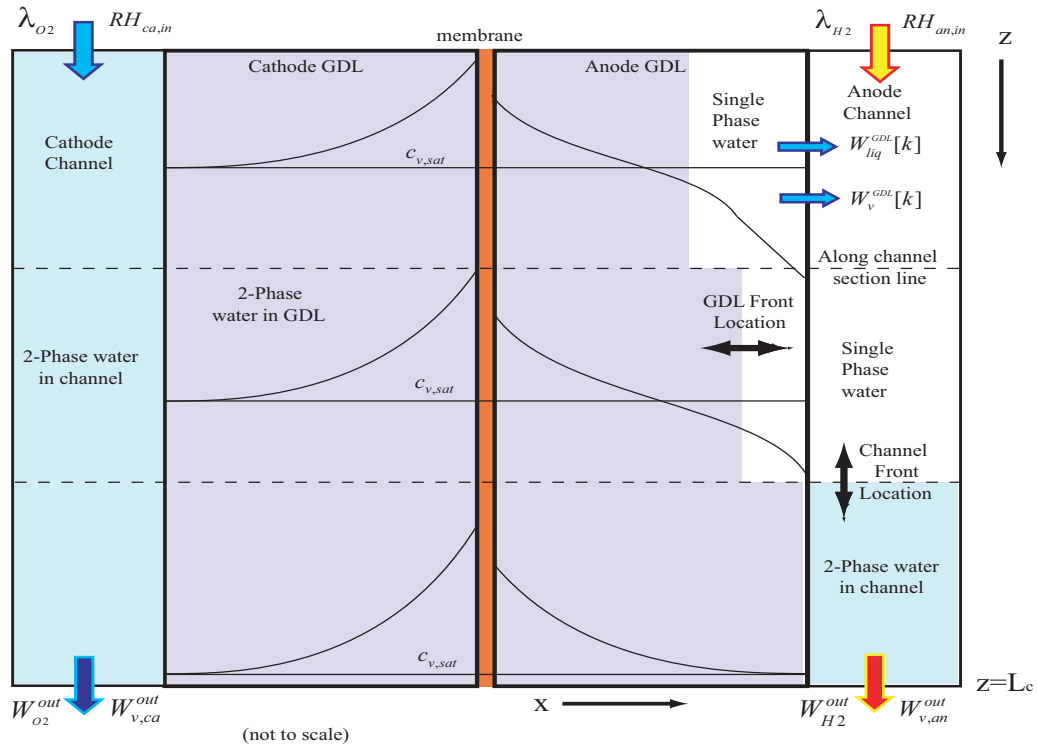
Figure 4.8: Schematic of along the channel model, with two-phase front for channel, and within the GDL for each unit model discretization along the channel.

For the single volume channel model, orifice equations were used (2.26,2.27) to relate pressure drops and flows through the inlet and outlet. Upon expansion of the channel model into a series of elementary volumes, the downstream boundaries for each discrete volume take the role and form of the exit orifice,

$$W^{ch}[m] = k^{ch}[m](P^{ch}[m] - P^{ch}[m+1]), \tag{4.26}$$

where m is the counter, $P^{ch}[m]$ are the pressures, and $k^{ch}[m]$ are the resistances to flow in each section along the channel. In general, the resistance changes as a function of channel location due to the variation in dynamic viscosity of the mixture due to varying molar fraction. However, when mass flow rate is used (4.26), k^{ch} is a function of kinematic viscosity (ν),

$$k^{ch} = \frac{\pi r_{eq}^4}{8\nu_{mix}dz},$$

(4.27)

where r_{eq} is the equivalent radius for the non-circular channel, and dz is the length of the discretized channel section. The normalization of dynamic viscosity by density to get kinematic viscosity reduces the influence of the elements of the mixture. Therefore, for the purposes of this illustrative example of the SAS unit model utility, it will be assumed that k^{ch} is constant over the length of the channel.

The use of a single lumped volume for the channel raises valid concerns regarding the ability of the model to address the inlet-outlet humidity disparity. To investigate this concern, a simulation discretizing the model into 9 sections was performed. Of interest are the humidities at the membrane nearest the inlet and at the channel exit. The conditions for the simulation are i=0.5A/cm^2, T_{st}=68C, ten sections of GDL discretization, and λ_{O_2}=300%. The λ_{H_2} is varied to show the effect on the two-phase water front in the channel, and is shown in the figures.

Using λ_{H_2}=250% results in accumulation of liquid water in the channel as shown in the bottom subplot of Fig. 4.9. The results shown are qualitatively similar to those published in [57]. Implementation of the control objective developed in 5.4 requires maintenance of the exit humidity below c_v^{sat}. Increasing λ_{H_2} to the neighborhood of 400% accomplishes this goal, with results shown in Fig. 4.10.

Raising the hydrogen flow rate has the obvious detrimental effect on fuel cell efficiency, reducing utilization from 40% to 25%. The positive news is that the anode side membrane humidity drops only 1% from 93% to 92%. Safe operating humidities for Nafion membranes are well below this range ([58]), suggesting that the control objective is unlikely to cause membrane drying. The reason that the membrane relative humidity decrease is less substantial than the channel is related to the membrane transport dependence upon concentration gradient. A decrease in water vapor concentration in the channel at the inlet draws more water vapor from the GDL and the drier anode GDL increases water transport from the cathode. This higher flow benefits the anode side humidity at the membrane first and foremost.

There are two significant hydrating effects that are not modeled that would raise
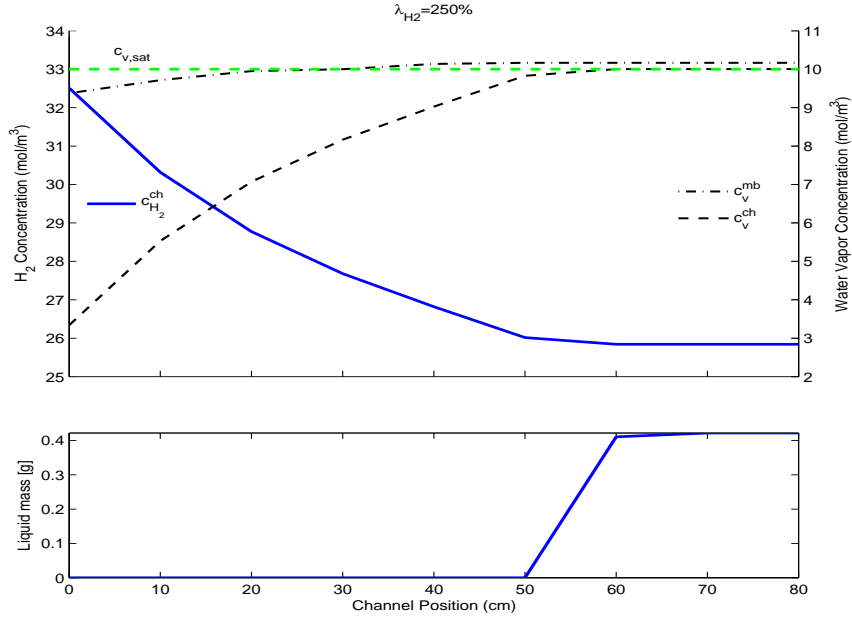
Figure 4.9: Distribution along-the-channel of water vapor at the membrane, as well as liquid, water vapor and hydrogen in the channel ($\lambda_{H_2} = 250\%$).

humidity at the membrane. The first is membrane-parallel diffusion vapor transport within the GDL. Though the convective flow dominates in the channel, diffusion in the GDL will move vapor along the membrane according to the gradient. The second phenomenon is the temperature gradient effect. The channel temperature will increase from inlet to outlet, gaining as much as 10°C at the exit in a co-flow study done on the cathode in [7], where the phenomenon was suggested as a method to prevent flooding at the channel outlet. Since the amount of water that can be held in vapor form increases exponentially with temperature, the forced implementation of a temperature gradient will lower exhaust humidity, while increasing inlet humidity versus an assumption of an averaged temperature for the length of the channel.

The SAS model can be easily modified to investigate the influence of the addition of a simple, estimated linear thermal variation along the channel (similar variation in the GDL). This is demonstrated in Fig. 4.11, assuming $T^{out} - T^{in} = 3°$C.

Figure 4.11 demonstrates the importance of inclusion of temperature gradients in the along-the-channel model. A set of conditions predicted by the model to incur channel flooding for the isothermal model is instead predicting non-flooding when temperature variation is included.
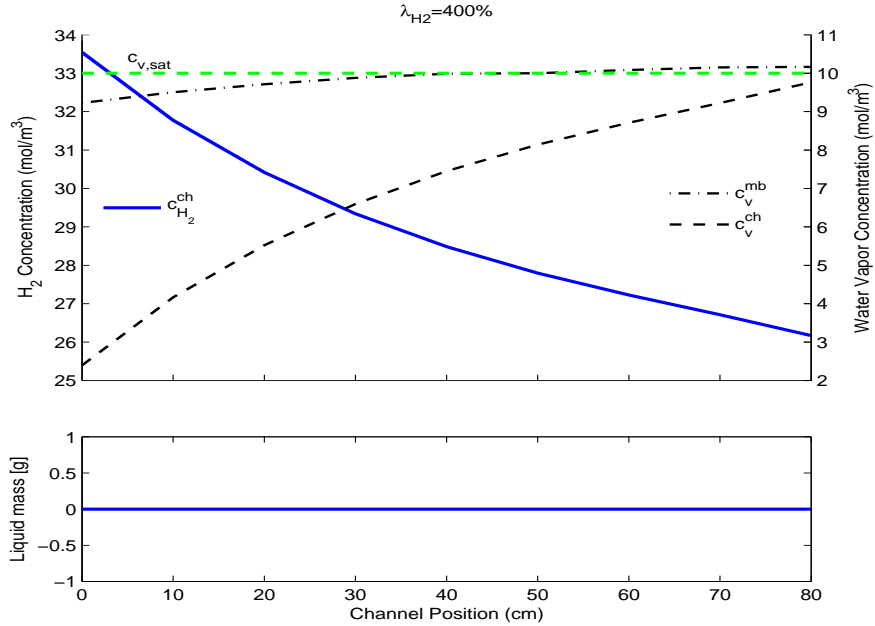
Figure 4.10: Distribution along-the-channel of water vapor at the membrane, as well as liquid, water vapor and hydrogen in the channel ($\lambda_{H_2} = 400\%$).

4.3.3 Maximizing Hydrogen Utilization by Control

Proportional control based on the channel outlet humidity error using the control objective of Sec. 5.4 is compared to dead-ended anode control methodology for hydrogen utilization. Fig. 4.12 indicates that the purge-controlled system tends to remove more water than is required in order to guarantee complete channel liquid removal.

The higher utilization for flow-through can be attributed to avoidance of the over-drying that occurs during purges. A purge causes drying to extend well into the GDL, removing more water than is necessary to re-establish flooding-induced cell voltage degradation. The cost of this GDL drying is more hydrogen pass-through with a smaller return on water removed due to ineffective water vapor transport in the sub-saturated channel. The control objective prevents channel liquid accumulation without over-drying the GDL.

The resulting consistency in voltage with the simple proportional-control applied to the outlet relative humidity is shown in Fig. 4.13.
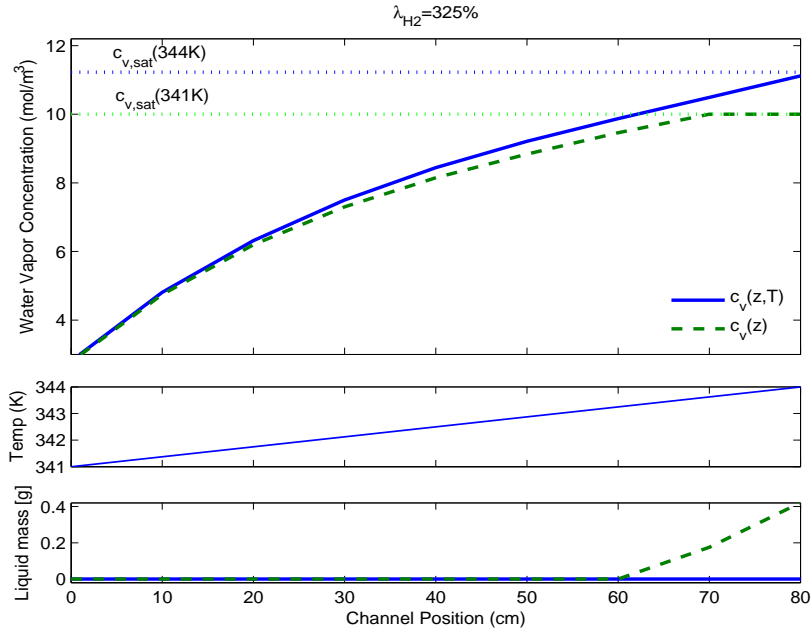
Figure 4.11: Addition of a temperature gradient turns model prediction from flooding to non-flooding for otherwise identical conditions.
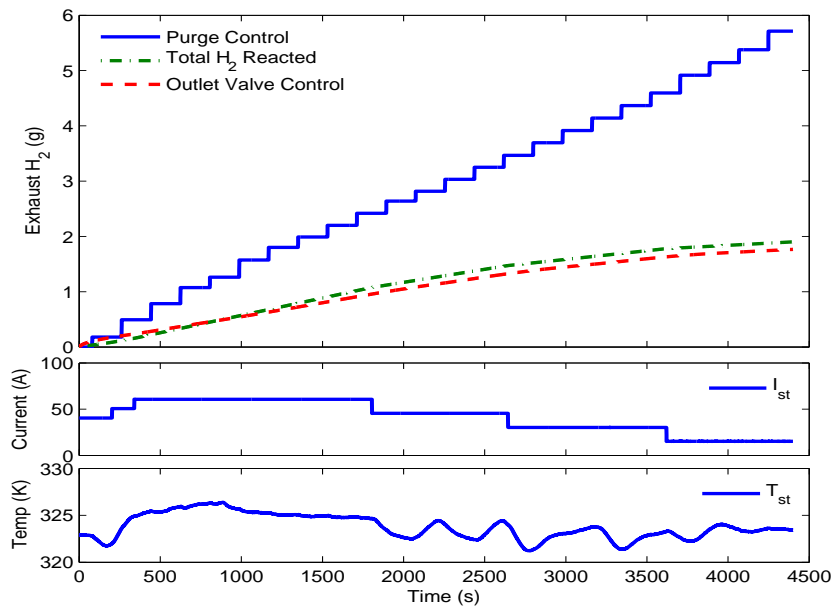
Figure 4.12: Hydrogen waste comparison between dead-ended and flow-through anode control.
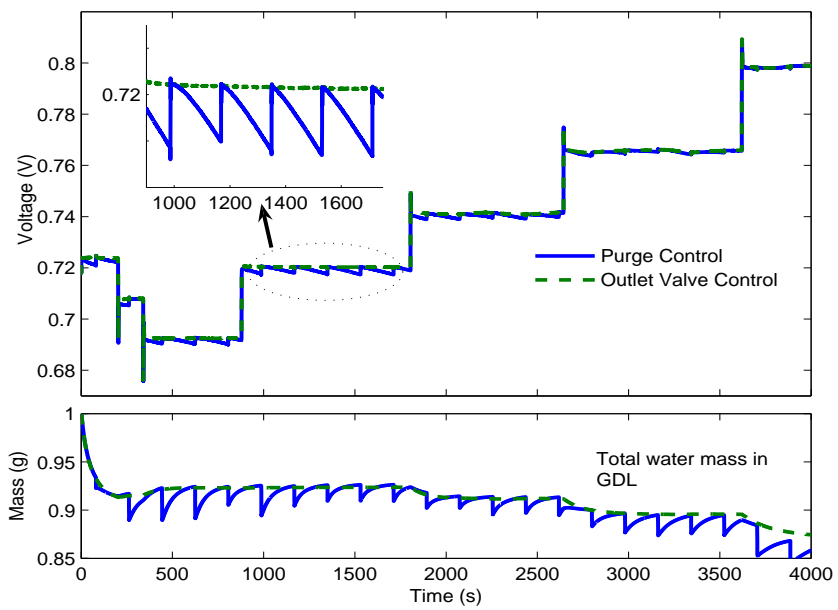
Figure 4.13: Simple P-control driven by exhaust humidity error versus reference prevents voltage degradation due to liquid accumulation.

Chapter 5

Control Analysis

This chapter describes the analyses performed to establish the control feasibility of the Semi-Analytic Solution (SAS) model. Since prevention of unbounded liquid water growth is the main concern, the stability study focuses on determining for which states, and under what conditions, instability exists. Upon isolation of the system instability, a hypothesis for a stabilizing control objective is proposed. The controllability-observability study will indicate if channel boundary value control of the GDL liquid water is feasible with the available physical inputs and will further provide information concerning measurement outputs.

5.1 Analysis of Equilibria

Understanding the system equilibria is a critical step towards definition of control objectives. The form of the time-derivative of (4.20) suggests that an equilibrium condition for $0 < s(x,t) < s_{im}$ does not exist because the α_i are not functions of s. This observation raises the need for discussion regarding s_{im}, and an analytic study of the dynamic properties of the model equilibria.

   The immobile saturation s_{im} represents the amount of liquid water required to wet the porous material fibers such that continuous liquid flow can proceed. A value of $s_{im} = 0.1$, or 10% of the pore volume being filled with liquid, is a common value used [5]. Others choose to ignore the s_{im} concept, which is equivalent to setting it to zero [59]. We proceed following the logic that there will be no liquid flow if the liquid volume is extremely low, and thus the s_{im} value of 0.1 will serve for analysis purposes. It is interesting to note that the choice of s_{im} will affect the liquid water

distribution estimation [54]. It is also shown here that the concept of immobile saturation introduces a range of s where equilibrium does not exist.

Analysis of the combined liquid and water vapor SAS and the steady-state liquid water solution (4.18) reveals that any distribution of c_v that satisfies the steady-state solution (4.8a) can be an equilibrium water vapor distribution. In this analysis, however, we are most interested in finding c_v equilibria that reduce or prevent build-up of liquid water in the channel.

Claim A: No equilibrium exists for $0 < s(x) < s_{im}$

There exists no equilibrium condition such that $s(x)$ within the GDL is non-zero, but less than the immobile saturation. To see this, expand the spatial derivative of the first term of (2.13) around some x,

$$\frac{\partial s(x,t)}{\partial t} = b_1 \left[b_2 S^{b_2-1}(x,t) \left(\frac{\partial S(x,t)}{\partial x} \right)^2 + S^{b_2}(x,t) \frac{\partial^2 S(x,t)}{\partial x^2} \right] - \frac{M_v \gamma}{\rho_l}(c_v^{sat} - c_v(x)). \quad (5.1)$$

Since $s(x,t) < s_{im}$ and $b_2 > 1$, the two terms within the bracket are zero because $S(x,t) = 0$ $(s(x,t) < s_{im})$, therefore

$$\frac{\partial s(x,t)}{\partial t} = -\frac{M_v \gamma}{\rho_l}(c_v^{sat} - c_v(x)). \quad (5.2)$$

First, considering the cases where $c_{v,ss}(x) \neq c_v^{sat}$, the RHS of the (5.2) dynamic equation is not a function of $s(x,t)$, and therefore no condition exists that will satisfy $\partial s/\partial t = 0$. Thus, while $0 < s(x,t) < s_{im}$, $s(x,t)$ will either grow (positive $\partial s/\partial t$, i.e. $c_v(x) > c_v^{sat}$) until it exceeds s_{im}, causing S to be re-introduced as an opposing factor for the condensation or decrease under evaporation (negative $\partial s/\partial t$, i.e. $c_v(x) < c_v^{sat}$), which will cease only when $s(x,t) = 0$.

It remains to show that $c_{v,ss}(x) \neq c_v^{sat}$ when $0 < s(x) < s_{im}$.

Claim B: $c_{v,ss}(x) \neq c_v^{sat}$ for $0 < s(x) < s_{im}$

Anywhere in the GDL that the liquid saturation steady-state is less than the immobile saturation, the water vapor pressure will not match the saturation pressure. To demonstrate this, a continuity of solution sketch of proof followed by a physical-insight based explanation is provided.

The sketch of proof method begins by assuming, in contradiction, that there

exists an $\bar{x}$ that satisfies $c_{v,ss}(\bar{x}) = c_v^{sat}$ and $0 < s(\bar{x}) < s_{im}$. When $s(\bar{x})$ falls between zero and s_{im}, it does so on a continuous open interval U around $\bar{x}$, where $s(x,t)$ is continuous because the derivative of (4.20) exists within $0 < s(x,t) < s_{im}$.

Continuity in $s(x,t)$ over U implies that an equilibrium value of $s(\bar{x})$ will be accompanied by continuous equilibrium values for all $s(x,t)$ within U. However, it follows from (4.8a) that,

$$c_{v,ss}(x) - c_v^{sat} = \alpha_1 e^{\beta x} + \alpha_2 e^{-\beta x} = 0 \;\Rightarrow\; e^{2\beta x} = -\frac{\alpha_1}{\alpha_2} \tag{5.3}$$

within U. Since α_1 and α_2 will have constant values in equilibrium, this incorrectly implies that the exponential function $e^{2\beta x}$ equals a constant over U. Therefore, the original premise is incorrect and there exists no $\bar{x}$ such that a steady-state condition $c_v(\bar{x}) = c_v^{sat}$ exists when $0 < s(x,t) < s_{im}$.

The above conclusion can be physically explained by recognizing that the claim is essentially a statement about the location of x_{fr} relative to x_{sat}, defined by $c_v(x_{sat}) = c_v^{sat}$.

Steady-state mass flow continuity implies that

$$W_{l,ss}(x) + W_{v,ss}(x) = W^{mb}. \tag{5.4}$$

Since both flows are positive in the direction from membrane to channel, the maximum equilibrium liquid flow naturally occurs when $W_{v,ss}(x)$ is at a minimum. Since the molar water vapor flux is directly proportional to the first spatial derivative of $c_v(x)$, this minimum is located at x_{sat}, which can be shown by taking the second derivative of (4.8a) with respect to x and setting it to zero,

$$\frac{\partial^2 c_v(x)}{\partial x^2} = \beta^2 \left(\alpha_1 e^{\beta x} + \alpha_1 e^{-\beta x}\right) = \beta^2 \left(c_v(x) - c_v^{sat}\right) = 0. \tag{5.5}$$

Since (5.5) is satisfied by $c_v(x) = c_v^{sat}$, the minimum water vapor transport occurs at $x = x^{sat}$, thus the steady-state liquid flow rate is a maximum at $x = x^{sat}$, implying $s(x^{sat}, t) > s_{im}$ and therefore $c_v(x) \neq c_v^{sat}$ for $0 < s(x,t) < s_{im}$.

Note 1: The steady-state liquid and vapor water transport at any x across the GDL can be calculated as follows:

Beginning with the definition of liquid water mass flow (2.9) and reversing the

chain rule to get the $\frac{\partial}{\partial x}$ to include the S^{b_2} term,

$$W_l = -\varepsilon A_{fc}\rho_l b_1 S^{b_2}\frac{\partial S}{\partial x} = -\varepsilon A_{fc}\rho_l \frac{b_1}{b_2+1}\frac{\partial}{\partial x}\left(S^{b_2+1}\right).$$ (5.6)

Substituting the steady-state $S_{ss}(x)$ found from (2.6) and (4.18),

$$W_{l,ss} = -\varepsilon A_{fc}\rho_l \frac{b_1}{b_2+1}\frac{\partial}{\partial x}\left(\frac{M_v\gamma(b_2+1)}{\rho_l\beta^2 b_1}\right.$$

$$\left[\beta(\alpha_1-\alpha_2)(x-L)+c_v^{ch}-c_v^{sat}\right.$$ (5.7)

$$\left.\left.-(\alpha_1 e^{\beta x}+\alpha_2 e^{-\beta x})+\left(\frac{S_\delta}{\beta_z}\right)^{b_2+1}\right]\right)$$

moving the constants out of the differentiation, rearranging, substituting for β^2 from (4.9), differentiating with respect to x,

$$W_{l,ss}(x) = -M_v\varepsilon A_{fc}\left[\underbrace{D_v^{sim}\beta(\alpha_1-\alpha_2)}_{-N^{mb}}-\underbrace{D_v^{sim}\beta\left(\alpha_1 e^{\beta x}-\alpha_2 e^{-\beta x}\right)}_{-N_v(x)}\right],$$ (5.8)

which is a restatement of (5.4), since $W_j(x) = M_j\varepsilon A_{fc}N_j(x)$.

Note 2: Equation (5.4) clearly indicates that the steady-state liquid flow will match the membrane water transport less the water vapor transport if there is sufficient liquid present in the GDL to generate capillary flow. Conversely, if capillary flow conditions are not met $(s(x,t) \leq s_{im})$, the entire water transport will be in vapor form. It is important to note that for a given set of system conditions, W^{mb} is constrained by W_l^{GDL} because as long as $s > s_{im}$, membrane water transport will not change. Although it might sound counter-intuitive, zero liquid flow across the GDL-channel interface allows greater membrane transport from cathode to anode. Thus the anode conditions can influence the cathode side water distributions.

5.2   Stability

It is known from experiment and simulation that the complete fuel cell will experience unbounded liquid water growth under many normal operating conditions (flow regulated anode inlet, high H_2 utilization, etc). Additionally, modal analysis of the system indicates the presence of unstable modes (poles at the origin of the linearized numeric system) when linearized about operating conditions with liquid accumula-

tion in the channels.

Figure 5.1 demonstrates the basic voltage degradation phenomenon, typical of our experimental results; namely that anode flooding is related to voltage degradation. The periodic purges necessary to remove the anode liquid water, and the recovery of the cell voltage, are clear in the vicinity of $t = 1800s$ and $t = 1980s$. A step-down change in stack current (91A $\rightarrow$ 76A) occurring at a time of low channel water mass ($t \sim 1862$s) does not noticeably affect the liquid accumulation, though the voltage output overshoot during the step-down is well estimated.
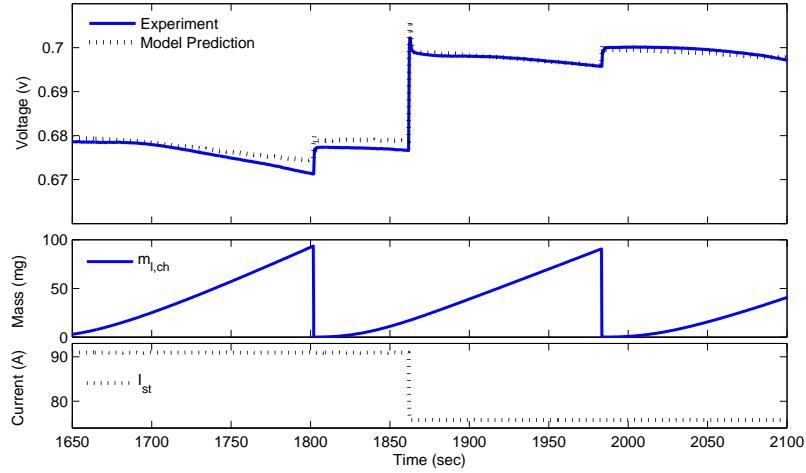
Figure 5.1: Experimental results support the hypothesis that anode flooding causes voltage degradation that is recovered through anode channel purging.

5.2.1 Stability of Liquid Water in the GDL

The apparent system instability is due to unbounded growth of the channel water mass state, which can only occur if liquid water flow from the GDL to the channel is non-zero and the channel water vapor is saturated ($W_l^{GDL} > 0$ and $c_v^{ch} = c_v^{sat}$). Specifically, one can show the following result:

Theorem: Given

- The assumptions of Sec. 2.1.1,
- The partial differential equations and boundary conditions described in Secs. 2.1, 2.2, and
- The semi-analytic solution from Sec. 4.1,

then the liquid water distribution for the anode is stable if the channel liquid water is stabilized.

Sketch of the Proof: If it can be shown that the GDL liquid water is stable (see below), then it can be concluded that stabilization of the channel water mass state results in overall water system stability, as this is the only remaining (possibly) liquid state.

To show stability of the liquid water distribution within the GDL for the boundary conditions described in Sec. 2.1.3, a general linearization of the liquid PDE with the assumption that $s > s_{im}$ for $0 \leq x \leq L$ is performed, which will result in $W_l^{GDL} > 0$. A transformation of the linearized system is then applied to facilitate the subsequent Lyapunov stability analysis.

The choice of $x_{fr} = L$ is made because it is the more general case, for which liquid flow into the channel is possible. By definition, liquid flow into the channel will cease when the mobile two-phase front recedes in the GDL. Stability of the liquid in the GDL can be proven using the following process for the simpler case where $x_{fr} < L$ if the same boundary condition ($S(x_{fr}) = S_\delta$) is employed.

Finally, stability is analyzed using the continuous PDE to address the question of potentially unstable spillover dynamics invisible to a numeric model.

5.2.2 Linearization of the Continuous PDE

In preparation for local stability analysis, a general linear PDE is derived for the liquid water anode distribution. If it is assumed that $s(x,t) > s_{im}$, (4.16) can be written,

$$\frac{\partial s(x,t)}{\partial t} = \frac{b_1}{(b_2 + 1)} \frac{\partial^2}{\partial x^2}\left(S(x,t)^{b_2+1} \right) + f(x), \tag{5.9}$$

where,

$$f(x) = \frac{M_v \gamma}{\rho_l}(\alpha_1 e^{\beta x} + \alpha_2 e^{-\beta x}). \tag{5.10}$$

Next, substituting the perturbation from an equilibrium distribution $S_0(x)$ of liquid water in the GDL,

$$S(x,t) = S_0(x) + \delta S(x,t),$$

so that,

$$\frac{\partial s}{\partial t} = \frac{b_1}{(b_2 + 1)} \frac{\partial^2}{\partial x^2} \left((S_0(x) + \delta S)^{b_2+1} \right) + f(x). \tag{5.11}$$

A linear approximation for polynomial expansion is,

$$(S_0(x) + \delta S)^{b_2+1} \simeq$$

$$\tag{5.12}$$

$$S_0(x)^{b_2+1} + (b_2 + 1)S_0(x)^{b_2}\delta S + H.O.T.(\delta S).$$

The distributed condensation-evaporation reaction term is represented as,

$$f(x) = f_0(x) + \delta f(x),$$

where $f_0(x)$ is the nominal term corresponding to $S_0(x)$. Inserting (5.12) and (5.13) into (5.11) gives,

$$\frac{\partial s}{\partial t} = \overbrace{\frac{b_1}{(b_2 + 1)}\frac{\partial^2}{\partial x^2}\left(S_0(x)^{b_2+1}\right) + f_0(x)}^{\dot{s}_0=0}$$

$$\tag{5.13}$$

$$+b_1\frac{\partial^2}{\partial x^2}\left(S_0(x)^{b_2}\delta S\right) + \delta f(x).$$

Since,

$$\delta S = \frac{\delta s}{(1 - s_{im})},$$

this leads to,

$$\delta\dot{s} = K_2\frac{\partial^2}{\partial x^2}\left(S_0(x)^{b_2}\delta s\right) + \delta f(x),$$

$$\tag{5.14}$$

where,

$$K_2 = \frac{b_1}{(1 - s_{im})}.$$

$$\tag{5.15}$$

Changing to the standard u PDE format with $u \triangleq \delta s$,

$$u_t = K_2\frac{\partial^2}{\partial x^2}\left(S_0(x)^{b_2}u\right) + \delta f(x).$$

$$\tag{5.16}$$

Performing the differentiation from,

$$u_t = \frac{\partial}{\partial x}\left(\frac{\partial}{\partial x}\left(K_2 S_0(x)^{b_2}u\right)\right) + \delta f(x),$$

$$\tag{5.17}$$

and defining,

$$\psi(x) \triangleq K_2 S_0(x)^{b_2},$$

$$\tag{5.18}$$

$$u_t = \frac{\partial}{\partial x} \left(\psi_x(x)u + \psi(x)u_x \right) + \delta f(x).$$

$$u_t = \frac{\partial^2 \psi(x)}{\partial x^2} u + \frac{\partial \psi(x)}{\partial x} u_x + \frac{\partial \psi(x)}{\partial x} u_x + \psi(x)u_{xx} + \delta f(x).$$

Hence, the linearized system is then,

$$u_t = \psi(x)u_{xx} + 2\psi(x)_x u_x + \psi(x)_{xx}u + \delta f(x). \tag{5.19}$$

5.2.3 Transformation of the Linearized PDE

To obtain a form conducive to stability analysis (i.e., eliminating the u_x term), the linearized PDE (5.19) can be transformed using,

$$u = we^{-\int_0^x \frac{\psi_\theta(\theta)}{\psi(\theta)} d\theta}, \tag{5.20}$$

and defining

$$\xi(x) \triangleq \frac{\psi(x)_x}{\psi(x)} \tag{5.21}$$

so that,

$$u_t = w_t e^{-\int_0^x \xi(\theta)d\theta},$$

this transforms each form of the function u in (5.19),

$$u_x = w_x e^{-\int_0^x \xi(\theta)d\theta} - w\xi e^{-\int_0^x \xi(\theta)d\theta},$$

$$u_{xx} = (w_{xx} - w_x\xi - w_x\xi - w\xi_x + w\xi^2)e^{-\int_0^x \xi(\theta)d\theta}.$$

Putting these definitions into (5.19), and multiplying through by the inverse of the transformation $(e^{\int_0^x \xi(\theta)d\theta})$,

$$w_t = \psi(w_{xx} - 2w_x\xi - w\xi_x + w\xi^2)$$

$$+2\psi_x(w_x - w\xi) + \psi_{xx}w + \delta f \cdot e^{\int_0^x \xi(\theta)d\theta}, \tag{5.22}$$

where only the w is a function of x and t, and the (x) notation for $\xi(x), f(x)$, and $\psi(x)$ has been dropped for simplicity.

The spatial derivative of ξ is,

$$\xi_x = \frac{\partial}{\partial x}\left(\frac{\psi_x}{\psi}\right) = \frac{\psi_{xx}}{\psi} - \frac{\psi_x^2}{\psi^2}. \tag{5.23}$$

Let $\tilde{f} \triangleq \delta f e^{\int_0^x \xi(\theta)}$, and inserting (5.21) and (5.23) into (5.22),

$$w_t = \psi\left(w_{xx} - 2w_x\frac{\psi_x}{\psi} - w\left(\frac{\psi_{xx}}{\psi} - \frac{\psi_x^2}{\psi^2}\right) + w\left(\frac{\psi_x}{\psi}\right)^2\right)$$
$$+ 2\psi_x(w_x - w\frac{\psi_x}{\psi}) + \psi_{xx}w + \tilde{f},$$

or,

$$w_t = \psi w_{xx} - 2w_x\psi_x - w\psi_{xx} + w\frac{\psi_x^2}{\psi} + w\frac{\psi_x^2}{\psi}$$
$$+ 2\psi_x w_x - 2w\frac{\psi_x^2}{\psi} + \psi_{xx}w + \tilde{f},$$

and canceling like terms,

$$w_t = \psi(x)w_{xx} + \tilde{f}. \tag{5.24}$$

Next, the transformed boundary conditions must be clarified. For the linearized PDE, the boundary conditions are,

$$w(L, t) = u(L, t)e^{\int_0^L \xi(\theta)d\theta} = 0 \cdot e^{\int_0^L \xi(\theta)d\theta} = 0, \tag{5.25}$$

and,

$$w_x(0, t) = u_x(0, t)e^{\int_0^0 \xi(\theta)d\theta} - u(0, t)\xi(0)e^{\int_0^0 \xi(\theta)d\theta}$$
$$= 0 \cdot e^0 - u(0, t)\xi(0)e^0,$$

to show $\xi(0) = \psi_x(0)/\psi(0) = 0$, recall $\psi(x) = K_2 S_0(x)^{b_2}$, and,

$$\psi_x(x) = b_2 K_2 S_0(x)^{b_2-1}\frac{\partial}{\partial x}S_0(x). \tag{5.26}$$

Thus, by the boundary conditions at $x = 0$,

$$\frac{\partial}{\partial x}S_0(0) = 0.$$

Therefore, $\psi_x(0) = 0$, and $w_x(0, t) = 0$.

5.2.4 Stability of the Transformed PDE

Modifying the steps described in [60] to fit our application, a Lyapunov stability analysis will be applied to the plant of the transformed system (5.24), where the $\tilde{f}$ is set to zero for the stability analysis because it is an exogenous input, and not a function of w.

To normalize the spatial variable, a $z = \frac{x}{L}$ transformation could be made so that (5.24) becomes $w_t(z,t) = \frac{1}{L^2}\psi(x)w_{zz}(z,t)$, but just take $L=1$ for convenience, without loss of generality.

Using the candidate Lyapunov function,

$$V = \frac{1}{2}\int_0^1 \frac{w^2(x,t)}{\psi(x)}dx + \frac{1}{2}\int_0^1 w_x^2(x,t)dx, \tag{5.27}$$

where it should be noted that $\psi(x) > 0$ over the range $x \in [0,1]$, because as $x \to 1$, $\psi(x) \to K_2 S_\delta^{b_2}$.

Taking the time derivative of the candidate Lyapunov function (dropping the arguments for brevity),

$$\dot{V} = \int_0^1 \left(\frac{ww_t}{\psi} - \frac{1}{2}\frac{w^2\psi_t}{\psi^2}\right)dx + \int_0^1 w_x w_{tx}dx,$$

where $\psi_t = 0$ since ψ is not a function of time. Substituting the transformed PDE, $w_t = \psi w_{xx}$, and integrating by parts,

$$\dot{V} = \int_0^1 ww_{xx}dx + \int_0^1 w_x w_{tx}dx,$$

$$\dot{V} = ww_x\Big|_0^1 - \int_0^1 w_x^2 dx + w_x w_t\Big|_0^1 - \int_0^1 \psi w_{xx}^2 dx.$$

Because the boundary conditions of the linearized, transformed system are,

$$w(1,t) = 0, \quad w_x(0,t) = 0,$$

and hence,

$$w_t(1,t) = 0,$$

then,

$$\dot{V} = -\int_0^1 w_x^2 dx - \int_0^1 \psi w_{xx}^2 dx. \tag{5.28}$$

73

Since $\dot{V} \leq 0$, we have stability in the sense of Lyapunov. To show exponential stability, recognize that $0 < \psi_{min} \leq \psi$, and apply Poincare's inequality to show,

$$-\int_0^1 w_x^2 dx \leq -\gamma\psi_{min} \int_0^1 \frac{w^2}{\psi} dx, \tag{5.29}$$

and

$$-\int_0^1 \psi w_{xx}^2 dx \leq -\gamma\psi_{min} \int_0^1 w_x^2 dx, \tag{5.30}$$

where $\gamma = \frac{1}{4}$. Then,

$$\dot{V} \leq -\gamma\psi_{min} \left(\int_0^1 \frac{w^2}{\psi} dx + \int_0^1 w_x^2 dx \right), \tag{5.31}$$

which becomes,

$$\dot{V} \leq -2\gamma\psi_{min}V, \tag{5.32}$$

indicating that $V \to 0$ exponentially as $t \to \infty$. To show pointwise convergence, use Agmon's inequality (with $w(1,t) = 0$),

$$\max_{x\in[0,1]} |w(x,t)|^2 \leq 2||w(\cdot,t)|| \cdot ||w_x(\cdot,t)||, \tag{5.33}$$

and the inequality $2||a|| \cdot ||b|| \leq ||a||^2 + ||b||^2$ to find,

$$\max_{x\in[0,1]} |w(x,t)|^2 \leq ||w(\cdot,t)||^2 + ||w_x(\cdot,t)||^2, \tag{5.34}$$

where $|| \cdot ||$ denotes the 2- norm. Since $\psi(x) > 0$ for all x and $V \to 0$, $||w(x,t)|| \to 0$ and $||w_x(x,t)|| \to 0$ as $t \to \infty$, implying,

$$\max_{x\in[0,1]} |w(x,t)| \to 0 \text{ as } t \to \infty. \tag{5.35}$$

Pointwise convergence is thus shown, and the liquid water distribution within the GDL is exponentially stable.

5.3   Stabilizing Equilibrium

Considering the water management goal of minimizing flooding and maximizing membrane hydration, the idea is to search for an equilibrium condition with zero liquid flow into the channel and the highest possible water content in the GDL.

Of course, this assumes that there exists a stable liquid water distribution in the GDL that does not significantly hinder reactant access to the catalyst. GDL liquid stability is shown in Sec. 5.2, and [4] used neutron imaging to show that typical steady-state levels of liquid water in the anode GDL do not significantly reduce voltage output, perhaps due to a randomly distributed nature of the liquid within the porous medium.

The top plot of Fig. 5.2 shows the results from a set of conditions that begin under a state of flooding ($W^{mb} > W_v^{out} - W_v^{in}$), generated with a stack current of 45A, stack temperature at 333K, and a hydrogen excess ratio of 2.5. All sections of the 10-section discretization have saturation levels above s_{im}, which will generate an undesirable liquid water flow into the channel and cause the increase in m_l^{ch} seen prior to $t = 1000$s. At $t = 1000$s, the H_2 excess ratio (λ_{H_2}) is increased to 2.63, sufficient to dry the anode channel, and force the two-phase water front to recede into the GDL. The transient response of the liquid water (Fig. 5.2) shows the water saturation of the section closest to the channel (sec. 10) being driven to zero, at which time the liquid water in sec. 9 begins to fall. The process continues until the front reaches sec. 7, attaining equilibrium because GDL flow-in (i.e. W^{mb}) increased to match the net channel flow-out (i.e. $W_v^{out} - W_v^{in}$).

To illustrate the mechanisms leading to equilibrium, consider the lower plot of Fig. 5.2, where plots of relevant mass flow rates are shown. Initially in a flooding condition, the H_2 excess ratio step at $t = 1000s$ creates a drying condition. The W_l^{GDL} is sufficient to balance the GDL water mass in the first 1000s, prior to the λ_{H_2} increase. The mobile two-phase water front recedes into the GDL as sec. 10, nearest the channel, reaches zero liquid volume. After $t = 1000$s, it can be seen from (5.8) and Fig. 5.2 that the liquid water flow decreases in proportion to the increase in water vapor flow resulting from the reduction in channel water vapor concentration caused by the channel water mass imbalance. In physical terms, at the start of a flooding-to-drying transition (i.e. $W^{mb} > W_v^{out} - W_v^{in} \rightarrow W_v^{out} - W_v^{in} > W^{mb}$), the net GDL-channel water flow is insufficient to satisfy the water mass balance in the channel, causing liquid evaporation, net water transport out of the GDL, and a decrease in the channel water vapor concentration below saturation level. The GDL nearest the channel will experience liquid volume decrease as more vapor is drawn by the sub-saturated channel, leading to a decrease in liquid flow to the channel. Once the liquid flow has ceased, the vapor mass flow out of the GDL continues to increase and can reach flow rates greater than the steady liquid mass flow rate experienced when $m_l^{ch} > 0$ and $c_v^{ch} = c_v^{sat}$. The W_v^{GDL} is increased by further decreases in c_v^{ch}
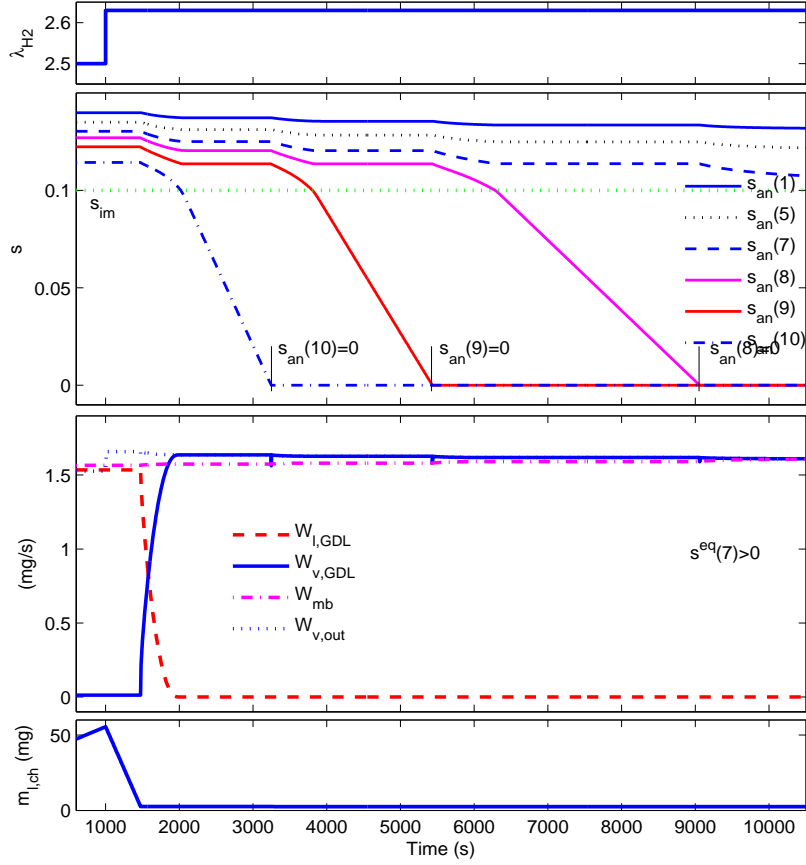
Figure 5.2: The transition from almost complete liquid transport to complete vapor transport across the GDL-channel boundary.

until the GDL water equilibrates. Equilibrium is finally reached when the mobile front reaches sec. 7 (i.e. $s_{an}(7) > 0$).

Under transient drying conditions ($W_v^{out} - W_v^{in} > W^{mb}$) the limitation that $W_{l,ss}^{GDL} < W^{mb}$ requires channel mass balance be obtained through vapor transport. To establish equilibrium, W^{mb} must increase, and this will happen only when the water vapor GDL-channel transport increases. Until liquid flow reaches zero, any increase in W_v^{GDL} occurs with a corresponding loss in liquid flow. The W_v^{GDL} growth to match $W_v^{out} - W_v^{in}$ will eliminate W_l^{GDL} as the two-phase front recedes from the channel.

Claim C: $c_v^{ch} = 2c_v^{sat} - c_{v,ss}^{mb}$ implies stable equilibrium and maximum GDL hydration

A channel water vapor concentration that is below the saturation water vapor concentration by the same amount that c_v^{mb} is above it will result in zero liquid flow into the channel. This condition will also maximize water in the GDL for all zero liquid GDL to channel flow conditions.

Using the steady state water vapor solution, the Claim implies,

$$\left(\alpha_1 e^{\beta x} + \alpha_2 e^{-\beta x}\right)\bigg|_{x=0} = -\left(\alpha_1 e^{\beta x} + \alpha_2 e^{-\beta x}\right)\bigg|_{x=L}, \tag{5.36}$$

or,

$$\alpha_1 + \alpha_2 = -\left(\alpha_1 e^{\beta L} + \alpha_2 e^{-\beta L}\right). \tag{5.37}$$

Maximum GDL hydration will occur when the two-phase front is located at $x = L$, the GDL-channel interface. To find the water vapor concentration at the two-phase front $(c_v(x_{fr}) = c_v^{ch})$ with zero liquid flow into the channel, use the knowledge that $W_l^{GDL} \to 0$ as $W_v^{GDL} \to W_v^{out} - W_v^{in}$, and steady-state mass continuity, to show that after $W_l^{GDL} = 0$, $W_v^{GDL} \to W^{mb}$ at equilibrium. Since the mass flow is related to the slope of the water vapor distribution by,

$$W_v^{GDL} = -M_v \varepsilon A_{fc} D_v^{s_{im}} \frac{dc_v}{dx}\bigg|_{x=L}, \tag{5.38}$$

and,

$$W^{mb} = -M_v \varepsilon A_{fc} D_v^{s_{im}} \frac{dc_v}{dx}\bigg|_{x=0}, \tag{5.39}$$

this implies:

$$\frac{dc_v(x)}{dx}\bigg|_{x=L} = \frac{dc_v(x)}{dx}\bigg|_{x=0}. \tag{5.40}$$

Taking the spatial derivative of (4.8a),

$$\frac{dc_v(x)}{dx} = \beta \left(\alpha_1 e^{\beta x} - \alpha_2 e^{-\beta x}\right), \tag{5.41}$$

and recognizing that equality of the water vapor slopes at the boundaries implies,

$$\alpha_1 e^{\beta L} - \alpha_2 e^{-\beta L} = \alpha_1 - \alpha_2, \tag{5.42}$$

when $N^{mb} = N_v^{GDL}$.

Therefore, to prove the Claim, it is only necessary to show (5.37), which can be done by direct algebraic manipulation after substituting (5.42) into both sides of (5.37), indicating that, indeed, $c_v^{ch} = 2c_v^{sat} - c_v^{mb}$ when $N^{mb} = N_v^{GDL}$. Since $N_v^{GDL} = N^{mb}$ implies $W_l^{GDL} = 0$, system stability is guaranteed.

5.4   Control Objective Concept

The fuel cell model's estimation of liquid flow into the channel is used both for prediction of voltage degradation and as an indication of flooding in the fuel cell that is highly detrimental to fuel cell performance and longevity. The semi-analytic model of the liquid water and water vapor distributions can be utilized to control anode channel liquid water accumulation, and thus potentially avoid voltage output degradation due to excessive water in the anode. The issue of the appropriate channel liquid water boundary condition (2.21) can be avoided completely by setting the control objective for the channel water vapor concentration such that the liquid water boundary condition at $S(L, t) = 0$, thus stabilizing the nominally unstable channel liquid water dynamics.

Figure 5.3 demonstrates that the steady-state solution to the water vapor PDE has an exponential form, while the liquid PDE is a fractional power polynomial. These shapes are highly dependent upon the choice of BC, as evidenced by results from [9], where numeric results show much higher liquid ratios ($s>0.80$) at the membrane and zero liquid water at the channel, due to the assumptions of liquid water transport across the membrane and $s = 0$ at the GDL-channel interface. Recent results [48] support the membrane boundary condition (2.20) used here.

The dash-dot line in Fig. 5.3 demonstrates that liquid water in excess of the immobile saturation (i.e. flooding) exists in the GDL when the water vapor concentration has reached its maximum value of c_v^{sat} in the channel. Under these conditions, the liquid water will grow unbounded in the channel (instability). The solid line represents a lower channel water vapor concentration, and a channel condition ($c_v^{ch} = c_v^{ch*}$) below which the GDL two-phase boundary begins to recede into the GDL (stable with $x_{fr} = L$) is observed. The dotted line depicts the steady-state distributions if $c_v^{ch} < c_v^{ch*}$, where the two-phase water front has receded into the GDL (stable with $s(L^-) = 0$).

The water vapor concentration at the vapor transition, $c_v(x_{fr})$, plays a key role in our model. Regardless of the position, it represents the boundary condition for
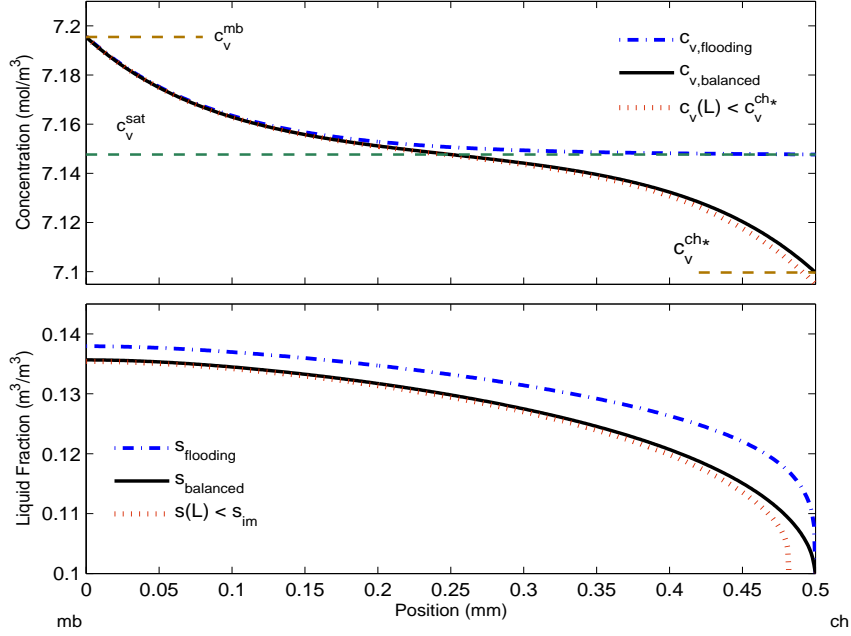
Figure 5.3: Channel water vapor concentration boundary value can shape the liquid water distribution. The flooding case has $c_v^{ch} = c_v^{sat}$, while the borderline case has $c_v^{ch} = c_v^{ch*}$, and the GDL drying case has $c_v^{ch} < c_v^{ch*}$.

the exponential solution. Based on Sec. 5.3 **Claim C**, it is proposed that

$$c_v^{ch*} = 2c_v^{sat} - c_{v,ss}^{mb}. \tag{5.43}$$

is a control objective that satisfies equilibrium, eliminates GDL-channel liquid transport, provides channel stability, and maintains the membrane water content at the highest value for a given set of conditions. The estimate of $c_{v,ss}^{mb}$ is generated by the model, and updated at every time step. A discussion on the practicality of the defined control objective follows in **Note 3**.

The c_v^{ch*} reference value is an upper bound to prevent flooding and maximize membrane water content. The unit fuel cell model from this research can be used to investigate a lower bound for the outlet humidity by using the model stacking capability demonstrated in Sec. 4.3.2 to estimate the inlet membrane humidity under various reactant excess ratios, temperatures, and/or stack currents. The modeled result would then be compared to acceptable water content levels for the membrane.

Note 3: The volumetric evaporation constant (γ), taken for this work from [5], plays a significant role in determining the c_v^{ch*}. For $\gamma = 900\text{s}^{-1}$, it is likely that c_v^{ch*} will be within 2% of saturation, and use of the outlet humidity near saturation as

the reference output presents an issue of sensor resolution and function. Near saturation, typical sensors can become clogged with liquid, rendering them temporarily ineffective. These issues may be resolved with heated, high-resolution sensors, or with innovative control algorithms. Another implementation issue that needs to be considered is the control of the hydrogen supply. Due to the low flow rates and low molecular weight, the flow controllers required to deliver the hydrogen to within the ± 0.05slm that will be necessary are quite expensive. However, control of the hydrogen supply is being addressed by industry (e.g. [61, 62]), and cost-reduction progress is expected.

5.5 Controllability

As described in Sec. 5.4, to eliminate liquid flow from GDL to channel, it is sufficient to maintain the GDL two-phase active front at $x \leq L$. Therefore, in support of this proposal, a controllability analysis will determine whether such control is mathematically possible, as well as indicate the input(s) best-suited to shape the liquid water distribution and the output(s) required. Because the liquid water states represent liquid water present in the discretized portion of the SAS model, the controllability-observability (C-O) analysis is performed on the linearized system (and not using the infinite dimensional PDE).

The proposed $x_{fr} = L$ location for the control objective coincides with the boundary conditions for the PDEs that describe the flows and distributions within the GDL. Placement of the active two-phase front at this location is challenging because $x = L$ is also the boundary of the switching analytic solution. Since the analysis is based upon a linearized system of switching nonlinear equations, the local C-O for three scenarios must be considered; $x_{fr} < L$ (receding front), $x_{fr} = L$ (the control objective), and for net liquid flow into the channel (flooding).

5.5.1 On the Choice of Controllability-Observability Test

A number of C-O tests exist, ranging from the simple C-O matrix rank tests to computation of the respective grammians to determine if they are positive definite.

The stiff system characteristics of our model lead to an unavoidably (short of time-scaling) large condition number. Unit scaling was performed to reduce the

condition number, but even the minimum condition number (κ_{min}), represented by

$$\kappa_{min} = \frac{\lambda_i^{max}}{\lambda_i^{min}}, \text{ with } \kappa \triangleq \frac{\sigma_i^{max}}{\sigma_i^{min}}, \tag{5.44}$$

and where σ and λ are the singular values and eigenvalues of the linearized system matrix A, is on the order of 10^6. Condition numbers of this magnitude are cause for concern, possibly causing large magnification of errors under matrix inversion due to computer rounding or modeling error.

The basic C-O analysis using

$$Co = [B \quad AB \quad A^2B \quad ...A^n] \qquad \text{and} \qquad Ob = \begin{bmatrix} C \\ CA \\ CA^2 \\ \vdots \\ CA^n \end{bmatrix} \tag{5.45}$$

matrix rank tests will be avoided here due to their reliance on interpretation of the rank of matrices with large condition numbers. A large condition number makes interpretation of rank subjective, as a decision must be made regarding C-O based on singular value relative magnitudes even though those values may on the order of 10^{30}. Further, the rank test does not provide information on which modes of the system are controllable/observable, or the degree of controllability.

The Popov-Belevitch-Hautus (PBH) eigenvalue test has the benefit of being able of identifying C-O for each mode, because the controllability test is simply,

$$\text{rank}[\lambda_i I - A \quad B] = n \quad \forall \lambda_i \in \mathcal{C}, \tag{5.46}$$

where each eigenvalue is tested and full rank indicates controllability. The requirement for observability of a mode is similarly found by,

$$\text{rank} \begin{bmatrix} \lambda_i I - A \\ C \end{bmatrix} = n \quad \forall \lambda_i \in \mathcal{C}. \tag{5.47}$$

The PBH eigenvalue method still requires rank determination on a matrix with high condition number.

The PBH eigenvector test, on the other hand, provides a simple means to associate modes and their relative controllability, yet does not require a matrix rank

evaluation. The concept behind the PBH eigenvector tests is based on considering the input and output matrices as operators that map the modes of the system to another space. If that space is the null space, then that mode is uncontrollable or unobservable or both, depending upon whether the input or output matrix was used in the test. Taken from [63], these test can be represented by:

$$\bar{q}A = \lambda\bar{q} \qquad \text{where } \bar{q} \text{ is a LH (row) eigenvector of } A,$$

from which $\bar{q}B=0$ implies $\bar{q}$ is an uncontrollable mode, and similarly,

$$A\bar{v} = \lambda\bar{v} \qquad \text{where } \bar{v} \text{ is a RH (column) eigenvector of } A,$$

and $C\bar{v}=0$ implies $\bar{v}$ is an unobservable mode.

The result of this mapping is a scalar value for each mode against each input or output vector in the matrices B and C. While the magnitude of the scalar value can be interpreted as an indication of the relative C-O of the mode versus a specific input/output, it should be noted that scaling will play an enormous role in comparison of results. For example, it would be ill-advised to compare the magnitude of the result of a concentration mode with the result of a liquid saturation mode. Further, the balancing algorithm employed to decouple the system uses scaling. For the purposes of this test, if the resultant is non-zero, there is some degree of controllability or observability, and comparisons should only be made between modes of like units for the same scaling.

The modal analysis performed in 3.4 presented a coordinate transformation that left only a very weak coupling between GDL liquid water and channel water vapor states. It is precisely this coupling that will be shown with the PBH eigenvector test to allow controllability of the liquid states. Further, is is demonstrated that the degree of coupling is affected by the operating point. For example, with the inputs described in Sec. 5.5.2, greater controllability of the liquid water modes is obtained when the channel condition is sub-saturated than when it is saturated. Conversely, during anode flooding and the associated channel vapor saturation, the GDL anode liquid water becomes uncontrollable, yet observability is gained using the cell voltage output.

5.5.2 Available Control Inputs

The possible control inputs for our system are related to channel constituent flow rates. The most straightforward input is the humidification of the inlet streams. In practice, both anode and cathode inlet streams can be humidified, though it is typical in our experiments to set the cathode inlet at 100% and the anode inlet at nearly 0% relative humidity, respectively. For this study, the general case of actuation via humidified inlet stream is assumed for both electrodes.

The control analysis is generalized to a flow-through anode outlet configuration for the following reasons:

1. Dead-ended systems more readily accumulate undesirable elements such as nitrogen and water.
2. A purge is a sudden and aggressive event, making data acquisition problematic, resulting in inconsistent data for model verification.
3. The purge duration necessary to efficiently remove channel water is difficult to gauge, with experience being the main determining factor.
4. The modeling assumption of water as vapor only at the channel outlet is more accurate for flow-through under small pressure differential.
5. The sudden flow dries out portions of the porous media deep into the GDL, adding repetitive drying/wetting cycles that reduce GDL longevity.
6. Possibly counter-intuitively, in spite of the 0.5% anode valve opening time compared to flow-through, cyclic purging has lower hydrogen utilization.

Flow-through anode flow control has negative aspects, the most notable being related to the ability to accurately provide the requested flow rates, as the small molecular weight and low flow rates required make measurement difficult. Progress on flow sensors and humidity measurement devices is steady, so this is not expected to be a technological hurdle.

Typical implementation methods for the reactant flow rates include pressure control and flow control. In flow control, the upstream pressure is held constant, and a valve opening position is determined to provide the desired flow rate into the channel,

$$W^{in} = u_{flow} \cdot k^{in}(P_{source} - P^{ch}), \tag{5.48}$$

where $u_{flow} \in [0, 1]$ is the position of the upstream valve, P^{ch} is the total pressure in the channel, P_{source} is the pressure upstream of the channel inlet, and k^{in} is an experimentally determined linear nozzle coefficient.

In pressure control, the channel pressure is controlled via an outlet valve open-

ing,

$$W^{out} = \bar{u} \cdot k^{out} \left(P^{ch} - P^{amb} \right), \tag{5.49}$$

where $\bar{u} \in [0, 1]$ is the position of the downstream valve, P^{amb} is the ambient pressure, and k^{out} is another experimentally determined linear nozzle coefficient.

Since the end result in both cases can be related to reactant excess ratios λ_{H_2} and λ_{O_2}, to maintain generality these will be the third and fourth inputs considered in the analysis. The input function is then,

$$u = g(RH_{an}^{in}, RH_{ca}^{in}, \lambda_{H_2}, \lambda_{O_2}). \tag{5.50}$$

In line with the goal of establishing a model for anode water distribution control, the focus is on the anode channel inputs. The cathode side inputs of oxygen excess ratio and inlet humidity are included in the analysis, but it is shown that they have little effect on controllability outside the O_2 and N_2 distributions. Further, the λ_{O_2} input is commonly used for fuel cell power control and O_2 starvation prevention, suggesting that it would be prudent to leave the cathode inputs out of the anode side water control discussion.

In this work 16 cases are studied, combining variations in operating point and degree of model order reduction. Table 5.1 lists the key cases considered (each condition from column one is tested for each model of column 2).

Condition	Model	
Flooding	24-state	Full numeric model
Borderline	10-state	SAS model (6 GDL liquid + 4 channel gas states)
$0 < s[n] < s_{im}$	7-state	Reduced SAS model (3 GDL liquid + 4 channel gas states)
Receded	4-state	Steady-state model (4 channel gas states)

Table 5.1: Cases Studied for Controllability/Observability

Additionally, for the 10-state model, 4 more tests combining the two practically available outputs were compared. The voltage output, based on a voltage degradation prediction model (see Appendix E), and measurement of relative humidity (ϕ) in the channel were compared for flooding and borderline cases. The point is to determine the effect on observability for each of these outputs alone, and together. The voltage model enables the greatest range of observable states, due to its dependence upon liquid water in the anode channel, concentrations of oxygen, hydrogen, water vapor

at the membrane, stack current, and temperature,

$$v_{cell} = f(m_{l,an}^{ch}, c_{va n}^{mb}, c_{v,ca}^{mb}, c_{H_2}^{mb}, c_{O_2}^{mb}, I_{st}, T_{st}), \tag{5.51}$$

whereas relative humidity is only a function of water vapor concentration and temperature,

$$\phi = f(c_{v,an}^{ch}, T_{st}). \tag{5.52}$$

5.5.3 Surrogate States for Reduced Models

Residualization of the fast states by analytic solution to form algebraic equations has an influence on the state matrices of the fuel cell model. For example, in the full-order 24-state model, the water vapor was a dynamic state in each spatially-discretized section. Upon implementation of the analytic solution for $c_{v,an}(x,t)$, the water vapor dynamic states are removed, and the analytic solution is inserted into dynamic state equations for $s_{an}(x,t)$. Given identical operating conditions, the SAS reduced model has very different state equations, as shown by (5.53)~(5.55). In these two examples residualization of the fast states has transferred the contributions of the gas states in the full-order model to the remaining dynamic states in the reduced-order model that determine their analytic solutions. These surrogate states are the boundary conditions for the analytic solutions implemented.

When reducing the full-order system to a reduced-order system under non-flooding conditions, with $I_{st} = 75$A, $T_{st} = 333$K, $RH_{an}^{in} = 0$, $\lambda_{H_2} = 187\%$, and voltage output, the linearized output matrix C is algebraically altered:

$$C_{full} = 0.747c_{v,an}[1] + 0.747c_{v,ca}[1] + 0.493c_{H_2}[1] + 20.9c_{O_2}[1], \tag{5.53}$$

$$C_{red} = 0.492c_{H_2}^{ch} + 20.3c_{O_2}^{ch} + 0.024m_{w,an}^{ch}. \tag{5.54}$$

Using as an example the liquid saturation nearest the channel, the state equations also change,

$$\dot{s}_{an}[3]_{full} = 0.110s_{an}[2] - 0.131s_{an}[3] + 0.016c_{v,an}[3],$$

$$\tag{5.55}$$

$$\dot{s}_{an}[3]_{red} = 0.082 s_{an}[2] - 0.043 s_{an}[3] + 0.0179 m_{w,an}^{ch}[3].$$

The hydrogen, oxygen, and anode vapor contributions have been related to their channel boundary conditions through the analytic solution, and are represented by the associated channel states. With the loss of the dynamic water vapor states, the cathode GDL water vapor distribution is influenced only through the membrane by the anode water vapor distribution. In the full-order model, membrane water content is a function of the humidities in both anode and cathode at $x = 0$. However, with the removal of water vapor states, Table 5.2 shows that the water vapor concentration membrane gradient becomes only a function of anode channel water vapor.

Removed State	Surrogate State
$c_{v,ca}(x,t)$	$m_{w,an}^{ch}$
$c_{v,an}(x,t)$	$m_{w,an}^{ch}$
$c_{O_2}(x,t)$	$c_{O_2}^{ch}$
$c_{H_2}(x,t)$	$c_{H_2}^{ch}$

Table 5.2: States in the output matrix removed by analytic solutions are replaced by remaining surrogate states.

5.5.4 Controllability-Observability Results

Of foremost concern is whether all the unstable modes are controllable and observable. As shown in Sec. 5.2, the liquid water states within the GDL are stable under any reasonable range of conditions, yet the system experiences unbounded growth from bounded inputs. The unstable state of concern is the water mass in the anode channel, as this leads to voltage degradation in the short term, and will cause fuel cell shut down if not addressed.

5.5.5 Controllability-Observability Tables

The results of the PBH tests for the various model cases and condition sets. In the table headings, the number refers to the number of states in the model (24 is the full-order model). The letter (in the observability table) indicates the output used (Voltage and/or Humidity of anode channel). The modes column references mode

groupings of states. Due to the nature of the modes and the model, the liquid states on the anode tend to form modes (3) together, as do the cathode O_2 states, the channel states on each electrode, etc.

Table 5.3: Controllability PBH Eigenvector Test Result

Mode	Flooding			Borderline			$s_{an}[3] < s_{im}$			Receding
	24	10	7	24	10	7	24	10	7	10
s_{an}	0	0	0	0.066	0.074	0.074	0.088	0.072	0.074	0.110
s_{an}	0	0	0	0.025	0.037	0.037	0.011	0.011	0.011	0.104
s_{an}	0	0	0	0.002	0	0	0.011	0.011	0.011	0.066
s_{ca}	0	0	−	0	0	−	0	0	−	0
s_{ca}	0	0	−	0	0	−	0	0	−	0
s_{ca}	0	0	−	0	0	−	0	0	−	0
$m_{w,an}^{ch}$	0.043	0.089	0.089	12.0	11.9	11.9	12.2	11.6	11.9	11.9
c_{an}^{ch}	18.3	19.4	19.4	15.4	16.9	16.9	10.5	16.8	16.8	17.0
c_{ca}^{ch}	28.0	21.3	21.3	28.0	21.3	21.3	28.0	21.3	21.3	21.3
c_{ca}^{ch}	3.36	3.60	3.60	3.36	3.60	3.60	3.36	3.60	3.60	3.60
$m_{w,ca}^{ch}$	12.7	−	−	12.7	−	−	12.7	−	−	−
c_{H_2}	5.90	−	−	6.07	−	−	6.80	−	−	−
c_{H_2}	8.82	−	−	9.24	−	−	9.20	−	−	−
c_{H_2}	5.03	−	−	6.03	−	−	3.30	−	−	−
$c_{v,an}$	0	−	−	1.03	−	−	2.74	−	−	−
$c_{v,an}$	0	−	−	1.83	−	−	6.06	−	−	−
$c_{v,an}$	0	−	−	0.98	−	−	0.36	−	−	−
c_{O_2}	3.79	−	−	3.79	−	−	3.58	−	−	−
c_{O_2}	6.60	−	−	6.60	−	−	6.60	−	−	−
c_{O_2}	2.10	−	−	2.10	−	−	2.10	−	−	−
$c_{v,ca}$	0	−	−	0.34	−	−	0	−	−	−
$c_{v,ca}$	0	−	−	1.03	−	−	1.86	−	−	−
$c_{v,ca}$	0	−	−	1.36	−	−	2.27	−	−	−
c_{N_2}	6.28	−	−	6.28	−	−	6.27	−	−	−
				Markers to highlight key results (summarized below)						

Table 5.4: Observability PBH Eigenvector Test Result

Modes	Flooding					Borderline				$0<s_{an}[3]<s_{im}$		$s_{an}[3]=0$
	24V	10V	10H	10VH	7V	24V	10V	10H	10VH	24V	10V	10V
s_{an}	1.09	1.09	0	1.09	1.09	0	0	0	0	0	0	0
s_{an}	0.48	0.48	0	0.48	0.48	0	0	0	0	0	0	0
s_{an}	0.17	0.16	0	0.16	0.16	0	0	0	0	0	0	0
s_{ca}	0	0	0	0	–	0	0	0	0	0	0	0
s_{ca}	0	0	0	0	–	0	0	0	0	0	0	0
s_{ca}	0	0	0	0	–	0	0	0	0	0	0	0
$m_{w,an}^{ch}$	2.34	2.34	0	2.34	2.34	0.30	0.29	0.56	0.63	0.30	0.29	0.27
c_{an}^{ch}	0.41	0.49	0	0.49	0.46	0.62	0.46	0.23	0.52	0.61	0.46	0.47
c_{ca}^{ch}	14.7	18.1	0	18.1	18.1	14.7	18.1	0	18.1	14.7	18.1	18.1
c_{ca}^{ch}	5.64	8.49	0	8.49	8.49	5.64	8.50	0	8.50	5.64	8.50	8.50
$m_{w,ca}^{ch}$	0	–	–	–	–	0	–	–	–	0	–	–
c_{H_2}	0.76	–	–	–	–	0.77	–	–	–	0.78	–	–
c_{H_2}	0.55	–	–	–	–	0.54	–	–	–	0.54	–	–
c_{H_2}	0.17	–	–	–	–	0.17	–	–	–	0.14	–	-
$c_{v,an}$	1.22	–	–	–	–	1.16	–	–	–	1.52	–	–
$c_{v,an}$	0.40	–	–	–	–	0.52	–	–	–	1.14	–	–
$c_{v,an}$	0.13	–	–	–	–	0.16	–	–	–	0.42	–	–
c_{O_2}	29.5	–	–	–	–	29.5	–	–	–	29.5	–	–
c_{O_2}	23.4	–	–	–	–	23.4	–	–	–	23.4	–	–
c_{O_2}	7.26	–	–	–	–	7.26	–	–	–	7.26	–	–
$c_{v,ca}$	1.67	–	–	–	–	1.50	–	–	–	0.27	–	–
$c_{v,ca}$	0.42	–	–	–	–	0.42	–	–	–	0.27	–	–
$c_{v,ca}$	0.04	–	–	–	–	0.17	–	–	–	0	–	–
c_{N_2}	6.85	–	–	–	–	6.85	–	–	–	6.85	–	–
	Markers to highlight key results (summarized below)											

The controllability and observability tests for the various cases result in the following conclusions (from data shown in Tables 5.3,5.4):

1. Under flooding conditions (non-zero liquid water in the channel), the mass of water in the anode channel is a controllable mode, and can thus be steered back to zero with the anode inputs (light blue shading in Table 5.3).
2. The anode GDL liquid water modes are controllable under all non-flooding conditions (pink shading in Table 5.3).
3. During flooding, the liquid water and water vapor (yellow shading in Table 5.3) states in the GDL are uncontrollable. Under this condition, small changes in anode inlet/outlet flow do not influence water vapor concentration in the channel, thus blocking influence on GDL liquid states.
4. Observability of anode liquid water, on the other hand, improves with flooding conditions as the liquid water is seen in the degradation of the voltage due to liquid buildup in the channel (pink shading in Table 5.4).
5. GDL liquid water is only observable under flooding conditions, and then only in the anode. Cathode liquid water (GDL and channel) is unobservable under all conditions due to the decoupling of vapor and liquid under the assumption of a saturated cathode channel.
6. The number of observable mode increases significantly with use of voltage output versus use of relative humidity alone due to the many states contributing to the voltage estimation.
7. Use of relative humidity output alone results in unobservable anode channel modes during flooding (yellow shading in Table 5.4).
8. Combination of both outputs does not increase the number of modes that are observable due to output state redundancy, however observability of the anode channel modes improves when both outputs are used (light blue shading in Table 5.4).
9. When the fast (gaseous) states in the GDL are reduced to algebraic equations, those voltage output matrix GDL states are transformed to the channel concentrations via the analytic solutions (5.53).

The significance of the above results can be summarized:

- Though the GDL liquid modes are not controllable under flooding, stabilization of the anode water dynamics is possible because the unstable anode channel water mass state is controllable.
- The lack of observability of the anode channel water mass during flooding implies that a combination of cell voltage and relative humidity outputs is desirable. The voltage output is instrumental to inform the controller that actuation is needed, and ϕ has information regarding whether it is drying or flooding causing the voltage loss.
- Together with channel liquid controllability above, controllability of the GDL liquid modes under all non-flooding conditions implies control objective imple-

mentation feasibility.

- As $s[n]$ nearest the channel falls below the immobile saturation, controllability of liquid modes declines due to the buffer caused by the non-equilibrium condition in section n.
- When $s[n]=0$, controllability rebounds for the GDL liquid modes, indicating that the removal of liquid in section n re-initiates influence of the channel vapor boundary value on GDL liquid.

5.5.6   Controllability of the GDL Liquid

The full system analysis indicates that it is theoretically possible to control the anode liquid water states using the RH_{an}^{in} and λ_{H_2} inputs. To clarify the relationship between channel water vapor concentration and GDL liquid water, an analysis focused on the liquid water states is performed symbolically to demonstrate controllability.

Taking advantage of the vapor-liquid decoupling possible due to the large timescale separation between the liquid and gas states, controllability of the liquid water states is analyzed by re-casting the liquid subsystem separately. Recalling the PDE describing liquid water accumulation in the GDL,

$$\frac{\partial s}{\partial t} = \frac{-1}{\rho_l \varepsilon A_{fc}} \frac{\partial W_{l,an}}{\partial x} - \frac{M_v \gamma}{\rho_l}(c_v^{sat} - c_{v,an}), \tag{5.56}$$

and the steady-state solution for $c_{v,an}$ can be substituted,

$$\frac{\partial s}{\partial t} = \frac{-1}{\rho_l \varepsilon A_{fc}} \frac{\partial W_{l,an}}{\partial x} + \frac{M_v \gamma}{\rho_l}(\alpha_1 e^{\beta x} + \alpha_2 e^{-\beta x}). \tag{5.57}$$

Defining $\Delta c_v^{ch} \triangleq c_{v,an}^{ch} - c_v^{sat}$, the α_i coefficients can be shown to be,

$$\alpha_1 = \frac{\Delta c_v^{ch} - \frac{N^{mb}}{\beta D_v^{sim}} e^{-\beta L}}{(e^{\beta L} + e^{-\beta L})}, \tag{5.58}$$

$$\alpha_2 = \frac{\Delta c_v^{ch} + \frac{N^{mb}}{\beta D_v^{sim}} e^{\beta L}}{(e^{\beta L} + e^{-\beta L})}. \tag{5.59}$$

Substituting in the PDE for $W_{l,an}$ from 2.11, and separating the boundary value control input Δc_v^{ch} from the disturbance input N^{mb} (another boundary value for the GDL water vapor states),

$$\frac{\partial s(x,t)}{\partial t} = \frac{b_1}{b_2 + 1} \frac{\partial^2}{\partial x^2}\left(S(x,t)^{b_2+1}\right) + B_k(x)\Delta c_v^{ch} + E_k(x)N^{mb}, \tag{5.60}$$

where

$$B_k(x) = \frac{M_v \gamma \left(e^{\beta x} + e^{-\beta L}\right)}{\rho_l \left(e^{\beta L} + e^{-\beta L}\right)}, \tag{5.61}$$

$$E_k(x) = \frac{M_v \gamma \left(e^{\beta(L-x)} + e^{-\beta(L-x)}\right)}{\rho_l \beta D_v^{sim} \left(e^{\beta L} + e^{-\beta L}\right)}. \tag{5.62}$$

Discretizing the spatial coordinate x into n sections enables representation of the system as n ODEs. Using the central difference second-order derivative approximation, and evaluating B_k and E_k at each section $x[k]$, the general form of one liquid water state equation becomes,

$$\frac{ds[k]}{dt} = \frac{b_1}{(b_2+1)\Delta x^2} \left(S^{b_2+1}[k+1] - 2S^{b_2+1}[k] + S^{b_2+1}[k-1]\right) + B_k[k]\Delta c_v^{ch} + E_k[k]N^{mb}, \tag{5.63}$$

which is formed into the standard state space form after linearization (assuming Δx is the same for all sections in the discretization),

$$\dot{\mathbf{s}} = A\mathbf{s} + B\Delta c_v^{ch} + EN^{mb}. \tag{5.64}$$

With $n = 3$, the system matrices are:

$$A = \frac{b_1}{\Delta x^2(1 - s_{im})} \begin{bmatrix} -S_o^{b_2}[1] & S_o^{b_2}[2] & 0 \\ S_o^{b_2}[1] & -2S_o^{b_2}[2] & S_o^{b_2}[3] \\ 0 & S_o^{b_2}[2] & -2S_o^{b_2}[3] \end{bmatrix} \tag{5.65}$$

$$B = \frac{M_v\gamma}{\rho_l\left(e^{\beta L} + e^{\beta L}\right)} \begin{bmatrix} \left(e^{\beta x[1]} + e^{-\beta x[1]}\right) \\ \left(e^{\beta x[2]} + e^{-\beta x[2]}\right) \\ \left(e^{\beta x[3]} + e^{-\beta x[3]}\right) \end{bmatrix} \tag{5.66}$$

$$E = \frac{M_v\gamma}{\rho_l\left(e^{\beta L} + e^{\beta L}\right)} \begin{bmatrix} \left(e^{\beta(L-x[1])} + e^{-\beta(L-x[1])}\right) \\ \left(e^{\beta(L-x[2])} + e^{-\beta(L-x[2])}\right) \\ \left(e^{\beta(L-x[3])} + e^{-\beta(L-x[3])}\right) \end{bmatrix} \tag{5.67}$$

For non-zero $S_o[k]$, this system will be controllable for all three modes, indicating that the liquid water distribution in the GDL is controllable using the channel water vapor concentration as a boundary value control input.

Chapter 6

Conclusions

Progress has been made toward control of PEMFC water distributions to improve efficiency and extend working life. The next steps would include implementation of high resolution, reliable sensing methods, experimental validation of the control, and design of optimizing control algorithms. Further, expansion of the model to include temperature variation would improve conditions for control to reduce excess water accumulation. The model created is expandable for performance comparisons between flow-through and dead-ended anode architectures, especially in the area of hydrogen utilization and the effect of nitrogen crossover.

Beyond fuel cells, the model order reduction method implemented here has application potential to other porous media-utilizing devices faced with PDE-based diffusion dynamics (e.g. batteries). Improving the durability of devices with porous media, multi-phase flow, and exposed to load cycles is a high priority for battery and fuel cell developers ([64]), with both passive (design) and active (automatic control) strategies under consideration. Additionally, the problem of freeze-thaw performance of fuel cells will require multi-phase models (including a third water phase), so an understanding of the water distribution in the GDL is of value.

6.1   Fuel Cell Control-Oriented Modeling

An experimentally verified, 24-state fuel cell model was simplified to only seven states using a combination of linear system theory, the energy-based model order reduction MORA, analytic PDE solutions, and error analysis. The semi-analytic solution model predicts voltage degradation due to anode flooding and reactant responses to changes in control/disturbance inputs at least as well as the full-order model. An

analytic solution switching mechanism is implemented to identify the time-varying location of the moving boundary between single and two-phase water.

The SAS model maintains the physical meanings of the states, with computational cost reduced by over 44% as judged by simulation time and number of calculations required. The SAS model created lends itself to higher resolution discretization of the PDEs, expansion to include addition of an along-the-channel dimension, temporal variation, and control algorithms simple and complex.

6.2 Control Analysis

In preparation for control application, the model has been analyzed for stability, controllability/observability, and equilibria mapping. The liquid water content in the GDL is proven to be locally exponentially stable throughout the range of normal operation. Unbounded liquid water growth in the channel is the only unstable mode, and this unstable mode is shown to be controllable with state feedback (c_v^{ch} and/or the voltage model), making the anode side overall system stabilizable.

The voltage output provides the greatest range of observability due to the presence of one state from each constituent in the voltage model. Addition of the anode channel humidity as an output increases the relative observability for the anode liquid water modes. However, the addition of humidity as an output does not increase the number of modes observable. Channel humidity has the advantage of being an explicit measurement of a state.

Analysis of the semi-analytic solution model reveals a range of values for which equilibrium cannot be reached, and suggests a desirable borderline equilibrium distribution. Thus, a control objective to stabilize the channel water state is proposed, using channel humidity as the reference. This reference humidity locates the active two-phase water front at the interface between the GDL and the channel ($x_{fr} = L$), where it has been shown that controllability of both the liquid water in the GDL and the channel water state exists using the inputs λ_{H_2} and RH_{an}^{in}. A simple P-control algorithm provides further evidence of the concept that the GDL liquid states can be controlled indirectly by control of the water vapor in the channel, which is the boundary value for the water vapor in the GDL. Since the GDL water vapor distribution is determined by the boundary, a distributed control is obtained over the GDL liquid. The boundary value control proposed has the additional benefit of providing the maximum hydration of the membrane under non-flooding conditions.

Appendices

Appendix A

Abbreviations and Nomenclature

Table A.1: Constant values and notation

Constant	Meaning	Value [units]	Notation	Meaning
γ	evaporation rate	900 [s^{-1}]	j	constituent (H_2, O_2, etc.)
A_{fc}	FC active area	0.03 [m^2]	mb	membrane
V_{an}^{ch}	ch volume	2.3×10^{-5} [m^3]	v, l, w, gas	vapor, liquid
V_{ca}^{ch}	(an, ca)	2.0×10^{-5} [m^3]		water, gas
S_δ	boundary condition at $S(x_{fr}, t)$	0.003 [-]	e	electrode (an,ca)
s_{im}	immobile saturation	0.1 [-]	ss	steady-state value
$\mathcal{R}$	universal gas constant	8.3147$\left[\frac{J}{molK}\right]$	GDL	gas diffusion layer
b_1	Liq. flow	2.42×10^{-5} [-]	$1p$	single-phase
b_2	fit constants	2.88 [-]	$2p$	two-phase
ρ_l	density	997 [kg/m^3]	rct	reaction
ε	porosity	0.5 [-]	fr	mobile front
V^{ch}	ch volume	[m^3]	amb	ambient
t^{mb}	mb thickness	3.8×10^{-5} [m]	in, out	ch in, out
k^{in}	inlet, outlet	3.89×10^{-8} [m s]	sat	saturation
k^{out}	and channel	4.71×10^{-8}[m s]	ch	channel
k^{ch}	orifice const	1.91×10^{-7} [m s]	app	apparent
K_1	tuned	1.17 [-]	C	capacitance
K_2	voltage	4.44 [μ A]	R	resistance
K_3	parameters	1.78 [-]	MR	modulated R
K_4		3.27 [-]	S$_f$	flow source
L	GDL thickness	5×10^{-4} [m]	MS$_f$	modulated S$_f$
M_j	molar mass	[kg/mol]	red	reduced model

Table A.2: Variable descriptions

Parameter	Meaning	[units]	Variable	Meaning	[units]
$\mathbf{e}$	gen. effort	[-]	$\mathcal{P}$	power	[J/s]
$\mathbf{f}$	gen. flow	[-]	i	current density	[A/m^2]
Q	vol. liquid flow rate	[m^3/s]	ϕ	relative humidity	[m^3]
AI_j	*Activity Index*	[-]	u, w	PDE sol'n dummy var	[-]
$D_j(s)$	effective diffusivity	[m^2/s]	D_w	membrane water diffusion coeff	[m^2/s]
$\bar{u}$	outlet valve control	[-]	u_{flow}	inlet valve control	[-]
$W_{j,e}$	mass flow rate]	[kg/s]	$N_{j,e}$	molar flux	[mol/m^{2}s]
α_1	anode $c_v(x)$	[mol/m^3]	ν_1	cathode $c_v(x)$	[mol/m^3]
α_2	sol'n coeffs.	[mol/m^3]	ν_2	sol'n coeffs.	[mol/m^3]
I_{st}	stack current	[A]	m^{1p}	$\frac{dc_v}{dx}\big|_{s(x,t)=0}$	[mol/m^4]
λ^{mb}, λ_e	water content	—	$c_j(x)$	concentration	[mol/m^3]
T_{st}	stack temp.	[K]	$s_e(x,t)$	saturation	[m^3/m^3]
D_j^{sim}	$D_j(s)$ w/$s = s_{im}$	[m^2/s]	$S_e(x,t)$	reduced saturation	[m^3/m^3]
P	pressure	[Pa]	m	mass	[kg]

Table A.3: Parameter descriptions

Parameter	Meaning	[units]	Sup/Subscript	Meaning	[units]
γ	evaporation rate	[s^{-1}]	λ_j	reactant $(j = H_2, O_2)$ excess ratios	[-]
α_w	tuned membrane transport parameter	[-]	s_{im}	immobile saturation	[-]
V_p	GDL pore vol.	[m^3]			

Appendix B

Separation of Variables

The details of the separation of variables method used to determine the analytic solutions are shown in this section.

Background Equations - Water Vapor

The flux equation,

$$N(x,t) = -D_v(s)\frac{\partial c_v(x,t)}{\partial x}, \tag{B.1}$$

combined with the mass balance PDE,

$$\frac{\partial c_v(x,t)}{\partial t} = -\frac{\partial N}{\partial x} + \gamma(c_v^{sat} - c_v(x,t)), \tag{B.2}$$

gives the 2nd-order equation of interest:

$$\Rightarrow \frac{\partial c_v(x,t)}{\partial t} = \frac{\partial}{\partial x}\left(D_v(s)\frac{\partial c_v(x,t)}{\partial x}\right) + \gamma(c_v^{sat} - c_v(x,t)) \tag{B.3}$$

With Boundary Conditions:

$$c_v(L,t) = c_v^{ch} \qquad \text{and} \qquad \frac{\partial c_v(0,t)}{\partial x} = -\frac{N^{mb}}{D_v(s)}. \tag{B.4}$$

So, B.3 becomes,

$$\frac{\partial c_v(x,t)}{\partial t} = D_v^{sim}\frac{\partial^2 c_v(x,t)}{\partial x^2} + \gamma(c_v^{sat} - c_v(x,t)) \tag{B.5}$$

Establish Homogeneous Boundary Conditions for SOV

Try a transformation of the form:

$$v(x,t) \triangleq c_v(x,t) - \left(\alpha_1 e^{\beta x} + \alpha_2 e^{-\beta x}\right) - c_v^{sat}, \tag{B.6}$$

where the first ' - ' sign is useful for later aesthetic purposes. Then,

$$\frac{dv(x,t)}{dx} = \frac{dc_v(x,t)}{dx} - \beta\left(\alpha_1 e^{\beta x} - \alpha_2 e^{-\beta x}\right), \tag{B.7}$$

and the first homogenous BC requirement is satisfied by,

$$\frac{dv(0,t)}{dx} = \frac{dc_v(0,t)}{dx} - \beta(\alpha_1 - \alpha_2) = -\frac{N^{mb}}{D_v^{sim}} - \beta(\alpha_1 - \alpha_2) \equiv 0. \tag{B.8}$$

Therefore,

$$\alpha_1 - \alpha_2 = -\frac{N^{mb}}{\beta D_v^{sim}}. \tag{B.9}$$

The second homogeneous BC requirement must satisfy,

$$v(L,t) = c_v(L,t) - \left(\alpha_1 e^{\beta L} + \alpha_2 e^{-\beta L}\right) - c_v^{sat} \equiv 0, \tag{B.10}$$

which leads to:

$$\alpha_1 e^{\beta L} + \alpha_2 e^{-\beta L} = c_v^{ch} - c_v^{sat}. \tag{B.11}$$

Standard 2nd Order PDE with Homogeneous Boundary Conditions

Next is determining β,

$$\frac{\partial v(x,t)}{\partial t} = \frac{\partial c_v(x,t)}{\partial t} \qquad \text{and} \qquad \frac{\partial^2 v(x,t)}{\partial x^2} = \frac{\partial c_v^2(x,t)}{\partial x^2} - \beta^2\left(\alpha_1 e^{\beta x} + \alpha_2 e^{-\beta x}\right). \tag{B.12}$$

The 2nd order PDE to be solved can now be written:

$$\frac{\partial v(x,t)}{\partial t} = D_v^{sim}\left(\frac{\partial^2 v(x,t)}{\partial x^2} + \beta^2\left(\alpha_1 e^{\beta x} + \alpha_2 e^{-\beta x}\right)\right) + \gamma\left(-v(x,t) - \left(\alpha_1 e^{\beta x} + \alpha_2 e^{-\beta x}\right)\right), \tag{B.13}$$

and if we choose,

$$\beta = \sqrt{\frac{\gamma}{D_v^{sim}}}, \tag{B.14}$$

then the simplified PDE becomes:

$$\frac{\partial v(x,t)}{\partial t} = D_v^{sim}\frac{\partial^2 v(x,t)}{\partial x^2} - \gamma v(x,t), \tag{B.15}$$

which has zero BC, but can have any initial condition that solves the steady-state case of the original PDE.

Separation of Variables (SOV)

Let's assume that the solution to (B.15) will be in the form:

$$v(x,t) = f(x)g(t), \tag{B.16}$$

so then:

$$\frac{dv(x,t)}{dt} = f(x)\frac{\partial g(t)}{\partial t} \qquad \text{and} \qquad \frac{\partial^2 v(x,t)}{\partial x^2} = \frac{\partial^2 f(x)}{\partial x^2}g(t). \tag{B.17}$$

Dropping the arguments from $f(x)$ and $g(t)$, using the common PDE notation $f_x \triangleq \partial f/\partial x$ and plugging in the $f(x), g(t)$-relationships,

$$fg_t = D_v^{sim} f_{xx}g - \gamma fg. \tag{B.18}$$

Dividing through by $D_v^{sim} fg$ gives,

$$\frac{g_t}{D_v^{sim}g} = \frac{f_{xx}}{f} - \frac{\gamma}{D_v^{sim}} \quad \text{we put the } \frac{\gamma}{D_v^{sim}} \text{ term with the 'time' equation ,} \tag{B.19}$$

$$\Rightarrow \frac{g_t}{D_v^{sim}g} + \frac{\gamma}{D_v^{sim}} = \frac{f_{xx}}{f} = \text{const } \triangleq -\lambda. \tag{B.20}$$

The Time Equation

$$g_t + \left(\lambda + \frac{\gamma}{D_v^{sim}}\right) D_v^{sim}g = 0 \qquad \text{Let } \xi \triangleq \left(\lambda + \frac{\gamma}{D_v^{sim}}\right), \tag{B.21}$$

then

$$g_t + \xi D_v^{sim}g = 0 \qquad \Rightarrow \qquad g(t) = e^{-\xi t}. \tag{B.22}$$

The Space Equation

$$f_{xx} + \lambda f = 0 \qquad \Rightarrow \qquad f(x) = A\cos(\sqrt{\lambda}x) + B\sin(\sqrt{\lambda}x). \tag{B.23}$$

The Zero Boundary Conditions

$$v_x(0,t) = 0 \quad \Rightarrow \quad f_x(0)g(t) = 0 \Rightarrow \quad f_x(0) = 0, \tag{B.24}$$

$$v(L, t) = 0 \quad \Rightarrow \quad f(L)g(t) = 0 \Rightarrow \quad f(L) = 0, \tag{B.25}$$

$$f_x(0) = \left(-A\sqrt{\lambda}\sin(\sqrt{\lambda}x) + B\sqrt{\lambda}\cos(\sqrt{\lambda}x) \right)\Big|_{x=0} = 0 \quad \Rightarrow \quad B = 0, \tag{B.26}$$

$$f(L) = A\cos(\sqrt{\lambda}L) = 0 \quad \Rightarrow \quad \sqrt{\lambda_n} = \left(n + \frac{1}{2} \right)\frac{\pi}{L}. \tag{B.27}$$

Since any linear combination of the λ_n constitutes a solution, we can write the spatial solution as an infinite sum over n:

$$f(x) = \sum_{n=0}^{\infty} A_n \cos(\sqrt{\lambda_n}x), \tag{B.28}$$

therefore, the full transformed solution is,

$$v(x, t) = e^{-\xi t} \sum_{n=0}^{\infty} A_n \cos(\sqrt{\lambda_n}x), \tag{B.29}$$

Finding the A_n Using the Initial Conditions

The initial distribution of the water vapor concentration is assumed known, and let's call that distribution,

$$c_v(x, 0) = \eta_1 e^{\beta x} + \eta_2 e^{-\beta x} + c_{v,o}^{sat}, \tag{B.30}$$

where $c_{v,o}^{sat}$ is the vapor saturation at the initial time, t_o, and β is not a function of time, so it remains unchanged. In the $v(x, t)$ transformed coordinate system,

$$v(x, 0) = c(x, 0) - (\alpha_1 e^{\beta x} + \alpha_2 e^{-\beta x}) - c_v^{sat}. \tag{B.31}$$

Now,

$$v(x, 0) = (\eta_1 - \alpha_1)e^{\beta x} + (\eta_2 - \alpha_2)e^{-\beta x} + (c_{v,o}^{sat} - c_v^{sat}). \tag{B.32}$$

Let,

$$\varphi_i \triangleq (\eta_i - \alpha_i) \text{ and } \Delta c_v^{sat} \triangleq (c_{v,o}^{sat} - c_v^{sat}), \tag{B.33}$$

so that,

$$v(x,0) = \sum_{n=0}^{\infty} A_n cos(\sqrt{\lambda_n}x) = \varphi_1 e^{\beta x} + \varphi_2 e^{-\beta x} + \Delta c_v^{sat}. \quad \text{(B.34)}$$

Applying the orthogonality argument, which is multiplying by $cos(\sqrt{\lambda_m}x)$ and integrating $\int_0^L dx$,

$$\sum_{n=0}^{\infty} A_n \int_0^L cos(\sqrt{\lambda_m}x)cos(\sqrt{\lambda_n}x)dx \quad \text{(B.35)}$$

$$= \int_0^L cos(\sqrt{\lambda_m}x) \left(\varphi_1 e^{\beta x} + \varphi_2 e^{-\beta x} + \Delta c_v^{sat} \right) dx.$$

By orthogonality, the LHS term is zero unless $m = n$, and we get,

$$A_m \frac{L}{2} = \varphi_1 \int_0^L e^{\beta x} cos(\sqrt{\lambda_m}x)dx + \varphi_2 \int_0^L e^{-\beta x} cos(\sqrt{\lambda_m}x)dx \quad \text{(B.36)}$$

$$+ \Delta c_v^{sat} \int_0^L cos(\sqrt{\lambda_m}x)dx.$$

$$\int_0^L e^{\beta x} cos(\sqrt{\lambda_m}x)dx = \frac{e^{\beta x}}{\beta^2 + \lambda_m} \left(\beta cos(\sqrt{\lambda_m}x) + \sqrt{\lambda_m} sin(\sqrt{\lambda_m}x) \right) \Big|_0^L \quad \text{(B.37)}$$

$$= \frac{e^{\beta L}}{\beta^2 + \lambda_m} \left[\sqrt{\lambda_m}(-1)^m \right] - \frac{\beta}{\beta^2 + \lambda_m},$$

$$\int_0^L e^{-\beta x} cos(\sqrt{\lambda_m}x)dx = \frac{e^{-\beta x}}{\beta^2 + \lambda_m} \left(-\beta cos(\sqrt{\lambda_m}x) + \sqrt{\lambda_m} sin(\sqrt{\lambda_m}x) \right) \Big|_0^L \quad \text{(B.38)}$$

$$= \frac{e^{-\beta L}}{\beta^2 + \lambda_m} \left[\sqrt{\lambda_m}(-1)^m \right] + \frac{\beta}{\beta^2 + \lambda_m},$$

$$\Delta c_v^{sat} \int_0^L cos(\sqrt{\lambda_m}x)dx = \frac{\Delta c_v^{sat}}{\sqrt{\lambda_m}} sin(\sqrt{\lambda_m}x) \Big|_0^L = \frac{\Delta c_v^{sat}}{\sqrt{\lambda_m}}(-1)^m. \quad \text{(B.39)}$$

$$A_m = \frac{2}{L} \left\{ \left(\varphi_1 e^{\beta L} + \varphi_2 e^{-\beta L} \right) \frac{\sqrt{\lambda_m}(-1)^m}{\beta^2 + \lambda_m} + (\varphi_2 - \varphi_1)\frac{\beta}{\beta^2 + \lambda_m} + \frac{\Delta c_v^{sat}}{\sqrt{\lambda_m}}(-1)^m \right\}, \quad \text{(B.40)}$$

Conclusion

Recalling that:

$$c_v(x, t) = v(x, t) + (\alpha_1 e^{\beta x} + \alpha_2 e^{-\beta x}) + c_v^{sat}, \tag{B.41}$$

$$c_v(x, t) = e^{-\xi_n t} \sum_{m=0}^{\infty} A_m cos(\sqrt{\lambda_m} x) + (\alpha_1 e^{\beta x} + \alpha_2 e^{-\beta x}) + c_v^{sat}. \tag{B.42}$$

Steady-state can be found by letting $t \to \infty$,

$$c_v(x) = \alpha_1 e^{\beta x} + \alpha_2 e^{-\beta x} + c_v^{sat}. \tag{B.43}$$

As a way to understand η_i is to think in terms of initial and final α_i:

$$\varphi_i = \eta_i - \alpha_i = \alpha_i \bigg|_{t=0} - \alpha_i \bigg|_{t=\infty}. \tag{B.44}$$

Appendix C

Liquid Steady-State Solution Derivation

The steady-state solution was derived from the second-order partial differential equation representing the liquid saturation in the GDL,

$$\frac{\partial s}{\partial t} = \frac{\partial}{\partial x}\left(b_1 S^{b_2}\frac{\partial S}{\partial x}\right) - \frac{M_v \gamma}{\rho_l}(c_v^{sat} - c_v(x)). \tag{C.1}$$

Substituting the quasi steady-state solution for the water vapor,

$$c_v(x) = \alpha_1 e^{\beta x} + \alpha_2 e^{-\beta x} + c_{v,sat}, \tag{C.2}$$

gives,

$$\frac{\partial s}{\partial t} = \frac{\partial}{\partial x}\left(b_1 S^{b_2}\frac{\partial S}{\partial x}\right) + \frac{M_v \gamma}{\rho_l}(\alpha_1 e^{\beta x} + \alpha_2 e^{-\beta x}). \tag{C.3}$$

Setting $\partial s/\partial t = 0$, and moving the differential term to the LHS,

$$\frac{d}{dx}\left(b_1 S^{b_2}\frac{dS}{dx}\right) = -\frac{M_v \gamma}{\rho_l}(\alpha_1 e^{\beta x} + \alpha_2 e^{-\beta x}). \tag{C.4}$$

Move the dx to the RHS, and integrate,

$$\int d\left(b_1 S^{b_2}\frac{dS}{dx}\right) = -\int_0^L \frac{M_v \gamma}{\rho_l}(\alpha_1 e^{\beta x} + \alpha_2 e^{-\beta x})dx. \tag{C.5}$$

Integrate the RHS w.r.t x, and add the constant of integration,

$$b_1 S^{b_2}\frac{dS}{dx} = -\frac{M_v \gamma}{\rho_l}\beta(\alpha_1 e^{\beta x} - \alpha_2 e^{-\beta x}) + c_1. \tag{C.6}$$

Move the dx to the RHS, and integrate,

$$\int b_1 S^{b_2} dS = -\int_0^L \frac{M_v \gamma \beta}{\rho_l}(\alpha_1 e^{\beta x} - \alpha_2 e^{-\beta x} + c_1)dx. \tag{C.7}$$

$$S^{b_2+1} = -\frac{(b_2+1)M_v\gamma\beta^2}{b_1\rho_l}(\alpha_1 e^{\beta x} + \alpha_2 e^{-\beta x} + c_1 x + c_2). \tag{C.8}$$

Let $\beta_z = \frac{(b_2+1)M_v\gamma\beta^2}{b_1\rho_l}$, and take the $1/(b_2+1)$ root of both sides,

$$S(x) = \left[-\beta_z(\alpha_1 e^{\beta x} + \alpha_2 e^{-\beta x} + c_1 x + c_2) \right]^{\frac{1}{b_2+1}}. \tag{C.9}$$

We find c_1 and c_2 from the boundary conditions, so we need the derivative of $S(x)$ w.r.t. x, for which it is convenient to define a notation for the equation inside the parenthesis of (C.9),

$$S_{inner} = -\beta_z(\alpha_1 e^{\beta x} + \alpha_2 e^{-\beta x} + c_1 x + c_2). \tag{C.10}$$

So,

$$\frac{dS}{dx} = \frac{1}{(b_2+1)}(S_{inner})^{\frac{-b_2}{b_2+1}}\frac{dS_{inner}}{dx}, \tag{C.11}$$

and recalling that we have Neumann conditions at $x = 0$ implies (because $S_{inner} \neq \infty$),

$$\frac{dS}{dx} = 0 \qquad \Rightarrow \qquad \frac{dS_{inner}}{dx} = 0. \tag{C.12}$$

This leads to,

$$\frac{dS_{inner}}{dx} = -\beta_z\beta(\alpha_1 e^{\beta x} - \alpha_2 e^{-\beta x} + c_1), \tag{C.13}$$

and thus at $x = 0$,

$$c_1 = -(\alpha_1 - \alpha_2). \tag{C.14}$$

The Robin boundary condition at $S(L) = S_\delta$, where S_δ is a non-negative small value that is not affected by the actual amount of liquid water in the channel, used with (C.9) and (C.14) gives,

$$S_\delta^{b_2+1} = -\beta_z(\alpha_1 e^{\beta L} + \alpha_2 e^{-\beta L} - (\alpha_1 - \alpha_2)L + c_2). \tag{C.15}$$

Rearranging leads to,

$$c_2 = (\alpha_1 - \alpha_2)L - (\alpha_1 e^{\beta L} + \alpha_2 e^{-\beta L}) - \frac{S_\delta^{b_2+1}}{\beta_z}. \tag{C.16}$$

Putting (C.14) and (C.16) into (C.9, and recognizing that $\alpha_1 e^{\beta L} + \alpha_2 e^{-\beta L} = c_v^{ch} - c_v^{sat}$

concludes the process,

$$S(x) = \left[\beta_z\left((\alpha_1 - \alpha_2)(x - L) - (\alpha_1 e^{\beta x} + \alpha_2 e^{-\beta x}) + (c_v^{ch} - c_v^{sat}) + \frac{S_\delta^{b_2+1}}{\beta_z}\right)\right]^{\frac{1}{b_2+1}}. \quad \text{(C.17)}$$

Appendix D

Simultaneous Solution of SAS Boundary Conditions and Coefficients

The details of the separation of variables method used to determine the analytic solutions are shown in this section.

ANODE SIDE

$$W_{H_2}^{in} = \lambda_{H_2} W_{H_2}^{rct} \tag{D.1}$$

$$W_{v,an}^{in} = \frac{P_{v,an}^{in}}{P_{an}^{in}} \frac{M_v}{M_{an}^{in}} W_{an}^{in} \tag{D.2}$$

$$P_{v,an}^{in} = RH_{an}^{in} P_v^{sat} \tag{D.3}$$

$$W_{an}^{in} = W_{H_2}^{in} + W_{v,an}^{in} \tag{D.4}$$

$$P_{an}^{in} = \frac{W_{an}^{in}}{k_{an}^{in}/24} + P_{an}^{ch} \tag{D.5}$$

$$M_{an}^{in} = \frac{P_{H_2}^{in} M_{H_2} + P_{v,an}^{in} M_v}{P_{an,ch}} \tag{D.6}$$

$$P_{H_2}^{in} = P_{an}^{in} - P_{v,an}^{in} \tag{D.7}$$

$$W_{an}^{out} = \bar{u} \cdot k_{an}^{out}(p_{an}^{ch} - p^{amb}) \tag{D.8}$$

$$P_{an}^{ch} = c_{an}^{ch} R T_{st} \tag{D.9}$$

$$c_{an}^{ch} = (c_{v,an}^{ch} + c_{H_2}^{ch}) \tag{D.10}$$

$$W_{H_2}^{out} = \frac{c_{H_2}^{ch}}{c_{an}^{ch}} \frac{M_{H_2}}{M_{an}^{ch}} W_{an}^{out} \tag{D.11}$$

$$W_{v,an}^{out} = \frac{c_{v,an}^{ch}}{c_{an}^{ch}} \frac{M_v}{M_{an}^{ch}} W_{an}^{out} \tag{D.12}$$

$$M_{an}^{ch} = \frac{c_{H_2}^{ch} M_{H_2} + c_{v,an}^{ch} M_v}{c_{an}^{ch}} \tag{D.13}$$

$$\frac{dc_{H_2}^{ch}}{dt} = \frac{1}{V_p M_{H_2}} \left(W_{H_2}^{in} - W_{H_2}^{out} + W_{H_2}[n] \right) \tag{D.14}$$

$$\frac{dm_{v,an}^{ch}}{dt} = \left(\Delta W_v^{ch} + W_{v,an}[n] + W_{l,an}[n] \right) \tag{D.15}$$

$$c_{v,an}^{ch} = min \left[\frac{m_{w,an}^{ch}}{M_v V_p}, c_v^{sat} \right] \tag{D.16}$$

$$\Delta W_v^{ch} = W_{v,an}^{in} - W_{v,an}^{out} \tag{D.17}$$

$$\boxed{\begin{array}{c} c_{v,an}^{2p}(x) = \alpha_1 e^{\beta x} + \alpha_2 e^{-\beta x} + c_v^{sat} \\ x \le x_{fr} \\ c_{v,an}^{2p}[k] = \alpha_1 e^{\beta x[k]} + \alpha_2 e^{-\beta x[k]} + c_v^{sat} \end{array}}$$

$$\boxed{\begin{array}{c} c_{v,an}^{1p}(x) = m^{1p}(x - L) + c_{v,an}^{ch} \\ x \ge x_{fr} \\ c_{v,an}^{1p}[k] = m^{1p}(x[k] - L) + c_{v,an}^{ch} \end{array}}$$

$$x_{fr} \triangleq min(x) \text{ such that } s(x, t) = 0 \tag{D.18}$$

For semi-analytic system, x_{fr} will be on border between sections with $s > 0$ and sections with $s = 0$.

$$\beta = \sqrt{\frac{\gamma}{D_v^{sim}}} \tag{D.19}$$

$$\boxed{\begin{aligned} W_{v,an}(x,t) &= M_v \varepsilon A_{fc} N_{v,an}(x,t) \\ W_{v,an}[k] &= M_v \varepsilon A_{fc} N_{v,an}[k] \end{aligned}}$$

$$\boxed{\begin{aligned} W_{H_2}(x,t) &= M_{H_2} \varepsilon A_{fc} N_{H_2}(x,t) \\ W_{H_2}[k] &= M_{H_2} \varepsilon A_{fc} N_{H_2}[k] \end{aligned}}$$

$$\boxed{\begin{aligned} N_{v,an}(x,t) &= -D_v^{sim} \frac{dc_{v,an}}{dx} \\ N_{v,an}[k] &= -D_v^{sim} \frac{dc_{v,an}[k]}{dx} \end{aligned}}$$

$$\boxed{\begin{aligned} N_{H_2}(x,t) &= -D_{H_2}^{sim} \frac{dc_{H_2}}{dx} \\ N_{H_2}[k] &= -D_{H_2}^{sim} \frac{dc_{H_2}[k]}{dx} \end{aligned}}$$

$$\boxed{\begin{aligned} \frac{dc_{H_2}[k]}{dx} &= -\frac{N_{H_2}^{rct}}{D_{H_2}^{sim}} \\ &\text{OR} \\ \frac{dc_{H_2}[k]}{dx} &= \frac{c_{H_2}[k+1] - c_{H_2}[k]}{\Delta x} \end{aligned}}$$

Since the continuous system would not have a discontinuity in $s(x,t)$, we apply continuity of $c_{v,an}(x)$ at x_{fr}.

$$c_{v,an}^{2p}(x_{fr}) = c_{v,an}^{1p}(x_{fr}) \tag{D.20}$$

Using mass flow continuity,

$$W_l[k] = -\rho_l \varepsilon A_{fc} b_1 S_{an}^{b_2}[k] \frac{dS_{an}[k]}{dx} \tag{D.21}$$

$$\frac{ds_{an}[k]}{dt} = \frac{-1}{\rho_l \varepsilon A_{fc}} \left(W_{l,an}[k] - W_{l,an}[k-1] \right) - r_{cond}[k]. \tag{D.22}$$

$$W_w^{1p}(x_{fr}) = W_w^{2p}(x_{fr})$$

$$W_v(x_{fr}^+, t) = W_v(x_{fr}^-, t) + W_l(x_{fr}^-, t)$$

$$D_{v,\varepsilon} \frac{dc_v^{1p}}{dx}\bigg|_{x_{fr}} = D_v^{s_{im}} \frac{dc_v^{2p}}{dx}\bigg|_{x_{fr}} - \frac{\rho_l}{M_v} b_1 S^{b_2} \frac{dS}{dx}\bigg|_{x_{fr}}$$

$$\frac{dc_v^{1p}}{dx}\bigg|_{x_{fr}} = \frac{D_v^{s_{im}}}{D_{v,\varepsilon}} \frac{dc_v^{2p}}{dx}\bigg|_{x_{fr}} - \frac{\rho_l}{D_{v,\varepsilon} M_v} b_1 S^{b_2} \frac{dS}{dx}\bigg|_{x_{fr}}$$

$$r_{cond}[k] = \frac{M_v \gamma}{\rho_l} \left(c_v^{sat} - c_{v,an}[k] \right). \tag{D.23}$$

$$S_{an}[k] = \frac{s_{an}[k] - s_{im}}{1 - s_{im}} \text{ for } s_{an}[k] > s_{im}, \tag{D.24}$$
$$S_{an}[k] = 0 \text{ O.W.}$$

$$\frac{dS_{an}[k]}{dx} = \frac{(S_{an}[k+1] - S_{an}[k])}{\Delta x}. \tag{D.25}$$

Since

$$m^{1p} \triangleq \frac{dc_v^{1p}}{dx} \tag{D.26}$$

$$c_{v,an}^{1p}(x_{fr}) = c_{v,an}^{2p}(x_{fr}) = \frac{dc_v^{1p}}{dx}(x_{fr} - L) + c_{v,an}^{ch} \tag{D.27}$$

$$\frac{dc_{v,an}^{2p}[k]}{dx} = \beta \left(\alpha_1 e^{\beta x[k]} - \alpha_2 e^{-\beta x[k]} \right) \ x \le x_{fr}$$
$$\text{OR}$$
$$m^{1p} = \frac{dc_{v,an}^{1p}[k]}{dx} = \frac{c_{v,an}^{1p}[k+1] - c_{v,an}^{1p}[k]}{\Delta x} \ x \ge x_{fr}$$

CATHODE SIDE

$$W_{O_2}^{in} = \lambda_{O_2} W_{O_2}^{rct} \tag{D.28}$$

$$W_{N_2}^{in} = \frac{0.79}{0.21} W_{O_2}^{in} \tag{D.29}$$

$$W_{v,ca}^{in} = \frac{M_v}{M_{air}} \frac{P_{v,ca}^{in}}{P_{ca}^{in}} \tag{D.30}$$

$$P_{v,ca}^{in} = RH_{ca}^{in} P_v^{sat} \tag{D.31}$$

$$W_{ca}^{in} = W_{O_2}^{in} + W_{v,ca}^{in} \tag{D.32}$$

$$P_{ca}^{in} = \frac{W_{ca}^{in}}{k_{ca}^{in}/24} + P_{ca}^{ch} \tag{D.33}$$

$$W_{ca}^{out} = k_{ca}^{out}(p_{ca}^{ch} - p^{amb}) \tag{D.34}$$

$$P_{ca}^{ch} = c_{ca}^{ch} R T_{st} \tag{D.35}$$

$$c_{ca}^{ch} = (c_{v,ca}^{ch} + c_{O_2}^{ch} + c_{N_2}^{ch}) \tag{D.36}$$

$$W_{ca}^{out} = k_{ca}^{out}(p_{ca}^{ch} - p^{amb}) \tag{D.37}$$

$$W_{O_2}^{out} = \frac{c_{O_2}^{ch}}{c_{ca}^{ch}} \frac{M_{O_2}}{M_{ca}^{ch}} W_{ca}^{out} \tag{D.38}$$

$$W_{v,ca}^{out} = \frac{c_{v,ca}^{ch}}{c_{ca}^{ch}} \frac{M_v}{M_{ca}^{ch}} W_{ca}^{out} \tag{D.39}$$

$$W_{N_2}^{out} = W_{ca}^{out} - W_{O_2}^{out} - W_{v,ca}^{out} \tag{D.40}$$

$$M_{ca}^{ch} = \frac{c_{O_2}^{ch} M_{O_2} + c_{v,ca}^{ch} M_v + c_{N_2}^{ch} M_{N_2}}{c_{an}^{ch}} \tag{D.41}$$

$$\frac{dc_{O_2}^{ch}}{dt} = \frac{1}{V_p M_{O_2}} \left(W_{O_2}^{in} - W_{O_2}^{out} + W_{O_2}[n] \right) \tag{D.42}$$

$$\frac{dc_{N_2}^{ch}}{dt} = \frac{1}{V_p M_{N_2}} \left(W_{N_2}^{in} - W_{N_2}^{out} + W_{N_2}[n] \right) \tag{D.43}$$

$$c_{v,ca}^{ch} = c_v^{sat} \tag{D.44}$$

$$\boxed{\begin{array}{c} W_{v,ca}(x,t) = M_v \varepsilon A_{fc} N_{v,ca}(x,t) \\ W_{v,ca}[k] = M_v \varepsilon A_{fc} N_{v,ca}[k] \end{array}}$$

$$\boxed{\begin{array}{c} W_{O_2}(x,t) = M_{O_2} \varepsilon A_{fc} N_{O_2}(x,t) \\ W_{O_2}[k] = M_{O_2} \varepsilon A_{fc} N_{O_2}[k] \end{array}}$$

$$\boxed{\begin{array}{c} W_{N_2}(x,t) = M_{N_2} \varepsilon A_{fc} N_{N_2}(x,t) \\ W_{N_2}[k] = M_{N_2} \varepsilon A_{fc} N_{N_2}[k] \end{array}}$$

$$\boxed{\begin{array}{c} N_{v,ca}(x,t) = -D_v^{s_{im}} \frac{dc_{v,ca}}{dx} \\ N_{v,ca}[k] = -D_v^{s_{im}} \frac{dc_{v,ca}[k]}{dx} \end{array}}$$

$$\boxed{\begin{array}{c} N_{O_2}(x,t) = -D_{O_2}^{s_{im}} \frac{dc_{O_2}}{dx} \\ N_{O_2}[k] = -D_{O_2}^{s_{im}} \frac{dc_{O_2}[k]}{dx} \end{array}}$$

$$\boxed{\begin{array}{c} N_{N_2}(x,t) = -D_{N_2}^{s_{im}} \frac{dc_{N_2}}{dx} \\ N_{N_2}[k] = -D_{N_2}^{s_{im}} \frac{dc_{N_2}[k]}{dx} \end{array}}$$

$$\boxed{\begin{array}{c} c_{v,ca}(x) = \nu_1 e^{\beta x} + \nu_2 e^{-\beta x} + c_v^{sat} \\ -L \leq x \leq 0 \\ \frac{dc_{v,an}[k]}{dx} = \beta(\nu_1 e^{\beta x} - \nu_2 e^{-\beta x}) \end{array}}$$

ANALYTIC SOLUTION

$$\beta(\alpha_1 - \alpha_2) = -\frac{N^{mb}}{D_v^{sim}},$$

$$\Downarrow \tag{D.45}$$

$$\alpha_1 = -\frac{N^{mb}}{\beta D_v^{sim}} + \alpha_2,$$

$$\alpha_1 e^{\beta x_{fr}} + \alpha_2 e^{-\beta x_{fr}} = c_v(x_{fr}) - c_v^{sat},$$

$$\Downarrow \tag{D.46}$$

$$\alpha_2 = \left(c_v(x_{fr}) - c_v^{sat} - \alpha_1 e^{\beta x_{fr}}\right)/e^{-\beta x_{fr}},$$

$$\beta(\nu_1 - \nu_2) = \frac{-N^{mb} + N_v^{rct}}{D_v^{sim}},$$

$$\Downarrow \tag{D.47}$$

$$\nu_1 = \frac{-N^{mb} + N_v^{rct}}{\beta D_v^{sim}} + \nu_2,$$

$$\nu_1 e^{-\beta L} + \nu_2 e^{\beta L} = c_v(-L) - c_v^{sat},$$

$$\Downarrow \tag{D.48}$$

$$\nu_2 = \left(c_v(-L) - c_v^{sat} - \nu_1 e^{-\beta L}\right)/e^{\beta L},$$

$$c_{v,an}\big|_{x=0} = \alpha_1 + \alpha_2 + c_v^{sat} \tag{D.49}$$

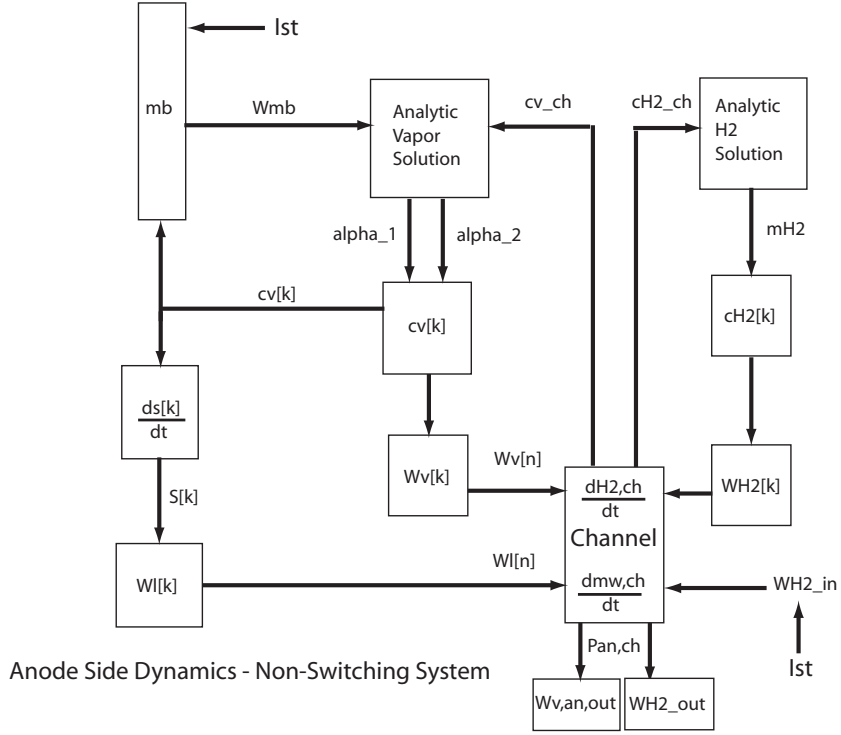$$c_{v,ca}\big|_{x=0} = \nu_1 + \nu_2 + c_v^{sat} \tag{D.50}$$

Figure D.1: Solution flow the case where the GDL has $s > 0$ for all sections ($x_{fr} = L$).

MEMBRANE TRANSPORT

$$N^{mb} = \beta_w(\lambda_{ca} - \lambda_{an}) - 2.5\frac{\lambda^{mb}}{22}\frac{i}{F} \tag{D.51}$$

$$\beta_w = 3.5 \times 10^{-6}\alpha_w\frac{\rho^{mb}}{M^{mb}t^{mb}}\frac{\lambda^{mb}}{14}e^{\frac{-2436}{T_{st}}} \tag{D.52}$$

$$\lambda_e = f(c_{v,e}^{mb}) \tag{D.53}$$

$$\lambda^{mb} = \frac{1}{2}(\lambda_{an} + \lambda_{ca}) \tag{D.54}$$
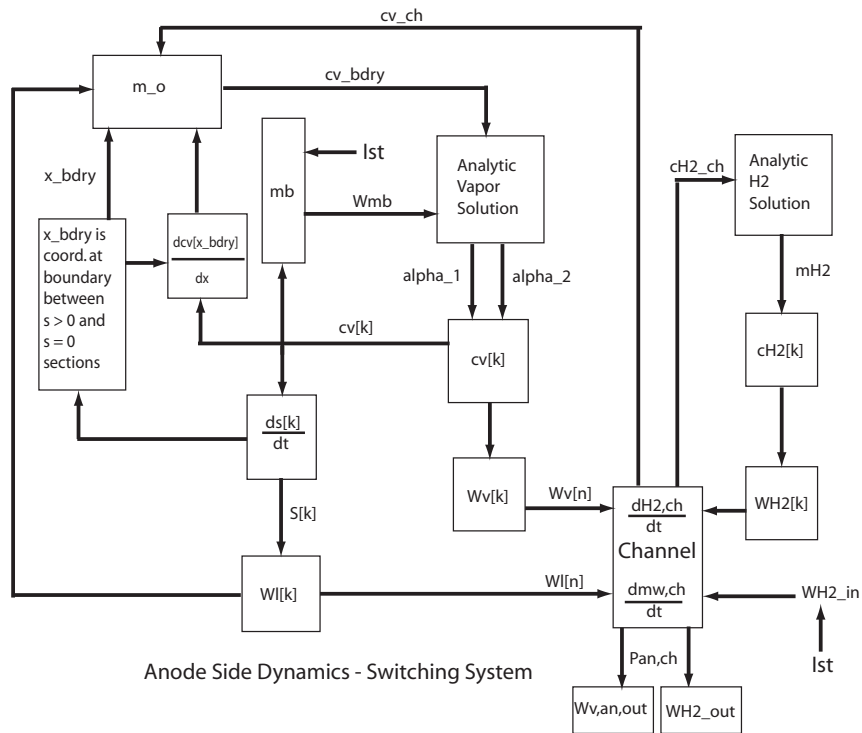
Figure D.2: Solution flow for the case where there may be some $s = 0$ sections $(x_{fr} < L)$.

Appendix E

Voltage Model

The voltage model is taken from [3] and is included here for reference.

The unique aspect of this model is embodied by the implementation of the apparent current density i_{app}, which translates the mass of liquid water accumulated in the anode channel into an apparent current density. The total water mass from (2.30) is used to find the apparent fuel cell active area, A_{app}, which is the total active area less the area occupied by the thin film of liquid water that is assumed to form on the GDL-channel interface,

$$A_{app} = A_{fc} - \frac{2m_l^{ch}}{\rho_l t_{wl}}.$$ (E.1)

The film thickness, $t_{wl} = 0.14$ mm is another tunable parameter, and the factor of 2 in the numerator exists since only half of the GDL-channel interfacial area is available for coverage due to the gas distributor land area.

The apparent current density is found by using A_{app} from

$$i_{app} = \frac{I_{st}}{A_{app}}.$$ (E.2)

The estimated cell voltage, $\hat{v}$, is equal to the theoretical open circuit voltage less the activation, ohmic, and concentration voltage losses,

$$\hat{v} = E - U_{act} - U_{ohmic} - U_{conc}.$$ (E.3)

Typical fuel cell operation avoids the concentration loss range of current density, therefore $U_{conc} = 0$. The theoretical open circuit voltage varies with temperature, reactant partial pressures, and temperature according to [65],

$$E = -\left(\frac{\Delta H}{2F} - \frac{T_{st}\Delta S}{2F}\right) + \frac{RT_{st}}{2F}\ln\left(\frac{p_{H_2}^{mb}\sqrt{p_{O_2}^{mb}}}{p_o^{1.5}}\right),$$ (E.4)

where ΔS and ΔH are the differences in entropy and enthalpy from standard conditions, p_o is the standard pressure, and $p_{O_2}^{mb}$ and $p_{H_2}^{mb}$ are taken from the GDL Section 1.

The activation voltage loss is modeled using,

$$U_{act} = K_1 \frac{RT_{st}}{F} \ln\left(\frac{i_{app}}{i_o}\right), \tag{E.5}$$

where $K_1 = 1.17$ is a charge transfer-related coefficient, and the exchange current density, i_o, is given by,

$$i_o = K_2 \left(\frac{p_{O_2}^{mb}}{p_o}\right)^{K_3} exp\left[-\frac{E_c}{RT_{st}}\left(1 - \frac{T_{st}}{T_o}\right)\right], \tag{E.6}$$

where $K_2 = 4.44\ \mu A$ and $K_3 = 1.78$ are tunable parameters, E_c is the activation energy for oxygen reduction on Pt, and T_o is the reference temperature.

Finally, the ohmic voltage loss model is taken from [13], including the experimentally identified parameters b_{11} and b_{12}, and modified with the tunable parameter $K_4 = 3.27$,

$$U_{ohmic} = K_4 \left[\frac{t_{mb}}{(b_{11}\lambda^{mb} - b_{12})} e^{-1268\left(\frac{1}{303} - \frac{1}{T_{st}}\right)}\right] i_{app}, \tag{E.7}$$

where t^{mb} is the membrane thickness and λ^{mb} is the membrane water content.

Bibliography

[1] T. Levitt, "Marketing myopia," *Harvard Business Review*, vol. 38, pp. 24–47, Jul-Aug 1960.

[2] Congress, House, Subcommittee on Energy and Air Quality, "The hydrogen energy economy hearing," *108th Congress, 1st Session*, May 20 2003.

[3] D. A. McKay, J. B. Siegel, W. T. Ott, and A. G. Stefanopoulou, "Parameterization and prediction of temporal fuel cell voltage behavior during flooding and drying conditions," *J. Power Sources*, vol. 178, no. 1, pp. 207–222, 2008.

[4] J. B. Siegel and A. G. Stefanopoulou, "Modeling and visualization of fuel cell water dynamics using neutron imaging." Seattle, WA, USA: Accepted to 2008 ACC, June 2008.

[5] J. H. Nam and M. Kaviany, "Effective diffusivity and water-saturation distribution in single- and two-layer PEMFC diffusion medium," *Int. J Heat Mass Transfer*, vol. 46, pp. 4595–4611, 2003.

[6] C. Wang, "Fundamental models for fuel cell engineering," *Chemical Reviews*, vol. 104, pp. 4727–4766, 2004.

[7] Y. Wang and C.-Y. Wang, "Ultra large-scale simulation of polymer electrolyte fuel cells," *Journal of Power Sources*, vol. 153, p. 130135, 2006.

[8] V. Gurau, H. Liu, and S. Kakaç, "Two-dimensional model for proton exchange membrane fuel cells," *American Institute of Chemical Engineers Journal*, vol. 44, no. 11, pp. 2410–2422, 1998.

[9] D. Natarajan and T. V. Nguyen, "A two-dimensional, two-phase, multicomponent, transient model for the cathode of a proton exchange membrane fuel cell using conventional gas distributors," *J. Electrochemical Society*, vol. 148, no. 12, pp. A1324–A1335, 2001.

[10] A. Y. Karnik and J. Sun, "Modeling and control of PEMFC system with an anode recirculation." Ypsilanti, MI: 2005 Third International Conference on Fuel Cell Science, Engineering and Technology, May 2005.

[11] J. Pukrushpan, A. Stefanopoulou, and H. Peng, "Controlling fuel cell breathing," *IEEE Control Systems Magazine*, vol. 24, no. 2, pp. 30–46, April 2004.

[12] V. Tsourapas, A. G. Stefanopoulou, and J. Sun, "Dynamics, optimization and control of a fuel cell based combined heat power (chp) system for shipboard applications." Portland, OR, USA: in Proceedings American Control Conference, June 2005.

[13] T. E. Springer, T. A. Zawodzinski, and S. Gottesfeld, "Polymer electrolyte fuel cell model," *Journal of the Electrochemical Society*, vol. 138, no. 8, pp. 2334–2342, 1991.

[14] D. Bernardi and M. Verbrugge, "A mathematical model of the solid-polymer-electrolyte fuel cell," *J. Electrochem. Soc.*, vol. 139, no. 9, pp. 2477–2491, 1992.

[15] T. Fuller and J. Newman, "Water and thermal management in solid-polymer-electrolyte fuel cells," *J. Electrochem. Soc.*, vol. 5, 1993.

[16] K. Dannenberg, P. Ekdunge, and G. Lindbergh, "Mathematical model of the PEMFC," *J. Appl. Electrochem.*, vol. 30, no. 12, pp. 1377–1387, 2000.

[17] A. Kulikovsky, "Semi-analytical 1D + 1D model of a polymer electrolyte fuel cell," *Electrochemistry Communications*, vol. 6, pp. 969–977, 2004.

[18] P. Berg, K. Promislow, J. Pierre, J. Stumper, and B. Wetton, "Water management in PEM fuel cells," *J. Electrochem. Soc.*, vol. 151, pp. A341–A353, 2004.

[19] S. Um and C. Wang, "Three-dimensional analysis of transport and electrochemical reactions in polymer electrolyte fuel cells," *Journal of Power Sources*, vol. 125, p. 4051, 2004.

[20] T. Berning and N. Djilali, "A 3d, multiphase, multicomponent model of the cathode and anode of a pem fuel cell," *J. Electrochem. Soc.*, vol. 150, no. 12, pp. A1589–A1598, 2003.

[21] K. Promislow and J. Stockie, "Adiabatic relaxation of convective-diffusive gas transport in a porous fuel cell electrode," *SIAM J. Appl. Math.*, vol. 62, pp. 180–205, 2001.

[22] K. Promislow, P. Chang, H. Haas, and B. Wetton, "A two-phase unit cell model for slow transients in polymer electrolyte membrane fuel cells," *Submitted to the J. Elec. Soc.*, 2008.

[23] M. Grötsch and M. Mangold, "A two-phase pemfc model for process control purposes," *Chemical Engineering Science*, vol. 63, pp. 434–447, 2007.

[24] J. T. Pukrushpan, A. G. Stefanopoulou, and H. Peng, *Control of Fuel Cell Power Systems: Principles, Modeling, Analysis and Feedback Design.* New York: Springer, 2000.

[25] K. W. Suh and A. G. Stefanopoulou, "Control and coordination of air compressor and voltage converter in load-following fuel cells," *Int'l Journal Energy Research*, vol. 29, pp. 1167–1189, 2007.

[26] C. Lauzze and D. J. Chmielewski, "Power control of a polymer electrolyte membrane fuel cell," *Journal of Industrial Engineering Chemical Research*, vol. 45, pp. 4661–4670, 2006.

[27] W. E. Mufford and D. G. Strasky, "Power control system for a fuel cell powered vehicle," *US patent 5 771 476*, June 2006.

119

[28] F. Zenith and S. Skogestad, "Control of fuel cell power output," *Journal of Process Control*, vol. 17, pp. 333–347, 2007.

[29] J. Sun and I. V. Kolmanovsky, "Robust reference governor for fuel cell starvation protection," *IEEE Trans. in Control Systems Technology*, vol. 13, no. 6, pp. 911–920, 2004.

[30] B. Moore, "Principal component analysis in linear systems: Controllability, observability, and model reduction," *IEEE Transactions on Automatic Control*, vol. AC-26, pp. 17–32, Feb 1981.

[31] D. Wilson, "Optimum solution of model-reduction problem," *Proc. of IEEE*, vol. 117, pp. 1161–1165, 1970.

[32] R. Skelton, "Cost decomposition of linear systems with application to model reduction," *Int'l Journal of Control*, vol. 32, pp. 1031–1055, 1980.

[33] D. Hyland and D. Bernstein, "The optimal projection equations for model reduction and the relationships among the methods of wilson, skelton, and moore," *Proc. of IEEE*, pp. 1201–1211, 1985.

[34] M. Loeve, "Functions aleatoire de second order," *C.R. Acadamie Science*, vol. 220, 1945.

[35] K. Glover, "All optimal hankel-norm approximations of linear multivariable systems and their L_∞ bounds," *Int'l Journal of Control*, vol. 39, pp. 1115–1193, 1984.

[36] L. Louca, J. Stein, G. Hulbert, and J. Sprague, "Proper model generation: An energy-based methodology," *Proceedings of the 1997 International Conference on Bond Graph Modeling*, pp. 44–49, Jan 1997.

[37] J. Stein and B. Wilson, "An algorithm for obtaining minimum-order models of distributed and discrete systems," *Automated Modeling*, pp. 47–58, 1992.

[38] S. Lall, P. Krysl, and J. Marsden, "Structure-preserving model reduction for mechanical systems," *Physica D*, vol. 184, pp. 304–318, 2003.

[39] C. Rowley, "Model reduction for fluids, using balanced proper orthogonal decomposition," *Int'l Journal on Bifurcation and Chaos*, vol. 15, pp. 997–1013, 2005.

[40] S. Lall, J. Marsden, and S. Glavaski, "Structure-preserving model reduction for mechanical systems," *Proc. of the IFAC World Congress*, pp. 473–478, 1999.

[41] ——, "A subspace approach to balanced truncation for model reduction of nonlinear control systems," *Int'l Journal of Robust Nonlinear Control*, vol. 12, pp. 519–535, 2002.

[42] B. Wilson and J. Taylor, "A model-order-deduction algorithm for nonlinear systems," *Automated Modeling for Design 1993*.

[43] D. Vasilyev, M. Rewieński, and J. White, "Perturbation analysis of tbr model reduction in application to trajectory-piecewise linear algorithm for mems structures," *Proceedings of the NSTI-Nanotech 2004*.

[44] M. J. Rewieṅski, "A trajectory piecewise-linear approach to model order reduction of nonlinear dynamical systems," Ph.D. dissertation, Massachusetts Institute of Technology, 2003.

[45] N. Djilali and D. Lu, "Influence of heat transfer on gas and water transport in fuel cells," *International Journal of Thermal Science*, vol. 41, pp. 29–40, 2002.

[46] F. Y. Zhang, X. G. Yang, and C.-Y. Wang, "Liquid water removal from a polymer electrolyte fuel cell," *J. Electrochemical Society*, vol. 153, no. 2, pp. A225–A232, 2006.

[47] J. Mahadevan, M. Sharma, and Y. Yortsos, "Flow-through drying of porous media," *American Institute of Chemical Engineers Journal*, vol. 52, no. 7, pp. 2367–2380, 2006.

[48] J. P. Owejan, J. E. Owejan, T. W. Tighe, W. Gu, and M. Mathias, "Investigation of fundamental transport mechanism of product water from cathode catalyst layer in PEMFCs." San Diego, CA, USA: 5th Joint ASME/JSME Fluids Engineering Conference, July 2007.

[49] S. Dutta and S. Shimpalee, "Numerical prediction of mass-exchange between cathode and anode channels in a pem fuel cell," *Int'l Journal of Heat and Mass Transfer*, vol. 44, 2001.

[50] A. A. Shah, G. S. Kim, W. Gervais, A. Young, K. Promislow, and D. Harvey, "The effects of water and microstructure on the performance of polymer electrolyte fuel cells," *J. Power Sources*, vol. 160, pp. 1251–1268, 2006.

[51] H. Meng and C.-Y. Wang, "Electron transport in PEFCs," *J. Electrochemical Society*, vol. 151, no. 3, pp. A358–A367, 2004.

[52] N. P. Siegel, M. W. Ellis, D. J. Nelson, and M. R. von Spakovsky, "A two-dimensional computational model of a PEMFC with liquid water transport," *J. Power Sources*, vol. 128, no. 1, pp. 173–184, 2006.

[53] S. Mazumder and J. V. Cole, "Rigorous 3d mathematical modeling of PEM fuel cells: 2 model predictions with liquid transport," *J. Electrochem. Soc.*, vol. 150, no. 11, pp. A1510–A1517, 2003.

[54] M. Gan and L.-D. Chen, "Analytic solution for two-phase flow in PEMFC gas diffusion layer." Irvine, CA, USA: ASME Fuel Cell 2006, ASMEFC2006-97104, June 2006.

[55] B. A. McCain, A. G. Stefanopoulou, and I. V. Kolmanovsky, "A dynamic semi-analytic channel-to-channel model of two-phase water distribution for estimation and control of fuel cells," *Submitted to IEEE Transactions in Control Systems Technology.*

[56] E. Osborne, "On pre-conditioning of matrices," *Journal of the ACM*, vol. 7, pp. 338–345, 1960.

[57] W. Huang, B. Zhou, and A. Sobiesiak, "Along-channel mathematical modelling for proton exchange membrane fuel cells," *Int'l J. of Energy Research*, vol. 29, pp. 1051–1071, 2005.

[58] Z.Bai, M. Durstock, and T. Dang, "Proton conductivity and properties of sulfonated polyarylenethioether sulfones as proton exchange membranes in fuel cells," *J. of Membrane Science*, vol. 281, pp. 508–516, 2006.

[59] M. Vynnycky, "On the modelling of two-phase flow in the cathode gas diffusion layer of a polymer electrolyte fuel cell," *Appl. Math and Comp*, vol. 189, pp. 1560–1575, 2007.

[60] M. Krstic and A. Smyshlyaev, "Boundary control of PDEs: A short course on backstepping designs," *SIAM*, to appear May, 2008.

[61] T. Sugawara, "Fuel cell power generation system," *US patent 6617066*, Sep 2003.

[62] ——, "Variable flow-rate ejector and a fuel cell having the same," *US patent 6858340*, Feb 2005.

[63] T. Kailath, *Linear Systems*, 1st ed. Englewood Cliffs, NJ: Prentice Hall, Inc., 1980.

[64] T. Ujiie, "Overview of fuel cell R&D on NEDO." Japan: New Energy and Industrial Technology Development Organization (NEDO), Oct 2006.

[65] R. O'Hayre, S. Cha, W. Colella, and F. Prinz, *Fuel Cell Fundamentals.* Hoboken: Wiley, 2006.